DEVELOPMENTS IN THE USE OF DIFFUSION TENSOR IMAGING DATA TO INVESTIGATE BRAIN STRUCTURE AND CONNECTIVITY

A thesis submitted in partial fulfilment of the

requirements for the Degree of

Doctor of Philosophy in Medical Physics

in the University of Canterbury

by Michael H. Chappell

University of Canterbury

2007

Acknowledgments

Research, especially when one is learning the tools of the trade, and when the trade is as diverse as MRI, is necessarily collaborative. Obtaining the required subject-matter knowledge and professional skills to undertake further research in the field can only happen with the patience, support, expertise and encouragement of one's mentors. With this in mind, and with the brevity of the acknowledgment in no way reflecting the degree of my gratitude, I wish to express sincere appreciation to my primary supervisor Dr Richard Watts for his endless enthusiasm and patience, to Dr Jennifer Brown and Associate Professor John Dalrymple-Alford as my ever-helpful and supportive co-supervisors, and to Associate Professor Lou Reinisch for his timely comments, suggestions and mentoring support.

Abstract

Diffusion tensor imaging (DTI) is a specialist MRI modality that can identify microstructural changes or abnormalities in the brain. It can also be used to show fibre tract pathways. Both of these features were used in this thesis. Firstly, standard imaging analysis techniques were used to study the effects of mild, repetitive closed head injury on a group of professional boxers. Such data is extremely rare, so the findings of regions of brain abnormalities in the boxers are important, adding to the body of knowledge about more severe traumatic brain injury. The author developed a novel multivariate analysis technique which was used on the same data. This new technique proved to be more sensitive than the standard univariate methods commonly used.

An important part of diagnosing and monitoring brain damage involves the use of bio-markers. A novel investigation of whether diffusion parameters obtained from DTI data could serve as bio-markers of cognitive impairment in Parkinson's disease was conducted. This also involved developing a multivariate approach, which displayed increased sensitivity compared with any of the component parameters used singly, and suggested these diffusion measures could be robust bio-markers of cognitive impairment.

Fibre tract connectivity between regions of the brain is also a potentially valuable measure for diagnosis and monitoring brain integrity. The feasibility of this was investigated in a multi-modal MRI study. Functional MRI (fMRI) identifies regions of activation associated with a particular task. DTI can then find the pathway of the fibre bundles connecting these regions. The feasibility of using regional connectivity to interrogate brain integrity was investigated using a single healthy volunteer. Fibre pathways between regions activated and deactivated by a working memory paradigm were determined. Though the results are only preliminary, they suggest that this line of research should be continued.

Context

Because of the inter-disciplinary nature of MRI research - including neurologists, radiologists, psychologists, physicists, engineers computer scientists and statisticians - clinical studies normally involve several researchers from a range of disciplines. The work presented in this thesis is no exception. My role was to analyse and process MRI data to answer questions concerning the development and utility of DTI methodology across three different contexts.

The diffusion boxer data were acquired by Dr Aziz Ulug and Dr Lijuan Zhang. Professional boxers in the United States are required to undergo routine MRI scanning as part of the monitoring process. These data are unique in that they do not represent patients presenting with traumatic symptoms, and so provide important data on chronic, repetitive, non-symptomatic head injury. For ethical reasons, it is impossible to design a study to deliberately obtain this type of data. My contribution was two-fold: firstly, the use of standard voxel-based analysis techniques to investigate the chronic brain injury suffered by these subjects; and secondly, the development and comparison of novel multivariate methods that were used with the boxer data. Statisticians Dr Jennifer Brown and Dr Mike Steel were instrumental in giving a direction for these studies in the early stages, and in overseeing their development.

The Parkinson's disease study involved investigating whether MRI could provide quantitative measures that would act as biomarkers of cognitive decline in Parkinson's disease. The MRI scanning was done at Southern Cross Hospital in Christchurch, with Professor Tim Anderson, Dr Scott Wells and Mr Gareth Leeper providing the medical and technical expertise, and Dr John Dalrymple-Alford and Ms Saskia van Stockum providing expertise in neuropsychology. I used the neuropsychological measures provided to generate regression analyses with different diffusion measures in the search for biomarkers. The neuropsychology testing was undertaken by Ms van Stockum and reflected in part various developments by local researchers including Dr Dalrymple-Alford, Prof Anderson, Dr John Fink, Dr Michael MacAskill and Ms Audrey McKinlay.

The connectivity study involved functional imaging of a memory paradigm designed and implemented by Dr Dalrymple-Alford and Dr Richard Watts. My contribution

entailed finding regions that were co-activated in the memory task and then using DTI data to investigate the existence of possible fibre tracts connecting these regions.

Integral to all these studies was the oversight and physics expertise of Dr Richard Watts.

Table of Contents

List of Figures

List of Tables

1 Introduction

Medical imaging is the science of extracting spatially and temporally resolved information at all physical scales.

Dr Elias A. Zerhouni
Director of NIH
ISMRM 2006

Brain damage, whether through head trauma or degenerative diseases such as Parkinson's disease, can affect the brain's grey matter (GM), white matter (WM), or both, in a way that is distinctive to the cause of the damage. Being able to recognise the signature patterns of various causes will aid diagnosis, and being able to track the progression of the damage over time is important for selecting and monitoring treatment. Within the last two decades, the advent of various imaging modalities has made possible the non-invasive *in vivo* imaging of the brain. Pre-eminent among these modalities for being able to show soft-tissue contrast is magnetic resonance imaging (MRI). This is a very versatile modality, with the operator able to control the imaging parameters in such a way as to make the image sensitive to different contrast mechanisms. Furthermore, these mechanisms are, in most cases, naturally occurring, which obviates the need for invasive contrast agents. One such technique is diffusion tensor imaging (DTI), in which the contrast mechanism is the diffusion (or random motion) of the water molecules in the brain. Because the temporal resolution of these scans is such that a single molecule will typically move a distance about the same size as a neuron on that time scale, changes occurring on that spatial scale can be detected. This technique is therefore sensitive to microstructural changes in the brain that may not be obvious on the macroscopic scale.

With the worldwide trend away from diseases being predominantly acute, short term and lethal to being more chronic and long-term, the disease burden on the patient and on the health system is growing at an alarming rate. Indeed, Dr Elias A. Zerhouni, the Director of the National Institute of Health in the United States, giving the Mansfield Lecture at the 14th scientific meeting of the International Society for Magnetic Resonance in Medicine in Seattle in 2006, insisted a change in paradigm is necessary for health care. He asserted that medicine is going to move from being curative to being pre-emptive, and that an integral part of this will be imaging.

Contrasting biological data of the future with that presently available, Dr Zerhouni noted that it will change from being:

- Destructive to non-destructive
- Qualitative to quantitative
- Uni-dimensional to multi-dimensional
- Low temporal resolution to high temporal resolution
- Non-localized to spatially resolved

MRI, especially when, as throughout this study, no contrast agents are used, is completely non-invasive, and so meets the first criterion.

While standard medical MR images are presently interpreted qualitatively, or at best semi-quantitatively, by a radiologist, the specialist DTI sub-modality provides quantitative information. This opens up the possibilities of both longitudinal studies and inter-site studies. The development of readily useable quantitative analyses are an important part of this study.

Developing methods of multivariate analysis of the DTI data is one of its most significant features of my research, improving the diagnostic quality of the analyses. I show how multivariate analyses can be used with both group comparisons and with regression analyses with a single group, in search of bio-markers of brain abnormalities. Multi-dimensionality also implies integrating data analyses across modalities. Researchers are increasingly looking for ways of combining the data from different imaging modalities such as functional MRI and electroencephalography (EEG). This study includes a preliminary investigation of the connectivity between different regions of the brain by combining DTI and functional MRI (fMRI) data.

While DTI studies are still predominantly cross-sectional, the quantitative nature of the data (in contrast to conventional medical scans which are intensity- and therefore scanner- dependent) makes it an excellent prospect for longitudinal and inter-site studies. By getting an immediate "snapshot" of the brain rather than having to wait for either cognitive/behavioural changes to manifest themselves or a post-mortem, temporal resolution will be greatly enhanced. This has important implications for diagnosis and

treatment of brain disorders. The spatial resolution of 2 mm of the DTI data in the current study make it possible to localize the effects of mild chronic brain damage in a way that has not been done before. In both the head trauma and degenerative disease studies described here, it was possible to localise regions of microstructural brain damage that were not visible on standard clinical MR (or other modality) images. This is a great strength of DTI, made even more sensitive by the multivariate methods I developed.

As well as the cost to the health system and the disease burden on the patient, there is another reason for moving medicine from treating the disease once symptoms become apparent and normal function is lost to intervening before the symptoms appear. There is presently no evidence that degenerative neurological diseases such as Alzheimer's are reversible. As the prevalence of these diseases increases with the aging population, rather than waiting for symptoms to appear, a better approach would be to start treatment early to delay the progression of the disease, thus preserving normal function in the patient for as long as possible. However, detecting and treating pre-symptomatically puts great demands on diagnostic procedures, and it is here that imaging has an important role to play. Treatment will become more efficiently targeted at those identified as being at risk. For this to be an effective strategy, imaging bio-markers will be needed to identify the disease early, then track the effectiveness of any treatment.

Imaging in general, and MRI in particular, is well-suited to meet the challenges of the future, and to have an important role to play in the new medical paradigm described by Dr Zerhouni. This study represents a step in this direction, particularly in

- the localization of brain damage
- investigating the usefulness of diffusion measures as bio-markers of brain disorders
- establishing new methodologies for multivariate analysis
- combining DTI and fMRI data.

Specifically, localisation of brain damage resulting from repeated, non-severe blows to the head was achieved with DTI data of professional boxers; investigating bio-markers,

as well as localising brain deterioration, entailed analysis of DTI data from a group of Parkinson's disease patients; and investigating connectivity between memory task activated and deactivated regions was done using functional MRI and DTI data from a healthy volunteer.

The motivation for the boxer study was three-fold.

1. While a lot of research on brain injury has been done using MRI, it has been overwhelmingly concentrated on single instances of traumatic injury, usually either moderate or severe. Research on chronic, repetitive, non-severe brain damage has been neglected in comparison. Indeed, it is only recently that there has been a growing awareness that this latter non-symptomatic damage is real and potentially serious. DTI's ability to reveal information about the microstructure of the brain has played a major part in this awareness, and this study demonstrates its important role in this under-reported field.

2. Professional boxers afford a unique opportunity to study chronic mild head injury (in contrast to traumatic mild head injury). Obtaining data on subjects who undergo repetitive blows to the head, yet are not hospitalized or even present with any obvious symptoms, is difficult. It is clearly unethical to conduct experiments of this nature on humans, so researchers are reliant on subjects for whom this occurs in their daily lives (typically head-contact sports players). However, identifying and contacting such subjects is difficult, and then persuading them to undergo scanning is often even harder. The best outcome from their point of view is that their brains are undamaged. Discovering damage could jeopardize both their sporting careers and their livelihood, so their reluctance to voluntarily move in this direction is understandable. However, in New York it is mandatory for all professional boxers to submit for regular MRI scanning as a monitoring mechanism.

3. The boxer data used in this study have been analysed before and the results published. This was at the whole brain and region of interest level. Having been collected as DTI data, a full voxel-based analysis was waiting to be done. This study has filled that gap.

The motivation for the Parkinson's disease study was to discover more about the cognitive state of patients who were at risk of later degeneration. A better understanding of the progression to dementia that many subjects undergo would help in the prediction and monitoring of such a course. Imaging has an important role in finding out whether there are new suitable biomarkers that could be used in such monitoring. Until recently, the mental state of these patients has primarily been ascertained using neuro-psychological measures often with general status measures such as the Mini Mental State Examination (MMSE). However, while such measures have been developed and refined over many years, they would benefit from the added spatial information diffusion bio-markers might bring. Neuro-psychological measures lack spatial resolution, as they are seldom specific to local brain regions. DTI produces potential imaging bio-markers that can change from voxel to voxel, thus allowing a much more spatially localised tracking of disease progression.

With the drive in imaging research to integrate the findings from different disciplines or modalities, ways of enhancing DTI research are being explored. This provides the motivation for the connectivity study, where data from fMRI are used to inform the tractography performed with the DTI data. While it would have been interesting, and added to the completion of the analyses to use boxers and Parkinson's patients for this, for technological reasons no fMRI data had been collected for either group. A normal, healthy volunteer was used for this part of the research.

This thesis is arranged as follows.

Chapter 2 outlines some basic principles of nuclear magnetic resonance (NMR), which is the foundation for MRI. A brief explanation is then given of how the NMR signal is spatially encoded in order to produce a magnetic resonance image. The first such image of the human head was performed in 1979. Clearly this cannot attempt to be a comprehensive treatise of MRI theory, but rather is a selection of the main aspects of the theory that pertain to this study. Where appropriate, the author has attempted to emphasize the potential for error at any stage of the design - acquisition - analysis process of any investigation, and to provide the framework to discuss the strengths and weaknesses of the studies in this research.

Chapter 3 continues the theory presented in chapter 2, applying it now to the specialist modalities of DTI and fMRI. The emphasis in this chapter is on data acquisition and analysis. Topics central to the analysis of these images such as image registration and normalization, statistical techniques to account for the multiple comparison problem, and the general linear model are introduced.

Chapter 4 describes how standard DTI techniques were used with professional boxers to investigate chronic head injury. The novelty of this study was that it involved localizing damage in subjects whose injuries were non-acute and non-symptomatic. The spatial resolution of a few mm has not previously been reported for this type of injury. The voxel-based analysis used here is a data-driven approach which requires no a priori information. The study showed that chronic brain damage can occur in head contact situations even where no outward symptoms are manifest. This has implications beyond boxing, for example to other head-contact sports and for battered child syndrome.

Chapter 5 explains important methodological developments, with novel techniques for analysing DTI data. The boxer data are used to illustrate the use of these techniques and to compare the results with those of standard methods (as used in Chapter 4). Whereas standard DTI analysis methods are univariate, the methods developed here are multivariate, with the potential for greatly increased sensitivity. Higher intrinsic sensitivity means the level of confidence can be raised compared with a less sensitive test without losing information about abnormalities altogether. This results in increased specificity. While exploratory research studies might be more focused towards higher sensitivity with a tolerance for lower specificity, interventional clinical investigations might require a much higher specificity. The methods developed here give more flexibility to move in either of these directions by appropriately changing the statistical thresholds.

Chapter 6 records the investigation of whether DTI diffusion metrics could be used as possible bio-markers of the cognitive decline in patients with Parkinson's disease (PD). In this study, the diffusion metrics were regressed against neuropsychological variables, and a novel multiple regression method is described, akin to, but different from, the one used with the boxer data. Suitable potential bio-markers were discovered, and these will undergo further testing in a larger study of Parkinson's disease.

In chapter 7 the white matter (WM) connectivity between the regions activated when certain tasks were performed was investigated. In this bi-modality approach, these regions were determined from the functional information from fMRI, and provided the seed and target points for the tractography determined from the DTI. Studying the connectivity between points known to co-activate in a given brain is an instructive way of investigating brain architecture. In the past, seed points (and target points if they were being used) have usually been chosen either from a "text book" perspective – where certain structures "*should*" be – or from a structural perspective – where certain structures *seemed* to be. But when it comes to architecture and connectivity, no two brains are alike, so studying connectivity based on personalized functional information is a step forward.

Chapter 8 concludes the research. It includes a discussion of the place of DTI in investigating brain structure and architecture as illustrated in these studies, summarising the findings from these studies using DTI analyses, and comparing and contrasting the new techniques used here. Suggested areas of further research are then outlined.

2 Principles of MRI Data Acquisition and Image Reconstruction

2.1 Basic Concepts: The Nuclear Magnetic Resonance Signal

MRI is a non-invasive, high-resolution imaging modality with many clinical and research applications. Its strength lies in its versatility. Whereas computed tomography (CT), for example, has only a single imaging parameter (the linear attenuation coefficient of the biological tissue), the tissue magnetization that MRI measures is sensitive to several different tissue parameters, to which the process can be "tuned". Furthermore, as well as standard anatomical medical images, MRI can yield information about tissue microstructure that is not apparent at larger scales. MRI is a development of nuclear magnetic resonance (NMR), which itself has important medical applications (Bechinger 1999; Jaroniec, et al. 2004; Srivastava and Govil 2001). Both NMR and MRI are based on the interactions of magnetic nuclei with an external magnetic field.

The hydrogen nucleus, comprising a single proton, has the potential to become weakly paramagnetic when subjected to strong magnetic fields. Since hydrogen is the most common element in the human body, there is the potential for the body to develop a net magnetization vector (NMV) in a strong magnetic field. This is the foundation premise on which MRI is based. In the strong field of an MR scanner (typically 1.5 or 3 tesla), the magnetic moment of each hydrogen nucleus (often simply called a "spin") has two quantum states available to it: the low-energy "spin-up" state, and the higher energy "spin-down" state. Classically, these are sometimes referred to as the spins being aligned either parallel or anti-parallel with the external field, respectively. Thermal energy can provide enough energy to promote a spin into the spin-down, higher energy state. Therefore the lower the temperature, the less spin-down occupation there will be, leaving a larger net occupation by spins of the spin-up state, so larger NMV. At room temperature, using a 3 T magnetic field, the excess number of protons in the spin-up state compared with the spin-down state is about 10 per million spins. It is this excess that creates the NMV that is used to interrogate the substance in a two-stage process. The first step is to energize, or "excite" the NMV by the application of an electromagnetic radiofrequency (RF) signal. Next, the NMV is allowed to return to its

equilibrium state, giving off electromagnetic radiation as it does so. This emitted radiation is recorded and provides data from which image contrast can be detected.

Classical Description of NMR

Each spin can be thought of as a tiny spinning charge (i.e. a tiny electric current) with magnetic moment $\boldsymbol{\mu}$. In the presence of an external magnetic field $\boldsymbol{B}$, a torque $\boldsymbol{\tau}$ acts on the spin. This is given by the vector cross-product:

$$\boldsymbol{\tau} = \boldsymbol{\mu} \times \boldsymbol{B} \tag{2.1}$$

A non-zero net torque produces a change in the angular momentum $\boldsymbol{J}$ given by:

$$\frac{d\boldsymbol{J}}{dt} = \boldsymbol{\tau} \tag{2.2}$$

and the relationship between the spin angular momentum and the magnetic moment has been found experimentally to be given by (Haacke, et al. 1999):

$$\boldsymbol{\mu} = \gamma \boldsymbol{J} \tag{2.3}$$

where the proportionality constant γ is called the *gyromagnetic ratio.*

Combining these three equations gives the fundamental equation of motion:

$$\frac{d\boldsymbol{\mu}}{dt} = \gamma \boldsymbol{\mu} \times \boldsymbol{B} \tag{2.4}$$

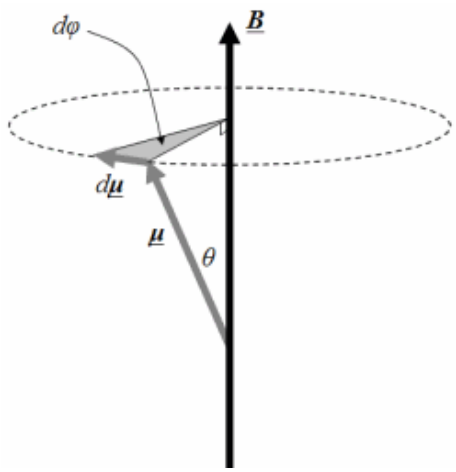

Figure 2.1 Precession schematic for a proton in an external magnetic field *B* (from Haacke, 1999)

This is the *Bloch equation without relaxation*, representing the precession of a steady state spin without relaxation. Since $d\boldsymbol{\mu}$ traces out the precession circle (Figure 2.1), it directly relates to the precession frequency of the spin. Geometrical considerations show that $|d\boldsymbol{\mu}| = d\mu = \mu \sin\theta \, d\varphi$. Substituting this in the modulus of Eq. 2.4 gives the precession frequency:

$$\omega = \gamma B \qquad 2.5$$

where ω is the Larmor frequency (MHz)

γ is the gyromagnetic ratio (MHz.T^{-1}) (= 42.58 MHz.T^{-1} for protons)

B is the external magnetic field strength (T)

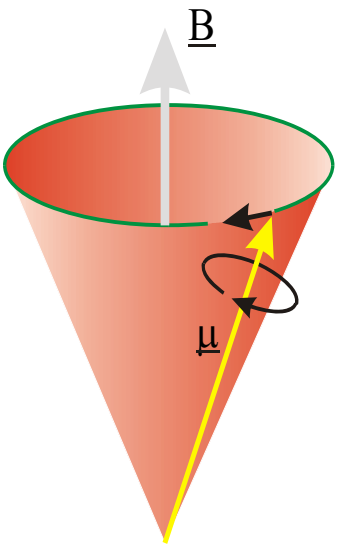

Figure 2.2 Cone of precession of the spinning proton in the magnetic field B.

This Larmor, or precession, frequency is the resonant frequency of the spin precessing about the axis of the external field (Figure 2.2). The NMV of the excess spins can be manipulated by exposing the spins to an oscillating magnetic field at their resonant frequency. Typically with MRI this radiation is in the radio frequency (RF) range. When such an RF pulse is applied to the subject, some spins resonate by moving into a higher energy state. This results in the net magnetization vector precessing, also at the Larmor frequency, about the z-axis as it spirals down towards the transverse plane (Figure 2.3a).

To understand the effects of RF pulses and the ensuing relaxations, it is helpful to use a rotating frame of reference. This frame rotates at the Larmor frequency about the direction of the magnetic field (normally labelled the z-axis). This rotating frame therefore shares the z-axis with the laboratory frame, but its x'- and y'- axes (and hence its transverse plane) are rotating with respect to the x- and y- axes of the laboratory frame. Spins at the Larmor frequency are stationary in the rotating frame, while those at higher or lower frequencies move forwards and backwards respectively, and so gain or lose phase. The transverse motion of the NMV is nil in the rotating frame, leaving only the longitudinal motion as the NMV responds to the energy of the RF pulse (Figure 2.3b). By varying the strength (b_1) and/or the duration (t) of the RF pulse we can control the flip angle, θ. In the rotating frame the oscillating RF field becomes stationary – i.e. $\mathbf{b_1}$ is stationary. So the NMV can be thought of as precessing about $\mathbf{b_1}$ at the Larmor frequency. The Larmor equation applied to this situation is then $\omega = \gamma b_1$. Since the

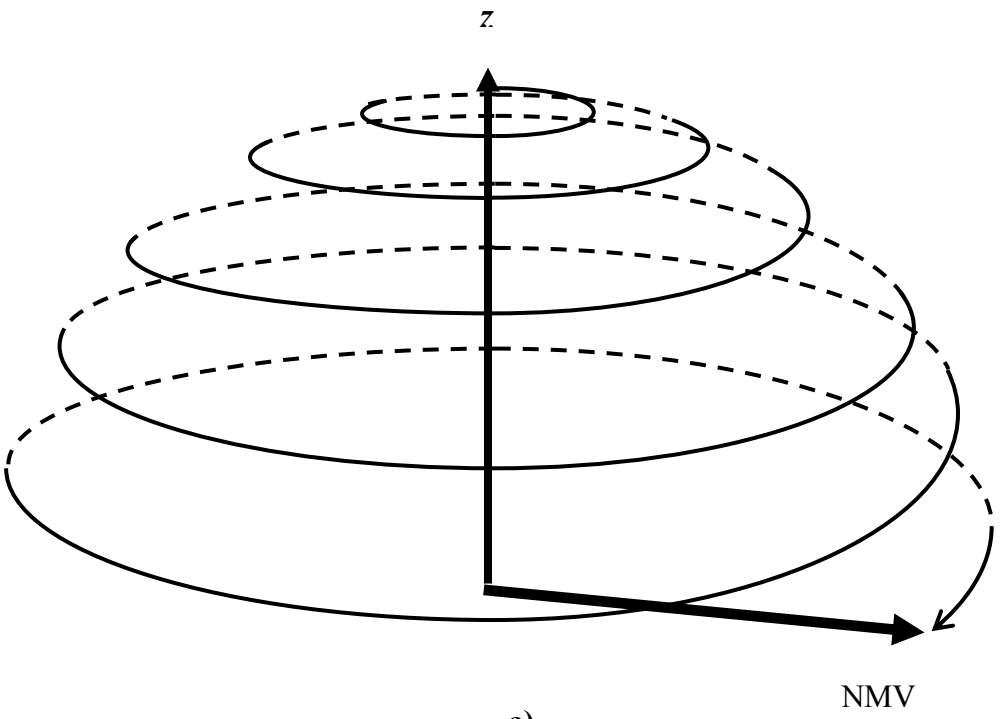

a)

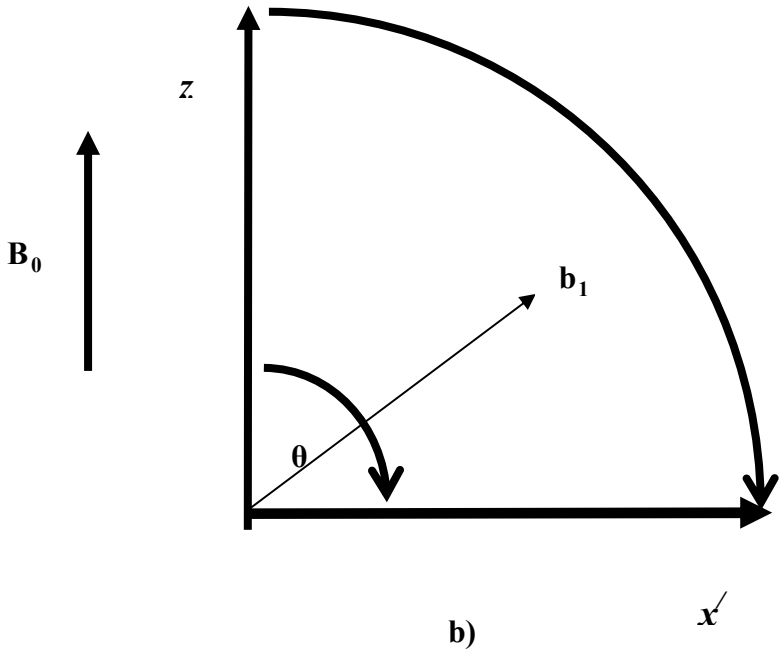

b)

Figure 2.3 Illustration of the spiral excitation of the NMV after the reception of an RF pulse as seen in a) the laboratory frame and b) the rotating frame. (From R. Watts MDPH 406 Lecture Notes.)

accumulation of phase – i.e. the flip angle - is described by $\theta = \int \omega dt$, we have here $\theta = \gamma b_1 t$. Typical flip angles are 90^o and 180^o, although other angles are sometimes used.

The NMR scanner has receiver coils that are sensitive to magnetization perpendicular to ***B.*** The NMV is rotating in the transverse plane of these coils, so an electromotive force is induced in them by this rotating NMV. The frequency of this induced emf is the Larmor frequency. The amplitude of the received signal decays exponentially as the individual spins rapidly de-phase through local field inhomogeneities caused by magnetic interaction effects. By observing the rate of decay of the signal as the NMV returns to its longitudinal alignment ($\theta = 0$) NMR can be used to infer information about the material encountered by the signal.

The decay of the transverse component is called "spin-spin relaxation", because it is achieved by the spins' magnetic interaction with their neighbours, which alters the magnetic field of each spin slightly, and therefore their respective Larmor frequencies. This leads to a loss of phase between the spins in the transverse plane. The recovery of the vertical component M_z is called "spin-lattice relaxation"; it is achieved by spins in the spin-down, excited state giving up their energy to the lattice structure and returning to the spin-up, ground state. Each relaxation process follows a prescribed exponential relationship, with a characteristic time where T_1 is the spin-lattice relaxation time constant and T_2 is the spin-spin relaxation time constant. If the RF pulse served to flip the NMV, with equilibrium value M_0, entirely into the transverse plane (i.e. $\theta = 90^o$), then the two relaxation equations describing the magnetization at time t are:

$$M_z(t) = M_0(1 - e^{-t/T_1}) \quad \text{, with } M_z(0) = 0 \qquad 2.6$$

$$M_{xy}(t) = M_{xy}(0)e^{-t/T_2} \qquad 2.7$$

Table 2-1 Recovery time constants for different tissue at B_0 = 1.5 T and 37 ^{o}C (human body temperature) (Haacke, et al. 1999)

Tissue	T_1 (ms)	T_2 (ms)
Grey matter	950	100
White matter	600	80
Muscle	900	50
Cerebrospinal fluid	4500	2200
Fat	250	60
Blood	1200	100-200

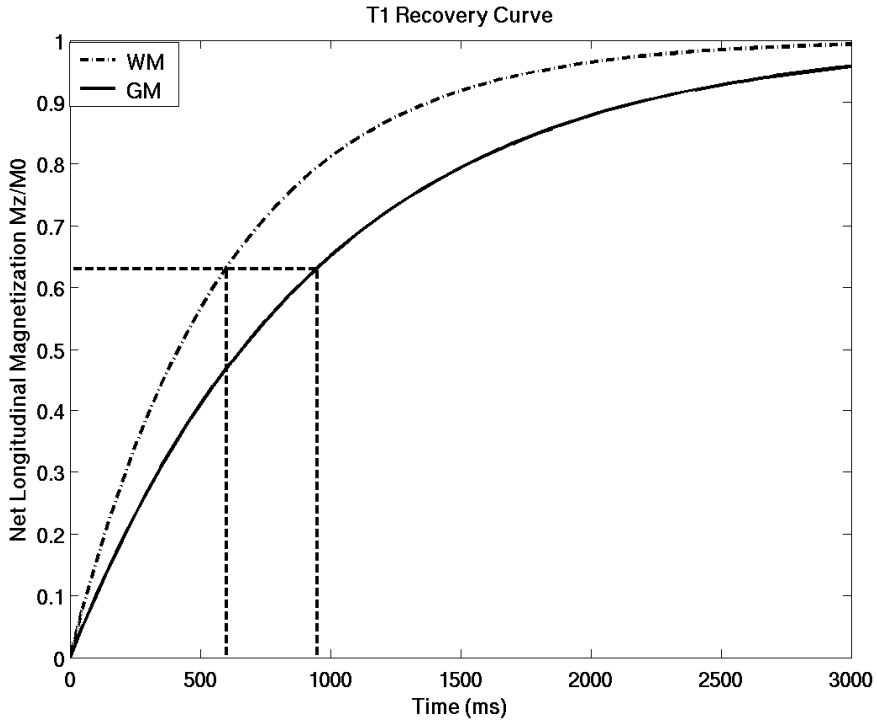

(a)

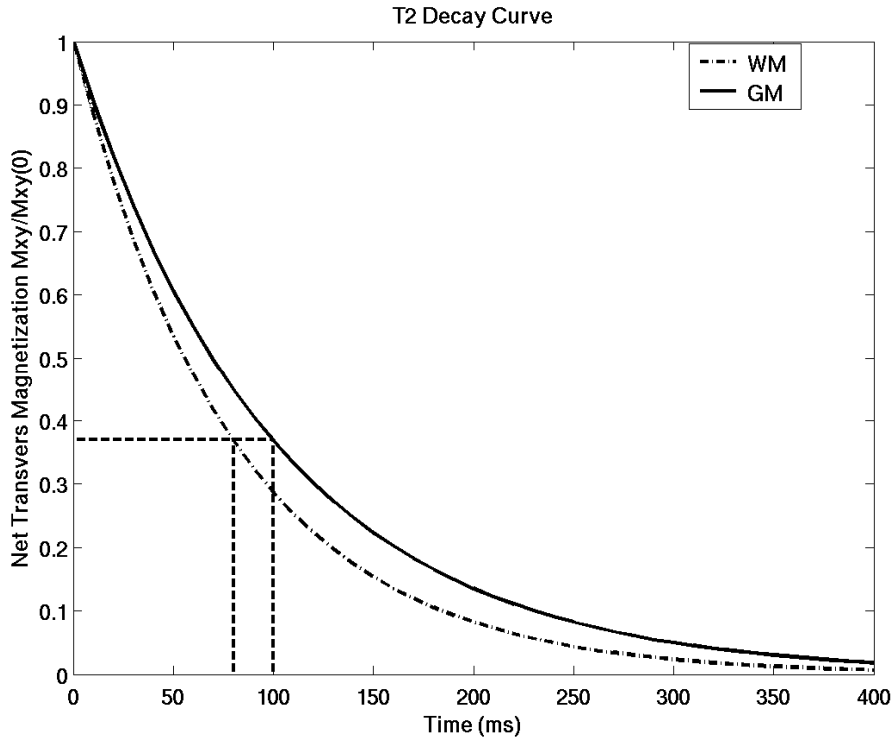

(b)

Figure 2.4 (a) The re-growth of the longitudinal component of magnetisation from the initial value Mz(0) to the equilibrium value M0. (b) The decay of the magnitude of the transverse magnetization from its initial value. (WM=white matter, GM=grey matter.)

Figure 2.4 illustrates how the longitudinal magnetization recovers from this situation while the transverse magnetization decays. These two processes are tissue dependent, with different tissues having different T_1 and T_2 values (Table 2-1). These differences are critical for MR imaging, since they are important sources of contrast between different tissues. By adjusting the imaging parameters to become sensitive to these differences contrast can be achieved.

2.2 Introductory Data Acquisition

While the relaxation of the NMV in principle contains the information being sought about the composition of the object, it is not practicable to measure this directly. Instead, the NMV is manipulated to produce "echoes" that can be successfully measured. Such manipulation is achieved by sending more RF pulses and/or by changing the gradient magnetic fields. The effect of both is similar: to re-phase spins that have lost phase, and thereby to create an echo of the original signal as the spins come progressively into phase with each other then go out of phase again. This echo signal is recorded. The timing, or sequencing, of the RF pulses, the gradient pulses, and the reading of the signal is critical. Pulse sequence diagrams are often used to show the inter-relationship between the different pulses.

2.2.1 Pulse Sequences

A simple pulse sequence is shown in Figure 2.5. In this example, after the initial 90° RF pulse the spins are in-phase, giving a strong signal. Inhomogeneities in the magnetic field cause small differences in spin frequencies with subsequent de-phasing and signal loss. The 180° pulse inverts the spins so that the higher precession frequency spins are now "behind" the lower frequency spins as they rotate in the transverse plane. The fast spins catch up with the slower spins in the same time interval as that between the 90° and 180° pulses. This is when maximum re-phasing has occurred, producing an "echo" of the original signal. This is the "echo time", T_E, at which the echo is recorded. The whole process can be repeated many times, and the time between the initiating RF pulses (the period of the sequence) is called the repetition time, T_R.

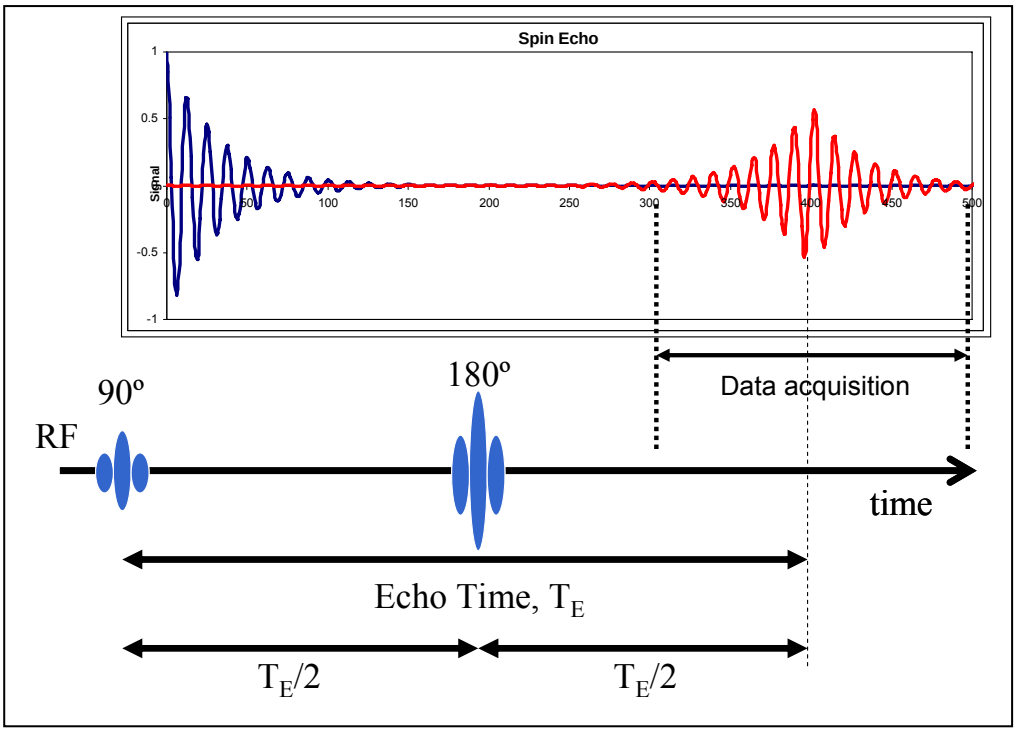

Figure 2.5 Pulse sequence diagram for a spin echo sequence showing the production and acquisition of an "echo". The echo occurs the same amount of time after the 180º refocusing pulse as the 90º pulse was before it. (From R. Watts MDPH 406 Lecture Notes.)

2.2.2 Spatial Encoding

The point of departure for MRI from NMR comes with the need for spatial separation – identifying which part of the signal comes from which part of the body – in order to form an image. The received signal must be spatially encoded in some way, and it is this feature that distinguishes MRI from NMR. Through the pioneering work of Paul Lauterbur (Lauterbur 1973) and Peter Mansfield (Mansfield, et al. 1976), controlled use of various magnetic field gradients modulates the frequency and phase of the signal to uniquely identify each voxel's contribution to the received signal. These gradients cause the magnetic field strength to become a function of position. Since the Larmor frequency is dependent on the magnetic field strength (Eq. 2.5), it too is a function of position. This means that the relaxation signals emitted by the object will have different frequencies depending which part of the object they come from. The single signal received by the coils will therefore comprise signals of many different frequencies and

phases, coming from different parts of the object. Fourier analysis is used to identify the spatial location of each component of the signal, and thus an image can be formed.

The localising magnetic field gradients are labelled G_x, G_y and G_z. These cause linear changes with distance in the longitudinal magnetic field $\boldsymbol{B}$, along the x-, y- and z-axes respectively. This is represented by the equation $\underline{B} = (B_0 + G_x x + G_y y + G_z z)\hat{\underline{z}}$. Different frequency (on-resonance) RF pulses will therefore excite different locations in the object.

Slice selection relies on this principle. If the scanner's magnetic field without gradients is B_0, Figure 2.6 shows the effect of a longitudinal gradient G_z. The field now varies linearly along the axis, effectively meaning each different z-coordinate has a different resonant frequency. By matching the frequency of the transmitted RF pulse to the Larmor frequency of the section of the object required, a longitudinal slice of data can be obtained.

The slice thickness can be altered either by changing the bandwidth of the RF pulse or by changing the gradients. Figure 2.7 shows how the latter achieves this. For a fixed bandwidth $\Delta\omega$, from the Larmor equation the slice thickness will be $\Delta z = \dfrac{\Delta\omega}{\gamma G_z}$.

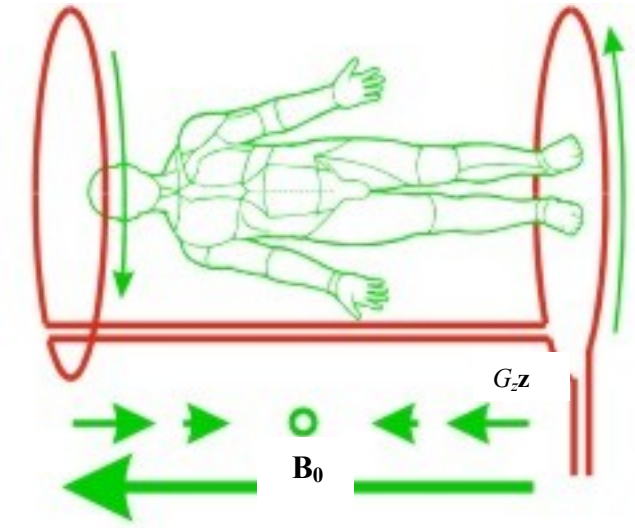

Figure 2.6 Effect of a magnetic field gradient G_z along the scanner's axis: the magnetic field now varies with position along the axis. (Arrows represent the additional field resulting from the G_z.) (From R. Watts MDPH 406 Lecture Notes.)

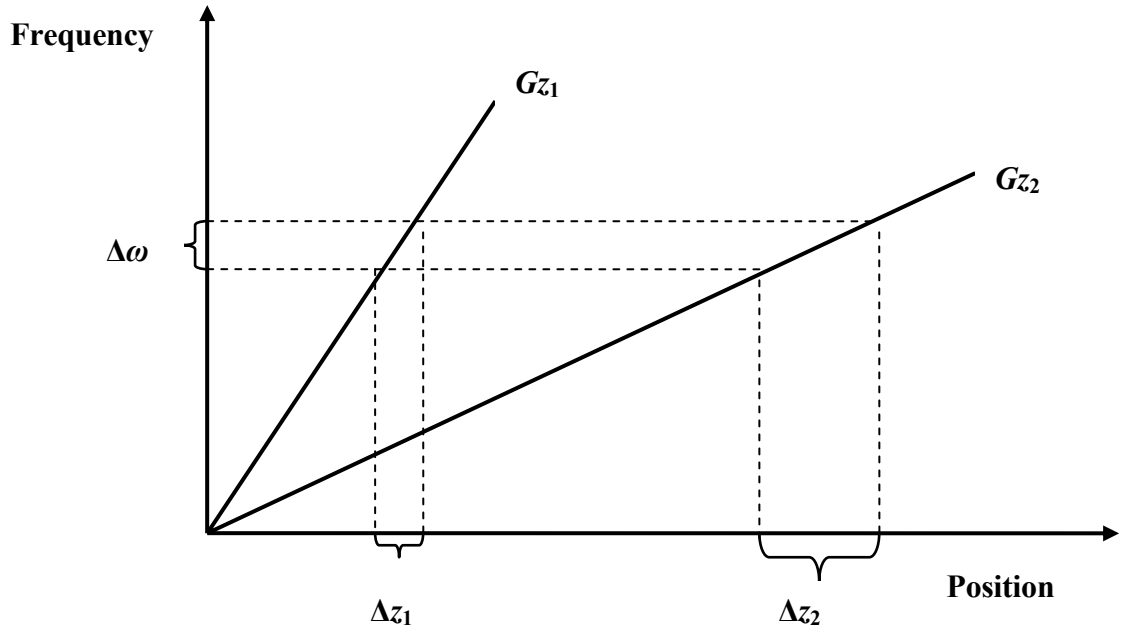

Figure 2.7 Plot of frequency of the transmitted RF pulse versus position along the direction of the slice-selection gradient. This shows how gradients of different strengths will select slices of different widths, using the same RF bandwidth *Δω*.

In order to locate a voxel, two more directions must be encoded in the slice data. This is done by using gradients G_x and G_y, and thus varying B in the other two directions as well. Figure 2.8 is an example of an imaging pulse sequence that uses an RF pulse to reverse the spins and achieve an echo. The sequence starts at the left of the diagram and progresses to the right. At the same time as the initiating 90^o RF pulse is transmitted the G_z, or slice select, gradient is applied. This excites only the spins in the corresponding section of the object. Once that has been achieved, some time is allowed for the spins to de-phase. Then a 180^o pulse is sent, with the same G_z gradient applied, to reverse the spins (as described above). They then re-phase, and while this is happening the G_x and G_y gradients are applied to encode the necessary spatial information. The signal is measured and recorded during an interval including the echo peak (when the spins are back in phase),. The process is then repeated to obtain data for another slice. In this way, a 3-d image can be constructed slice upon slice.

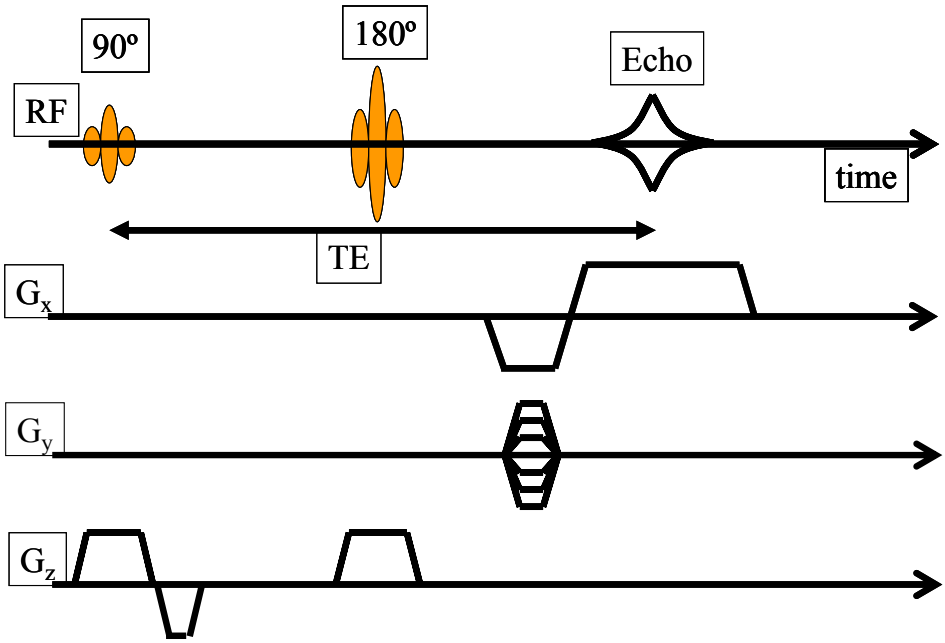

Figure 2.8 A spin echo pulse sequence with time along the horizontal showing the sequencing of the different gradients and RF pulses. (From R. Watts MDPH 406 Lecture Notes.)

The G_z pulses, which must be on while the excitation RF pulse is transmitted, make slice selection possible (*z*-axis localization). The G_y gradient, with an amplitude that varies with each repeat of the sequence "addresses" voxels in the *y*-, while the G_x pulse encodes spatial identification in the *x*-direction.

2.3 Image Reconstruction

Unlike other imaging modalities such as CT, the spatially encoded received signal does not form an image directly. The intensities of the received signal are received at different spatial frequencies rather than at different spatial locations. To achieve the latter and produce an image the data must undergo Fourier transformation.

2.3.1 k-space (Paschal and Morris 2004)

The "space" that the initial digital "image" is received and stored in prior to Fourier reconstruction is called k-space. A sequence such as the one in Figure 2.8 fills one line of the k-space matrix for each completed sequence, or each T_R. Once all the scans have

been completed and all the lines of k-space filled, the data are transformed to produce the visual image of that slice.

If a 2D object is represented by the function $f(x,y)$, and k_x and k_y are the relevant positions in k-space, then the received digital image can be written (McRobbie, et al. 2003):

$$F(k_x, k_y) = \iint_{x,y} f(x,y) \exp[i2\pi(xk_x + yk_y)]\ dxdy \qquad 2.8$$

Equivalently, the spatial image can be expressed in terms of the frequency data:

$$f(x,) = \iint_{k_x,k_y} F(k_x, k_y) \exp[-i2\pi(xk_x + yk_y)]\ dk_x dk_y \qquad 2.9$$

F and f are Fourier conjugates, so a wide *coverage* of k-space gives increased spatial *resolution*, while a high density of k-samples (k-space "resolution") gives wide spatial coverage (field of view).

The effect of the gradient fields is to gain information from a different part of k-space. In fact, where in k-space the data is being collected from depends directly on the amplitude and duration of these gradients. For any shaped gradient,

$$\left.\begin{aligned} k_x(t) &= \frac{\gamma}{2\pi}\int_0^t G_x(t')dt' \\ k_y(t) &= \frac{\gamma}{2\pi}\int_0^t G_y(t')dt' \end{aligned}\right\} \qquad 2.10$$

These equations show immediately that without the gradient magnetic fields (i.e. if $G_x = G_y = 0$), there would be only one point in k-space: the origin. This point represents full transverse magnetization, before any de-phasing and decay starts. Here, all the spins are in phase. As the gradients change with time, so do the k-values that the sampled data will be stored at, as given by Eq. 2.10. This creates what is called the k-trajectory, or the path through k-space as it is progressively filled.

2.3.2 Filling k-space

There are many possible trajectories for filling k–space, depending, among other things, which contrast is being sought. How this is done has a significant impact on the spatial, temporal, and contrast resolution of the resulting images (Paschal and Morris 2004).

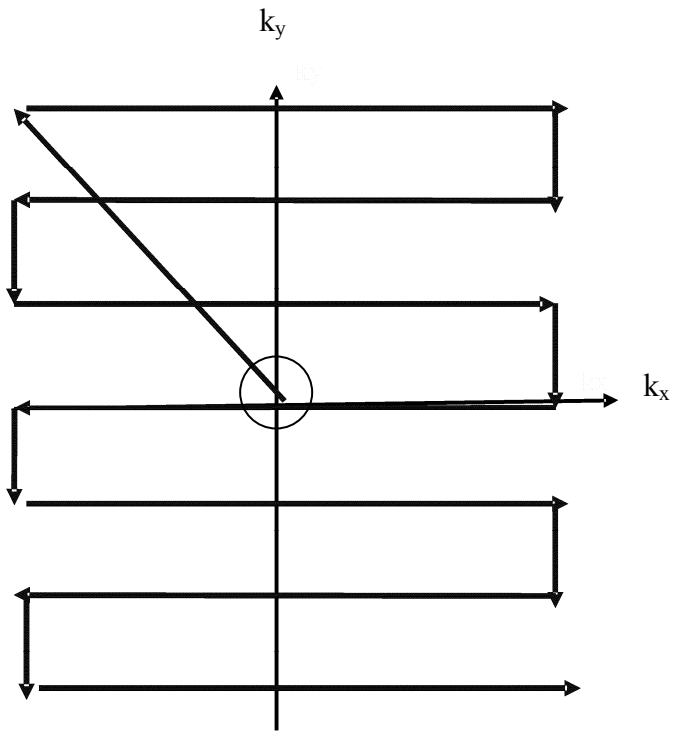

Figure 2.9 EPI k-space trajectory, showing the path taken as the k values change because of the changing gradients.

There are two main classes of contrast, and four major classes of trajectories.

1. Contrasts.

    a. Static. Typically these are used to produce high-resolution anatomical images. The contrast options include proton density, T_1, and T_2 weighted imaging.

b. Dynamic. These are used to study motion such as perfusion, diffusion and blood flow. These motions themselves establish endogenous contrasts that can be measured with MRI.

2. Trajectories.

a. Standard non-echo planar rectilinear. This is the most common MRI trajectory, achieved by holding k_y constant while a line of k_x is filled from a single RF pulse. A new value of k_y is obtained, and the process repeated. Thus k-space is filled one line at a time.

b. Echo Planar Imaging (EPI). A significant decrease in acquisition time is achieved by filling k-space quickly from a single RF excitation. This is usually the preferred option for data-intensive studies such as diffusion tensor imaging and functional magnetic resonance imaging. While it has the great strength of short acquisition times, it also has serious disadvantages, including signal dropout and distortion of the image due to field inhomogeneities (Paschal and Morris 2004). Figure 2.9 shows a schematic of the trajectory of this pulse sequence through k-space. EPI has several features:

- It is one of the fastest pulse sequences (Mansfield 1977), being able to acquire the data for a 2-d image in less than 100 ms.
- It produces excellent T_2 contrast, since T_R is generall >> T1. Then, the extended acquisition time from the single RF pulse means the longitudinal magnetisation has effectively fully recovered, so there is no T_1 contamination in the signal.
- The fact that all the data come from a single RF pulse places a limit on how long imaging can continue for before the exponential decay of the transverse magnetisation being recorded reduces the signal strength to a level where it is virtually indistinguishable from the noise. This limit is typically about 100 ms (Bernstein, et al. 2004).
- It has a high level of artifact (see next section).

c. Radial. This has the advantage of very good SNR. It also allows for the imaging of tissues with short T_2 , such as lung parenchyma, which need short T_E.

d. Spiral. Like EPI, these trajectories sweep quickly over the whole of k-space after a single excitation. They are more efficient than EPI, with no wasted data (such as when EPI "blips" down to its next k_y (see Figure 2.9)). A main disadvantage of spiral trajectories is that their acquired data points do not lie on a rectilinear grid, so these must be re-sampled into a Cartesian framework.

Although 3-d images are usually constructed slice-by-slice, a 3-d scanning of k-space is sometimes performed, producing a full 3-d image. This is done by using two phase-encoding gradients rather than the single one in 2-d imaging. This gathers data from all points in k-space and, using a 3-d fourier transform, produces the 3-d image. Because all the points in k-space contribute to the signal this gives better signal-to-noise (SNR) ratio than the slice-by-slice 2-d method. However there are two disadvantages with 3-d imaging:

a. Phase-encoding dimensions are more vulnerable to field inhomogeneities and motion artifacts than the frequency-encoding dimension. Since 3-d imaging has two phase-encoding dimensions as against 2-d imaging's one, it is more prone to these problems.

b. Obviously it will take longer to fill a 3-d k-space than a 2-d one. Head motion is therefore more likely during the 3-d acquisition, and this will cause distortions that pervade the entire image. With 2-d imaging, head motion will cause a misalignment between slices in single shot imaging, but this is easily corrected using registration techniques.

2.4 Artifacts

It is impossible to get a completely uniform B_0 field over the whole subject volume, mainly due to the interaction of the subject with the magnetic field which causes small changes in the field. Such imperfections can produce artifacts in the final image.

2.4.1 B_0 Inhomogeneities.

Large-scale inhomogeneities can cause geometric distortions by creating errors in the phase-encoded voxel "addresses". These errors effectively spatially shift the incorrectly encoded voxels, creating distortions. Small-scale inhomogeneities cause spins within a voxel to lose phase coherence and hence the signal intensity drops, causing incorrect contrast resolution.

2.4.2 Non-linearities in the gradient fields.

These cause errors in the k-space trajectories. Non-linearities in G_x cause errors in k_x which can result in a compressed image. Errors in G_y result in a skewed image. Errors in G_z can cause thinner slices to be imaged, with the resulting loss of signal intensity and SNR.

EPI pulse sequences are prone to the following artifacts (Bernstein, et al. 2004):

2.4.3 Magnetic susceptibility artifacts.

Changes in the magnetic susceptibility in a local neighbourhood – for example at an air-tissue boundary – cause small changes in the magnetic field. These only need to be as big as 1 part per million to cause serious spatial distortion and/or signal dropout. Care must be exercised in interpreting EP images near magnetic susceptibility boundaries.

2.4.4 Nyquist ghosts

"Ghosting", or repeating the image in a wrong location, is common with EPI. These arise from many different sources that lead to changes in signal amplitude, phase inconsistency, or displacement of k-space data. Typically these errors all lead to a mis-registration of alternate lines of k-space. When the positive- and negative-going lines in k-space do not match, $N/2$ ghosts can occur. This is when a ghost image appears shifted with respect to the main image by half the field-of-view. There are many techniques for reducing Nyquist ghosting, although some degree of ghosting can be expected in most EP images.

2.4.5 Eddy currents

Eddy currents form in the scanner itself, as a result of the rapidly switching G_x. The magnetic fields established by these eddy currents distort the B_0 field, thus reducing

image quality. Eddy currents can cause a shift in k-space, for example with the centre occurring later in the readout than expected. Such shifts can result in compression, shearing, or displacement of the image. Engineering compensations such as actively shielded gradients keep eddy current distortions to a minimum, though they can still at times lead to distortion with EPI.

3 Diffusion Tensor and Functional MR Imaging and Analysis

3.1 Diffusion Tensor Imaging

3.1.1 Background

The constant random (Brownian) motion of water molecules in the brain is often referred to as "self-diffusion" or just "diffusion". An example of diffusion is when an ink drop is placed in a container of water. The ink drop immediately starts dispersing isotropically, and occupies an ever-increasing spherical volume. In free diffusion, the mean squared displacement of a molecule is given by Einstein (Einstein 1905):

$$\langle r^2 \rangle = 6Dt \qquad 3.1$$

where r is the distance from the starting point (mm)
D is the diffusion coefficient ($mm^2\ s^{-1}$)
t is the time (s)

The NMR signal can be made sensitive to the diffusion of the water molecules in the brain (Carr and Purcell 1954). Bipolar magnetic field gradients refocus the spins and so remove the effect of inhomogeneities in B_0 as the spins diffuse to different locations. Now, the phase changes and resulting signal decay are due to the diffusion of the spins. Using suitable pulse sequences (such as that in Figure 3.1), the decay brought about by diffusion can be detected, and the relevant diffusion coefficients estimated. Diffusion effects on the NMR signal are represented by the following equation (Le Bihan 1995):

$$\frac{S}{S_0} = \exp[-(\gamma G \delta)^2 \Delta D] \qquad 3.2$$

where S is the received signal intensity
S_0 is the signal intensity with no diffusion gradients
γ is the gyromagnetic ratio of the tissue (radians $s^{-1}\ T^{-1}$)
G is the gradient strength ($T\ mm^{-1}$)
δ is the gradient pulse duration (s)
Δ is the time between the onset of the gradient pulses (s)
D is the diffusion coefficient ($mm^2\ s^{-1}$)

This equation shows how the strength of the received signal is related to the diffusivity, and is the basis for diffusion measurement using NMR (Le Bihan 1995).

In a homogenous fluid diffusion is isotropic, and D is characterized by a single value. In the brain, however, diffusion is often anisotropic, so D depends on the measurement direction, and is called the apparent diffusion coefficient (ADC) in that direction. Brownian motion can be represented by a 3×3 symmetric, positive-definite matrix (Basser, et al. 1994), usually called a "tensor". This is usually written as:

$$\mathbf{D} = \begin{pmatrix} D_{xx} & D_{xy} & D_{xz} \\ D_{xy} & D_{yy} & D_{yz} \\ D_{xz} & D_{yz} & D_{zz} \end{pmatrix}$$ where x, y and z are the measurement axes of the scanner.

The diagonal elements represent the diffusion coefficient along the respective measurement axes, while the off-diagonal elements are covariance, or "cross", terms. When the subject's anatomical axes are aligned with the scanner's x, y and z axes there is no covariance between the axes, and the off-diagonal terms drop out. The tensor is often diagonalized to find its eigenvalues, from which frame-independent diffusion measures can be derived.

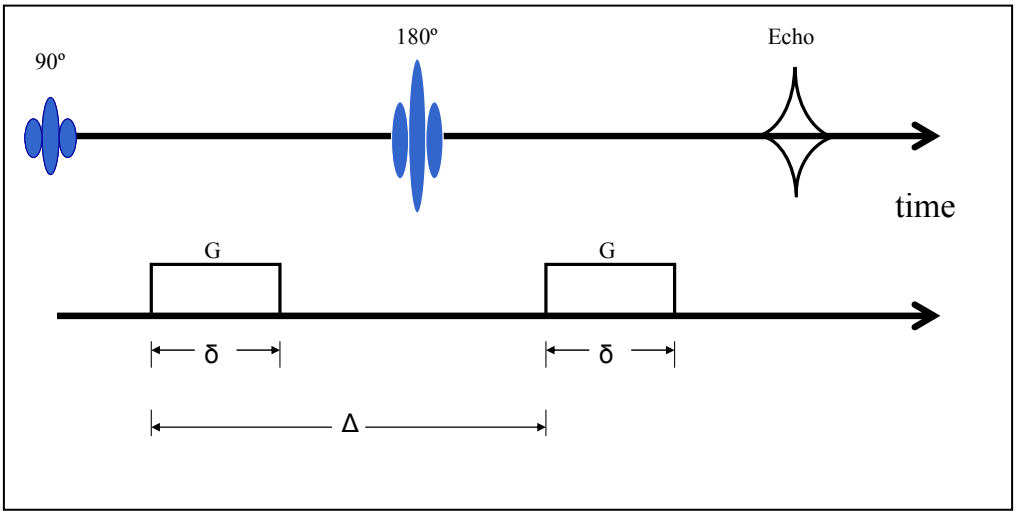

Figure 3.1 Pulsed gradient (Stejskal-Tanner) acquisition sequence for detecting diffusion effects. G is the gradient strength, δ the gradient duration, and Δ the time between the onset of the pulses. (From R. Watts MDPH 406 Lecture Notes.)

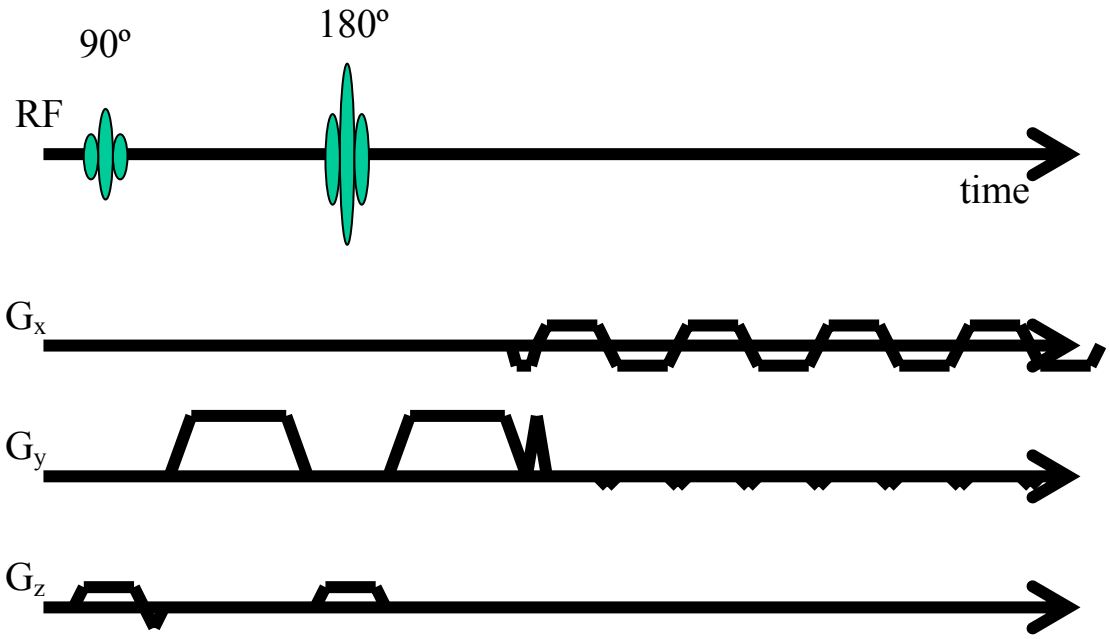

Figure 3.2 Diffusion-weighted EPI Pulse Sequence. (From R. Watts MDPH 406 Lecture Notes.)

In order to obtain a diffusion weighted image, it is necessary to combine a diffusion pulse sequence (as in Figure 3.1) with an imaging pulse sequence (as in Figure 2.8.). The pulse sequence therefore contains both imaging and diffusion gradients, as shown in Figure 3.2.

Ideally the effects of the different gradients would be independent, but in practice there is an interaction effect that must be accounted for. This is done using the "*b*-factor" (for isotropic diffusion), and the symmetric "*b*-matrix" (for anisotropic diffusion) (Le Bihan 1995). Methods of calculating the *b*-factor and *b*-matrix are detailed in the literature (Basser and Jones 2002; Mattiello, et al. 1997). For the Stejskal-Tanner pulse sequence shown in Figure 3.1, $b = \gamma^2 G^2 \delta^2 (\Delta - \delta/3)$.

Using the appropriate **b** matrix, and replacing the ADC D with the diffusion tensor **D**, Eq. 2.8 can be written as

$$\frac{S}{S_0} = \exp\left[-\sum_{i=1}^{3}\sum_{j=1}^{3} b_{ij} D_{ij} \right] = \exp\left[-\text{Trace}(\mathbf{bD}) \right] \qquad 3.3$$

where b_{ij} and D_{ij} are the elements of the *b*-matrix **b** and the diffusion tensor **D** respectively (Basser and Jones 2002).

For isotropic diffusion, where $D_{xx} = D_{yy} = D_{zz} = D$, and $b = b_{xx} + b_{yy} + b_{zz}$ =Trace(**b**),

$$\frac{S}{S_0} = \exp(-bD) \qquad 3.4$$

The *b*-factor is an operator-controlled parameter that must be appropriately chosen in order for optimal imaging to be obtained. Eq. 3.4 shows that while increasing the *b*-factor will increase the contrast in the image, it will also reduce the SNR, so a compromise must be reached. A value of b = 1000 s mm^{-2} is typically used in DTI. With the ADC in the brain being ~ 10^3 mm^2 s^{-1} this gives a value of bD of ~1. Eq. 3.4 shows that S/S_0 will then be ~ e^{-1}. This fraction is large enough S can still be detected, and small enough that contrast is evident between S and S_0.

While diffusion tensor imaging (DTI) is the state-of-the-art MR diffusion technique, diffusion weighted imaging (DWI) is also often used. While DTI yields the full tensor with its richness of information about the magnitude, direction and propagation of the diffusion (see below), DWI yields only the mean diffusivity - a measure of the magnitude of the diffusion. While DTI requires at least 6 diffusion gradient directions (though to compensate for low SNR usually more than 20 are used), DWI requires measurements in just three orthogonal directions. The advantages of DWI over DTI are its speed of acquisition, and that it is less demanding of the hardware.

3.1.2 Tensor Geometry

The diffusion tensor describes a geometric ellipsoid, with the three axis lengths possibly all different. (In the case of isotropic diffusion, as with the ink drop, the ellipsoid is a sphere.) This tensor contains information about the lengths and spatial orientation of the ellipsoid's axes, and therefore about the three-dimensional diffusion at that point. The axis lengths of the ellipsoid are proportional to the square roots of the three tensor eigenvalues, $\lambda_1 \geq \lambda_2 \geq \lambda_3 \geq 0$. If the ellipsoid's three orthogonal axes are aligned with the axes of the reference frame, the tensor is diagonal; if the ellipsoid is rotated with respect to the reference frame, the tensor contains symmetric off-diagonal elements to account for the rotation.

The dual requirement that they be symmetric and positive-definite means tensors are a specialised form of matrix, and do not form a vector space (for example, the negation of a tensor is not a tensor, since it is not positive-definite). Computational rules that apply

to vectors do not apply to tensors. This has implications for DTI analysis. Processing techniques such as de-noising and interpolation, and statistical tools to analyze the variability of tensors, model the noise, and allow collating of data from several subjects, are all important in the analysis of DT data. Conventionally, attempts to do this are hampered by several factors. These include the following (Arsigny, et al. 2006):

- Since the tensor eigenvalues represent physical diffusivity along the three spatial axes, they must be non-negative. However, the presence of noise in the MR signal causes some of the tensors to depart from the condition of being positive-definite. Ad hoc attempts to remove the spurious effects this causes (e.g. by setting all negative eigenvalues to zero) are not altogether satisfactory.

- Instead of analyzing the tensor as a whole, scalar features of the tensor (such as mean diffusivity *(MD)* and fractional anisotropy *(FA*)) are often considered in isolation. However, this results in a loss of information.

- Attempts to average a group of tensors using their Euclidean mean results in the "tensor swelling effect", where the determinant (which is proportional to the diffusivity) of this "mean" can be greater than the determinants of the original tensors. Tensors with high anisotropy are particularly susceptible to this swelling, with their ellipsoid being much "fuller" than it should be.

The underlying cause of these computational problems is that tensors do not belong to Euclidean ("flat") space. Euclidean space is a subset of Riemannian ("curved") space, and it is to the latter, but not the former, that tensors belong. Euclidean algebra must therefore be replaced by Riemannian algebra in tensor processing in order to both retain all the information in each tensor, and to prevent false results and conclusions from occurring when combining tensors.

Two recent approaches to processing the tensors in Riemannian space have shown promising results with both synthetic and clinical DTI data. One is to use affine-invariant metrics (Castano-Moraga, et al. 2007; Corouge, et al. 2006; Fillard, et al. 2005; Fletcher and Joshi 2004; Fletcher and Joshi 2007), with the following definitions:

Tensor logarithm:

$$\ln(\mathbf{S}) = \sum_{k=1}^{+\infty} \frac{(-1)^k}{k} (\mathbf{S} - \mathbf{Id})^k$$

where **d** is the vector of eigenvalues of tensor **S** and **I** is the identity matrix;

Tensor square root:

$$\mathbf{S}^{-½} = \exp(\tfrac{1}{2}(\log(\mathbf{S}))$$

Tensor norm:

$$|| \mathbf{S} || = \sqrt{trace(\mathbf{S}^{\mathbf{T}}\mathbf{S})}$$

Then the distance between two tensors $\mathbf{S_1}$ and $\mathbf{S_2}$ is given by:

$$\text{Dist}(\mathbf{S_1}, \mathbf{S_2}) = ||\log(\mathbf{S_1}^{-1/2}. \mathbf{S_2}. \mathbf{S_1}^{-1/2})|| \qquad 3.5$$

The second non-Euclidean approach is a simplification of the affine-invariant structure, using similarity-invariant metrics, which have been called *Log-Euclidean* metrics (Arsigny, et al. 2006). Here the distance is given by

$$\text{Dist}(\mathbf{S_1}, \mathbf{S_2}) = ||\log(\mathbf{S_1}) - \log(\mathbf{S_2})|| \qquad 3.6$$

This is computationally simpler and faster than the affine-invariant methods. The simple logarithmic transformation of tensors sends them into a new space with an algebraic structure defined on it such that tensors can now be treated as vectors without any loss of information or distortion of the data. This greatly simplifies the processing of tensors compared with affine-invariant structures, while still eliminating the difficulties of using a Euclidean structure. The one potential cost of this simplification is that results using Log-Euclidean metrics depend, in principle, on the coordinate system chosen. However, Arsigny et al. (Arsigny, et al. 2006) claim that one would need to change the coordinate system very anisotropically before this would become noticeable – far more than is the case in typical medical imaging changes such as from Montreal Neurological Institute (MNI) coordinates to Talairach coordinates.

Further, a new anisotropy, called *geodesic anisotropy (GA)* is defined in this non-linear space. It is:

$$GA(S) = \left(\sum_{i=1}^{3} (\log(\lambda_i) - \overline{\log \lambda})^2 \right)^{\frac{1}{2}} \qquad 3.7$$

where λ_i denotes the eigenvalues of diffusion tensor S and $\overline{\log \lambda}$ denotes the average of the logs of the eigenvalues (Corouge, et al. 2006; Fletcher and Joshi 2004). This value is based on the geodesic distance in Riemannian space between S and the closest isotropic tensor. Whereas the Euclidean *fractional anisotropy, FA,* is the standard deviation of the eigenvalues treated as linear scalars, *GA* is the standard deviation of the log of the eigenvalues. Another way of looking at it is that while *FA* is a measure of the normalized distance of *S* from its isotropic part using the matrix norm for the distance measure, *GA* measures this distance along a geodesic (Batchelor, et al. 2005).

In Riemannian space, the mean of a set of tensors is the tensor which minimizes the sum of squared distances to the set; and interpolating two tensors means finding the shortest line joining them.

The difference between the new definitions and the standard matrix ones is akin to the difference between interpreting numbers additively or as positive quantities multiplicatively.

A comparison between Euclidean and Riemannian algebraic operations is given in

Table 3-1 (from Pennec et al. (2006)). This Riemannian approach to DTI analysis is new, with one of the earliest works being in 2004 (Fletcher and Joshi 2004). Most neuroimaging tensor analysis is still being done in a Euclidean framework, typically by investigating various scalar quantities derived from the tensor. An example of such scalars is the average of the ADC values along each eigenvector. This average is called the mean diffusivity, *MD*. Other examples are the degree of anisotropy and the linear or planar propagation of the diffusion, calculated from the eigenvalues.

Table 3-1 Comparison of basic operations in Euclidean and Riemannian spaces

	Euclidean Vector Space	**Riemannian Space**
Subtraction	$\overrightarrow{xy} = y - x$	$\overrightarrow{xy} = \log_x(y)$
Addition	$y = x + \overrightarrow{xy}$	$y = \exp_x(\overrightarrow{xy})$
Distance	$\mathrm{dist}(x,y) = \| y - x \|$	$\mathrm{dist}(x,y) = \| \overrightarrow{xy} \|_x$
$x_{t+\varepsilon} = \exp_{x_t}(-\varepsilon \nabla C(x_t))$	$\sum_i \overrightarrow{\bar{x}x_i} = 0$	$\sum_i \log_{\bar{x}}(x_i) = 0$
$x(t) = \exp_{x_1}(t\overrightarrow{x_1 x_2})$	$x_{t+\varepsilon} = x_t - \varepsilon \nabla C(x_t)$	

Linear (geodesic) interpolation $x(t) = x_1 + t\overrightarrow{x_1 x_2}$

3.1.3 Tensor Scalars

Several of these quantities derived from the tensor are rotationally invariant, and therefore frame-independent. These quantities are used to calculate quantitative values of the diffusion process. Quantities derived from the tensor that are potentially useful for imaging can be classified into three groupings:

- apparent diffusion coefficients, which measure the "magnitude" of the diffusion;
- diffusion anisotropy indices, which measure the directional preference of the diffusion;
- apparent propagation measures, which quantify whether the diffusivity's propagation is more linear ($\lambda_1 >> \lambda_2 \approx \lambda_3$), spherical ($\lambda_1 \approx \lambda_2 \approx \lambda_3$), or planar ($\lambda_1 \approx \lambda_2 >> \lambda_3$). Diffusion following a single fibre bundle shows more linear diffusivity, while regions of crossing fibres, along with sheet-like structures, show more planar diffusivity (Westin, et al. 2002; Zhang, et al. 2003).

Some of the most commonly used metrics to describe diffusion are (Ennis and Kindlmann 2006; Kingsley 2006a; Westin, et al. 2002) :

a. Average Diffusion Coefficient:

$$MD = \mu = \tfrac{1}{3}(\lambda_1 + \lambda_2 + \lambda_3) \qquad 3.8$$

$$Norm = \sqrt{\lambda_1^2 + \lambda_2^2 + \lambda_3^2} \qquad 3.9$$

b. Anisotropy:

Fractional Anisotropy:

$$FA = \sqrt{\frac{3}{2}\frac{(\lambda_1 - \mu)^2 + (\lambda_2 - \mu)^2 + (\lambda_3 - \mu)^2}{\lambda_1^2 + \lambda_2^2 + \lambda_3^2}} \quad 3.10$$

Scaled Relative Anisotropy:

$$sRA = \sqrt{\frac{(\lambda_1 - \mu)^2 + (\lambda_2 - \mu)^2 + (\lambda_3 - \mu)^2}{6\mu^2}} \quad 3.11$$

Volume Fraction (Volume Ratio):

$$VF = 1 - \lambda_1\lambda_2\lambda_3 / \mu^3 \quad 3.12$$

Geodesic anisotropy:

$$GA = \left(\sum_{i=1}^{3} (\log(\lambda_i) - \overline{\log \lambda})^2 \right)^{\frac{1}{2}} \quad 3.13$$

c. Propagation:

$$Mode = \frac{\lambda_1\lambda_2\lambda_3}{[(\lambda_1 - \mu_1)^2 + (\lambda_2 - \mu_1)^2 + (\lambda_3 - \mu_1)^2]^{3/2}} \quad 3.14$$

$$c_l = \frac{\lambda_1 - \lambda_2}{\lambda_1 + \lambda_2 + \lambda_3} \quad \text{linear anisotropy} \quad 3.15$$

$$c_p = \frac{2(\lambda_2 - \lambda_3)}{\lambda_1 + \lambda_2 + \lambda_3} \quad \text{planar anisotropy} \quad 3.16$$

$$c_s = \frac{3\lambda_3}{\lambda_1 + \lambda_2 + \lambda_3} \quad \text{isotropy, with } c_l + c_p + c_s = 1 \quad 3.17$$

3.1.4 Tractography

Water is known to preferentially diffuse along WM fibres rather than transverse to them (Mori, et al. 1999). This causes the diffusion to be anisotropic as the motion of the molecules is freer longitudinally along the fibre tract and more restricted transversely across the tract. The principal axis of the ellipsoid, given by the principal eigenvector of the tensor, will be in the direction of the fibre tract. Thus, by suitably segmenting the brain and considering only WM, connecting up these principal eigenvectors can trace

the passage of fibre tracts through the brain. However, with the diameter of white fibre tracts (axons) being on the order of microns, and the resolution of DTI being mm, it is not possible to identify individual fibres. Nevertheless, where a sufficient number of fibres form a fibre bundle, DTI tractography can be used to follow these bundles and so investigate the connectivity structure of a particular brain. There are three main approaches used to do this:

1. *Deterministic* (Mori, et al. 1999). Here, the principal eigenvector of the diffusion tensor is taken to give the direction of the fibre bundle. This assumes that myelinated axons allow diffusion to occur more easily longitudinally than transversely. By connecting the principal eigenvectors from neighbouring voxels, estimates of the directions of fibre bundles can be drawn (Watts, et al. 2003). Each of these is a *maximum likelihood* pathway through the DTI data, but there is no associated measure of confidence in the location of this pathway, making interpretation difficult. Also, having a single maximum likelihood direction in each voxel means voxels that have several non-collinear fibre bundles are not well-modeled by these methodologies (Watts, et al. 2003).

2. *Probabilistic* (Behrens, et al. 2003). Whereas the tensor models the diffusion process, probabilistic tracking models the underlying fibre structure. In its simplest form, the simple partial volume model, the probabilistic model, like the tensor model, assumes that a fraction of diffusion is along a single dominant direction. Unlike the tensor, it assumes that the remainder is isotropic. Also unlike the tensor model, it allows for inherent uncertainty in the measurements, and builds a probability density function (*pdf*) for each parameter. The width of these distributions represents uncertainty in the direction of the diffusion. By repeatedly sampling the *pdfs* across the probabilities, estimates can be made of the probability that a fibre pathway (or streamline) that leaves 'seed voxel' *A* will pass through any other voxel. Each resulting probabilistic streamline is said to connect *A* to all points along its path (Ciccarelli, et al. 2006). The connectivity probability is found by dividing the number of probabilistic streamlines which pass through a voxel *B* by the total number of probabilistic streamlines leaving *A*. Although this simple model does not explicitly allow for non-collinear fibre bundles in the same voxel, this is implicitly accounted for by

the uncertainties built into the *pdfs*. Compared with deterministic tracking, probabilistic tracking has two other main advantages. Firstly, it does not require the severe streamline-stopping criteria which limits deterministic tracking's sensitivity in places like deep grey matter and cortical regions. Secondly, while a single noisy voxel often ends a deterministic streamline, probabilistic methods are robust to noise. Probabilistic tracking produces many more lines than deterministic approaches, and these need careful interpretation, especially where they might appear to show crossing fibres, which deterministic approaches do not. The distribution of connectivity from the seed point represents *confidence bounds* on the location of the most probable single connection. It is not a distribution of connections from the seed point.

3. *Riemannian* (Batchelor, et al. 2006; Corouge, et al. 2006). As well as the problem with multiple, non-collinear fibres in the same voxel mentioned above, another important practical limitation with tractography using Euclidean metrics is the lack of tools to quantify the results. While the degree of anisotropy of the tensors can be measured, and the direction of the principal eigenvector determined, the shape and geometry of the tract is not generally directly quantified. Batchelor et al. (2006) measure geometric invariants such as curvature and torsion to describe the shapes of curves, independent of their spatial position. This could assist in the classification of different fibre tracts, and in distinguishing tracts that pass close to each other. Corouge et al. (2006) represent the shape of tracts of interest by the geometry of the medial spine found using the tensor mean and variance. Such approaches are still in their infancy, but may provide a step forward in the use of DTI tractography.

3.2 Functional Magnetic Resonance Imaging

Functional MRI (fMRI) is used to show which parts of the cortex are activated by, or functionally related to, the performance of certain tasks.

FMRI is based on a rather surprising physiological observation: when a region of the brain is activated, the local venous blood is more oxygenated than before, despite the increased metabolic rate of oxygen in the region. This is because the increase in the cerebral blood flow (CBF) is even greater, creating a "surplus" of oxygenated blood.

Since deoxygenated blood has different magnetic properties from oxygenated blood, changes in the oxygenation level can be used as the contrast mechanism, using the BOLD, or Blood Oxygenation Level Dependent, technique (Aguirre, et al. 1998; Gati, et al. 1997; Zarahn, et al. 1997).

FMRI BOLD experiments often use a block design which involves presenting the subject with alternating blocks of two stimulus or task conditions, while simultaneously imaging the brain. Images are acquired every few seconds over a period of several minutes. Cortical areas which are differentially active in one condition compared with the other will experience changes in the amount of oxygenated blood. These changes will cause changes in the MR signal intensity over time that correlate with the stimulus/task cycles.

The underlying physiological premise is that neuronal activation changes the oxygen content of the blood. Because the signal is so weak, the set task and MRI scan sequence is repeated many times and the results averaged to increase the signal to noise ratio. Typically with the use of subtraction methods, comparing the signal during task performance with the signal during "rest", cortical regions associated with the task but not the "rest" condition can be identified with high spatial resolution (~ 2-4 mm). However subtraction methodology has some questionable assumptions when applied to neural activity and neuroimaging (Friston, et al. 1996). These include assuming that:

- The brain processes serially – i.e. neural structures supporting cognitive and behavioural processes combine in a simple additive manner. However the brain is known to act "in parallel" (Burton and Small 1999), with interaction effects possibly being significant.

- The two conditions being compared (for example "memory" and "rest") differ in only one important aspect. By then subtracting one response from the other, it is assumed that what remains is the activation for the condition of interest (such as memory). The validity of this assumption is still unknown, but it may be an over-simplification of a process as complex as the neuronal operation of the human brain. For example, we cannot be sure that no memory processing is being done during the "rest" period; nor can we be sure that only memory processing is being done during the "memory" block.

Alternative approaches to fMRI analysis such as conjunction analysis of interactions (Price and Friston 1997) are sometimes used rather than simple subtraction methodology.

One of the most significant limitations of fMRI is that what is being sought - the neuronal activations associated with a certain task - is not measured directly. The BOLD signal is used as a proxy. This has two major drawbacks:

- With the measured parameter being several physiological "steps" away from the desired one, there is the potential for unknown signal-altering processes to be present and thus to contaminate the signal. This is especially likely given that the process from the activated neuron to the change in the cell's oxygenation level is, at present, so poorly understood.

- There is a significant time lag of several seconds between the neuronal firing in response to a stimulus and the resulting change in the local blood oxygenation level. This has two important consequences. Firstly, it renders the time resolution of fMRI studies poor, and secondly it adds a level of complexity to the analysis, where the time lag must either be modeled or measured in some way. To model it risks forcing the data to conform to a formulaic reconstruction. This may result in the loss of important subtle departures from the model. To measure it accurately requires a lot of data, especially since the fMRI signal is so weak. Images used for measuring the hemodynamic response cannot then be used for the correlation analysis to determine the regions of activation.

There are also important cognitive psychological factors that must be considered in the design of the paradigms – for example, if a block design is used, will the subject start to subconsciously predict the next stimulus, thus changing their neural response? Is "rest" a suitable second task, since the brain is never completely at rest, and brain activity during this time will hinder the comparison?

As long as the interpreter pays attention to the design, acquisition and analysis pitfalls awaiting any fMRI study, it is an important tool in gaining further insight into the functional workings of the brain.

3.3 Image Analysis

The quantitative diffusion data produced by DTI and the intensity time courses produced by fMRI both lend themselves to statistical analysis. Group comparisons are then possible, considerably increasing the power of the study over a single subject investigation. However, before grouped imaging can be performed, the individual images must be spatially normalized.

3.3.1 Spatial Normalization

Spatial normalization is necessary for all population studies since no two individuals have the same shaped or sized brain. Normalization is the process that warps each brain to a standard template, thus allowing direct comparisons between localised regions. In single-subject fMRI, a weaker form of normalization called registration is still necessary to remove the effects of inadvertent head motion by the subject during the course of the scan.

There are two main approaches used in normalization: *label-based* and *non label-based* (Ashburner and Friston 1999). Label-based methods rely on the identification of spatial features or landmarks in the images, and finding transformations which superpose the set of labels on to each other. Non label-based methods find transformations which minimize the intensity differences between the object being normalized and the template it is being normalized to. Label-based approaches are typically (although not exclusively) operator-dependent, which is a weakness in terms both of objectivity (repeatability) and logistical constraints when processing a large number of images. Non-label based approaches are much easier to automate and by-pass the repeatability problem of using labels. However, the weakness in these methods is that if the object is very different from the template, local maxima or minima may be found instead of the global maximum or minimum, producing a distorted result. It is therefore important to visually check the results of any automatic intensity-based (i.e. non label based) normalization, as any sub-optimal normalization will be immediately apparent. Intensity-based spatial normalization involves two steps:

1. *Affine transformations*, or *rigid body transformations*, sometimes also called *image registration.* These are used to align the images to each other. This involves finding the matrices of translation, rotation, sheer and scaling that will

achieve the best fit of the two images. This achieves good overall shape similarity, but does not attempt to match every sulcus and gyrus.

2. *Non-linear warping* (Ashburner and Friston 1999). A linear combination of basis functions is found which best fits the object to the template after it has been subjected to affine transformation. This second step simultaneously minimizes:

    - The mean squared difference between the intensities of the object and the template

    - The squared distance between certain parameters and their known expectation (for example, the length of the brain must not end up unrealistically small). This constraint is sometimes called *regularization*, and provides control against the distortion of "over-fitting".

Image registration is relatively straightforward, and is available in all reputable neuroimaging software packages. However, non-linear warping is more complicated, and is not available in some packages. With single-subject functional MRI, this is not a problem, but when population averages and comparisons are needed, rigid body transformations may not achieve adequate geometric similarity for comparison. Normalization can never be done perfectly, and the less accurately this pre-processing step is done, the more problems it will cause later in the analysis. The SPM software (Worsley, et al. 1996) performs full spatial normalization, and was used for the population studies presented in this thesis.

3.3.2 Voxel Based Analysis (VBA)

This analyzes the data from each voxel separately, then pools the results in order to reach regional conclusions There are a number of different ways of approaching voxel based analysis, depending on which hypothesis is being tested. Two different analysis methods are described and used here. The first, using the boxer data, was a group comparison between a sample of the target population and a sample of control subjects. The second, with Parkinson's disease (PD) data, was a single group analysis, where changes in brain microstructure were tested for correlation with various neuropsychological variables. In both cases (the former involving ANOVA, the latter

linear regression) the analysis is done at the individual voxel level. When a voxel's metric value, averaged over the target subjects, is statistically significantly different from the value averaged over the controls, that voxel is highlighted on an image. Or, in regression analysis, where the metric value of a particular voxel shows a significant correlation with a neuropsychological variable from subject to subject, that voxel is highlighted.

However, there are two complications involved in any VBA. Firstly, as previously discussed, the geometric non-uniformity of brains makes normalization necessary. Secondly, with each voxel being about 2 mm × 2 mm × 5 mm, there are around 10^5 voxels in a brain. With this many pair-wise statistical tests, Type I errors ('false positives') become important (Moore and McCabe 2006). If the level of significance of the statistical tests is $\alpha = 0.05$, then there will be some 5 000 voxels deemed 'active' or 'positive' when in truth they are not. In order to rectify this situation and control the number of false positives, their occurrence must be quantified. There are two main measures of false positives, and the choice of the measure helps direct the method of control that will be used.

1. *Familywise Error Rate (FWER).* This is the standard measure of Type I errors. It is the chance of getting any false positives in the multiple test experiment. Another way of expressing this, if we know the number of tests (voxels) being made, is to state the expected number of false positives that will be produced, as in the above example. There are three main approaches to thresholding the images of test statistics in order to control the FWER.

    a. Bonferroni Correction. This conventional statistical approach of simply dividing the threshold *p*-value by the number of trials (i.e. voxels) undoubtedly controls the Type I error, but at the expense of introducing a large and unacceptable Type II error - i.e. severely reducing the power of the analysis (Benjamini and Hochberg 1995; Genovese, et al. 2002; Nichols and Hayasaka 2003). The reason for this is that Bonferroni has an underlying assumption that the trials are independent of each other. MRI data is almost always smoothed (typically with an 8 mm FWHM Gaussian kernel to increase the signal to noise ratio) before statistical tests are done. The values ascribed to a given voxel then also depend on

the values of the voxels around it, and Bonferroni is then too conservative. If, however, statistical tests were being done on unsmoothed data, then Bonferroni *may* be the appropriate correction technique, though even at the data acquisition stage it is possible that some inter-dependence is present.

b. Random Field Theory (RFT) (Poline, et al. 1997; Worsley, et al. 1992; Worsley, et al. 1996). RFT uses a new basic spatial unit in place of the voxel. This is the 'resel', or 'resolution element'. The resel is effectively the size of the Gaussian smoothing kernel. There will typically be several orders of magnitude fewer resels than voxels, which helps illustrate why the Bonferroni correction is too conservative. However, RFT is more sophisticated than simply using the Bonferroni algorithm with the number of voxels replaced by the number of resels. In determining the appropriate threshold statistic, RFT takes into account not just the 'peak height' (i.e. magnitude) of the statistic in a cluster of voxels, but also the extent of the cluster – i.e. how many voxels are in the cluster. The assumption here is that (for example) 50 voxels all grouped in a contiguous cluster are less likely to be false positives than 50 individually scattered voxels. The larger the cluster, the lower the threshold can be. While this adaptiveness to cluster extent, and therefore smoothness of the statistic image, is a strength of RFT, it also has some drawbacks. One is its assumption that the variables are Gaussian. If RFT is used, smoothing of the data is essential in order to ensure Gaussianity. Smoothing, though, reduces the resolution. Another drawback of RFT is its complexity, which makes it hard to understand and use appropriately. It is often used more as a 'black box', with all the dangers this entails. These include a lack of awareness and appreciation of the assumptions underlying RFT (Nichols and Hayasaka 2003). These researchers also used simulations to show that RFT thresholds are still "extremely conservative for all but extremely smooth data". The results of this method are also dependent on how "cluster" has been defined in the algorithm.

c. Resampling Methods. (Holmes, et al. 1996). These are non-parametric methods, including permutation techniques and bootstrapping. They, like RFT, are adaptive to smoothness but, unlike RFT, they require few assumptions. Both permutations and resampling methods work by resampling the data under the null hypothesis; the former without replacement and the latter with replacement. They resample not voxel by voxel, but the entire image as a whole. From this, the statistic of each image is computed and the maximum statistic recorded. This is repeated many times to form an empirical distribution of this maximum statistic. If α_0 is the allowed fraction of false positives, then the $100(1-\alpha_0)$th percentile of this distribution provides the threshold for controlling FWER. The chief weaknesses of these non-parametric methods are that they are computationally intensive, and they lack generality (Nichols and Hayasaka 2003).

2. *False Discovery Rate (FDR).* This measure of Type I errors is relatively new to statistics (Benjamini and Hochberg 1995), and has been successfully applied to neuroimaging (Genovese, et al. 2002). Whereas FWER is the ratio of false positives to total number of *tests*, FDR is the ratio of false positives to total number of *positives*. The rationale behind this is that often it is not the absolute number of false positives that is of interest, as much as the proportion of designated positives (i.e. rejections of the null hypothesis) that are actually false. Controlling the FDR entails ensuring that *on average* the FDR is no larger than a specified fraction, q. As with RFT and resampling methods, this approach is adaptive, in this case to the signal strength, adjusting the statistic threshold in order to keep q constant as the signal strength varies. Unlike Bonferroni, the focus is on the proportion of positives that are false, rather than the thresholding statistic itself. And, unlike conventional significance testing where the choice of α is arbitrary, the choice of q has physical meaning and can be rigorously interpreted and compared across studies. While conventional significance levels (0.01 – 0.05) are often used, this is by no means required, and values from 0.10 – 0.20 are reasonable in many situations (Genovese, et al. 2002). While this method of controlling Type I errors is more powerful than the FWER methods (Benjamini and Hochberg 1995), it becomes more conservative as correlations

between voxels increase, and is therefore most powerful for unsmoothed data (Genovese, et al. 2002).

3.3.3 The General Linear Model (GLM)

Analysis of both DTI and fMRI data entails the use of the GLM to find which voxels have statistically significant changes in their signals, thus indicating activation with fMRI, or structural differences with DTI. The GLM attempts to model the received MR signal at each voxel as a linear combination of stimuli (for fMRI) or conditions (DTI). The GLM at a single voxel can be written as:

$$z_n = \beta_0 + \beta_1 r_n^{(1)} + \beta_2 r_n^{(2)} + \beta_3 r_n^{(3)} + ... + \varepsilon_n \qquad 3.18$$

where Z_n is the received signal at time point n

β_0 is a (baseline) constant

$\beta_{1,2,\ ...,n}$ are the stimulus (or condition) weights

$r_n^{(j)}$ are the responses to the j different stimuli (or conditions)

ε_n is the error term, or residual

n = 1, 2, …., number of images

Rather than writing out the n situations we make use of matrix notation, where each row represents a new time point. Then:

$$\mathbf{z} = \mathbf{R}\,\boldsymbol{\beta} + \boldsymbol{\varepsilon} \qquad 3.19$$

where $\mathbf{z}$ is the vector of data (the signal vector)

$\mathbf{R}$ is the matrix of stimuli or conditions (the "design" matrix)

$\boldsymbol{\beta}$ is the vector of coefficients

$\boldsymbol{\varepsilon}$ is the vector of residuals

Note: $\mathbf{z}$ and $\boldsymbol{\beta}$ both depend on the voxel, while $\mathbf{R}$ is the same for all voxels. This design matrix can be presented graphically. Figure 3.3 shows the graphical depiction of the design matrix for 59 boxers and 12 controls.

Solving Eq. 3.19 for $\boldsymbol{\beta}$. using least squares gives:

$$\hat{\boldsymbol{\beta}} = [\mathbf{R}^{\mathrm{T}}\mathbf{T}]^{-1}\mathbf{R}^{\mathrm{T}}\mathbf{z} \qquad 3.20$$

These $\hat{\boldsymbol{\beta}}$, different at each voxel, can then be tested for statistical significance under the null hypothesis that $\boldsymbol{\beta} = \underline{\mathbf{0}}$. This is the basis on which voxels are identified as showing neuronal activation (fMRI), or structural differences between groups (DTI).

The GLM provides important flexibility in analyzing fMRI results. It is this flexibility that allows two different stimuli to be compared directly with each other (e.g. two different memory tasks). Each stimulus is modeled separately in the **R** matrix, with the β coefficient of each stimulus then tested for statistical significance under the null hypothesis that there is no difference between the two stimuli (i.e. $\beta_1 = \beta_2$). Ideally, the two stimuli should be as close to each other in terms of neuronal activity as possible, except for the single extra domain being investigated (e.g. working memory). Using a paradigm that involves two memory-like stimuli with one being more demanding than the other removes non-memory related activities such as vision and motor responses that a rest condition might not remove.

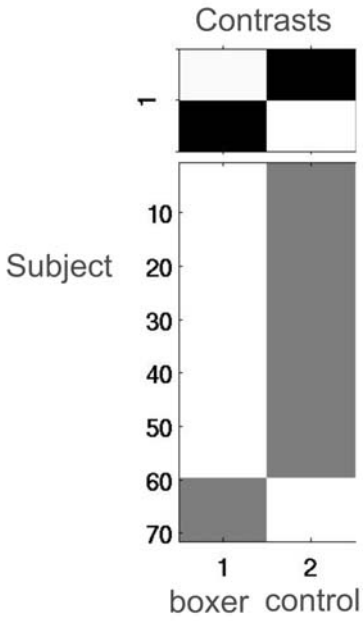

Figure 3.3 Design matrix for a 2-group study with the first 59 subjects in group 1 and the last 12 subjects in group 2.

4 Mild Head Injury: Univariate Diffusion Tensor Imaging of Professional Boxers

4.1 Background to Head Injuries

There is increasing evidence that even mild closed head injury (CHI) can cause considerable neural damage throughout the brain. Most of this damage occurs in the form of non-focal, non-haemorrhagic diffuse axonal injury (DAI) due to a combination of rotational shear forces and head-trauma-related metabolic changes within the brain. There is evidence for the presence of this type of injury after mild CHI from post-mortem examinations (Goodman 1994; Kane, et al. 1998) and perfusion abnormalities in functional imaging (Marks, et al. 2006). In contrast, conventional structural imaging techniques (CT, MRI) have demonstrated an insufficient sensitivity to DAI. Advances in structural imaging have led to applications such as diffusion weighted imaging (DWI) and diffusion tensor imaging (DTI), which have shown a much increased ability to detect microscopic non-haemorrhagic lesions that are below the detection threshold of conventional imaging.

This opens a path for examining the presence of neural injury after mild CHI in much greater detail. A major novelty of the study presented here is the use of professional boxers to investigate mild, non-acute head injury. The subjects in this study were asymptomatic. Such data are rare, and this is a major novelty in clinical research. Surprisingly, no other studies have applied DWI or DTI following mild CHI, possibly because it is unlikely to see effects from a single event. The application of DWI/DTI on a distriction of events allows the possibility of providing structural imaging evidence for DAI in mild CHI with increased accuracy and resolution. The contrast mechanism provided by these techniques allows the description of aspects of neural pathology after mild head trauma not easily accessible with other imaging methods. It could also be used to examine correlations between cerebral injury and motor performance. Recent data show that the instrumented assessment of eye and arm motor function can provide sensitive markers for neurophysiological dysfunction in the brain and further indicate that motor function may be much closer related to the functional integrity of the injured brain after mild CHI than psychometric status. The data from DWI/DTI imaging may be helpful in demonstrating this close relationship

between cerebral integrity and motor function more clearly (Heitger, et al. 2004; Heitger, et al. 2006).

While the occurrence of neural injury after CHI is well known (Meythaler, et al. 2001; Moseley 2000; Rabadi and Jordan 2001; Zhang, et al. 2003), the localisation of tissue damage has proven difficult due to the microscopic, and in the vast majority of lesions, non-haemorrhagic character of DAI. So far, functional imaging techniques such as fMRI (McAllister, et al. 1999) or SPECT (Nedd, et al. 1993) have been used to gauge the extent of neural injury after mild CHI. Whilst these techniques have been able to show perfusion abnormalities and cerebral dysfunction likely related to head-trauma-related neural injury, approaches to capture such injury with structural imaging have been less successful in terms of illustrating the presence of DAI. MRI imaging techniques such as T_2-weighted fast spin echo (FSE) and fluid-attenuated inversion recovery (FLAIR) sequences can demonstrate DAI, but their limited sensitivity to this minute injury frequently leads to an underestimation of the extent of the injury (Brandstack, et al. 2006; Huisman, et al. 2003; Shiga, et al. 2006). This situation has changed with the development of diffusion-weighted imaging (DWI) and the related diffusion tensor imaging (DTI).

Voxel-based analysis (VBA) of DTI data was used in this study to better understand the distribution of microscopic injuries throughout the brain. This may lead to improved clinical diagnoses of brain damage, and better management of cumulative brain damage resulting from repeated but non-severe blows to the head.

It is difficult to reliably detect mild traumatic brain injury (TBI) using CT and conventional MRI (Huisman, et al. 2004; Jantzen, et al. 2004). This is because the effects of TBI on cell tissue are often microscopic and diffuse (Huisman, et al. 2003). There are many reported cases of patients who had normal-appearing CT and/or MRI scans but later presented with unmistakable symptoms of TBI (Goetz, et al. 2004; Wu, et al. 2004; Zhang, et al. 2003). Similarly, EEG can be used to detect pathologic unspecific alterations with high accuracy, but is not useful for specifying the findings for an exact diagnosis (Pointinger, et al. 2002). In this study DTI was used to investigate the microscopic abnormalities of the brains of professional boxers. Because DTI measures diffusion, and diffusion is sensitive to microstructural changes, DTI is

able to detect these changes where other imaging techniques may fail. A recent study reported statistically significant increases in the whole-brain *MD* of boxers compared to controls. It also revealed an increase in the spread of the boxers' distribution of coefficients compared to the controls' distribution, suggesting greater heterogeneity of diffusion within the boxers. Furthermore, these increases in diffusion were found to occur before brain abnormalities appeared on conventional MR images, establishing diffusion imaging as an important tool for monitoring the neurological health of boxers (Zhang, et al. 2003).

4.2 Materials and Methods

In vivo data were acquired from 81 professional male boxers (age range 20–42 years, median age 28 years) and 12 male control subjects (22–31 years, median age 25.5 years). The control subjects were free from neurological disease and had no boxing history. Informed consent was obtained from all participants. Imaging protocols were approved by the institutional review board. This was part of a screening program that assessed boxers with no symptoms of neurological damage. Conventional MRI of these subjects produced negative or nonspecific findings, including cavum septum pellucidum, subcortical WM disease, and periventricular WM disease. Whole-brain scans were performed on two GE 1.5T MRI scanners (General Electric Medical Systems, Milwaukee, WI, USA) with 22 mT/m gradient strength. A quadrature head coil was used, and in all cases the section thickness was 5 mm, with no intersection gaps. A 2D spin-echo EPI acquisition was used with TE/TR = 100 ms/12 s. An acquisition matrix of 128 × 128 × 30 and 1.7 × 1.7 × 5 mm^3 voxels in 26 gradient directions with *b*-values of 815–1152 $s.mm^{-2}$, and six acquisitions with no diffusion weighting was used. The total acquisition time was 6 minutes 24 seconds.

All images were warped, or spatially normalised, to a standard Montreal Neurological Institute (MNI) template using Statistical Parametric Mapping (SPM) (Worsley, et al. 1996) with the SPM2 package. The images were then smoothed using an 8 mm FWHM Gaussian kernel.

To test whether normalisation was effected by the choice of template, three different templates were selected initially – EPI, T_2 and FA. The resulting group analyses identifying regions of brain abnormalities were not sensitive to the choice of template.

All results presented in this chapter used the EPI template, since an EPI sequence was used to acquire the DTI data.

Both parametric and non-parametric analyses were performed. SPM2 was used for the parametric analysis, and SnPM2 for the non-parametric. Parametric analysis assumes the variables being tested – in this case *MD*, *FA* and *mode* – have a known distribution. SPM2 assumes a normal distribution for general linear modeling. Once model parameters have been estimated, they can be used in a variety of statistical tests such as two-sample *t*-tests and regression against a covariate. Parametric analysis is computationally fast, flexible, and widely used. However, if there is evidence of extreme non-normality of the distributions, a better option is to use non-parametric techniques (Holmes, et al. 1996; Nichols and Holmes 2002). These techniques make far less stringent assumptions about the distributions of the data, they are applicable where parametric techniques are not, and they are conceptually straightforward. However, the price is computational speed. For example, using a 3GHz Pentium 4 processor, analysis of the boxer data with SPM2 took a few seconds; with SnPM2 it took about 40 minutes. Futhermore, nonparametric tests generally have less power than parametric tests when the assumptions of the latter are satisfied. Non-parametric analysis of these data was used as a benchmark comparison because with so few control subjects, it was not meaningful to test the parametric model's assumptions of normality.

With the boxer data there were two possible confounding variables. Since the MR images were collected on two different scanners, there could be a confounding scanner effect. A strength of DTI is that it measures physical diffusion quantities, from the ratio of the signal intensities with and without diffusion weighting respectively. As long as the two scanners were calibrated correctly there should not be a confounding effect in the data. This is in contrast to standard MRI which records relative magnitudes from which the image is formed. This makes inter-site image comparisons difficult with standard imaging. With inter-site DTI studies it is still important to check for a possible scanner effect. The second confounding variable was subject age, which could cause some unknown and unwanted effect (Chun, et al. 2000).

These possible effects were tested for in two different ways in this study. The first was analytic, using analysis of covariance (ANCOVA) to model and remove these possible effects, with the scanner and subject age in years treated as confounding variables. The

other approach, used with the non-parametric analysis where ANCOVA is not part of the SnPM package, was to manually remove some of the subjects in order to make the data more homogeneous in terms of subject age. To achieve the same age range in both the boxer and control groups, 22 boxers were removed, leaving a study comparing 59 boxers with 12 controls. A similar approach was used with respect to the scanner, where the 50 boxers and 7 controls who were scanned on the same scanner were analysed separately.

In the full parametric study, once the significant clusters had been identified in SPM2 the coordinates of the most significant voxel in each cluster were used to identify that voxel as being within the WM or gray matter (GM). This was done using the predefined WM/GM templates of a normal brain in the FreeSurfer software based on the theory of (Fischl, et al. 2001) and (Witzel, et al. 2001), and then checked against the segmented images of the subjects of this study as produced in the upgraded image segmentation procedures of SPM5. The appropriate average *MD* or *FA* values for the boxers and the controls at each cluster maximum were then tabulated.

4.3 Results

4.3.1 Normalisation

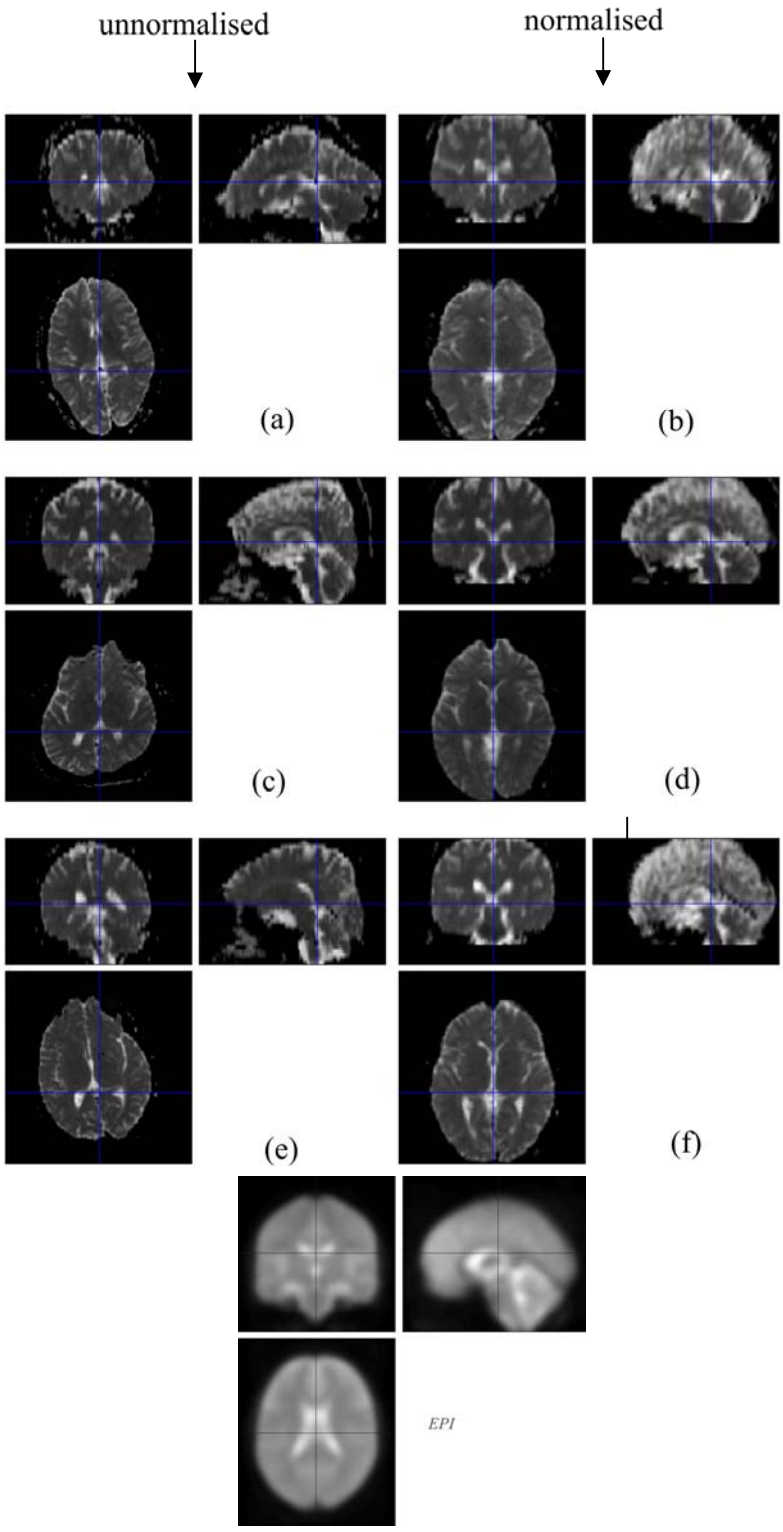

Figure 4.1 3-section sets of of 3 different unnormalised boxer images (a, c, e) and their respective normalised images (b, d, f). The EPI template used for normalisation is also shown.

Figure 4.1 illustrates the effects of spatial normalisation. Brains with different shapes and orientations (a, c and e) are warped using rigid body and non-linear transformations into the same space with approximately the same shape (b, d and f), allowing inter-subject comparisons.

4.3.2 Allowing for scanner and age effects

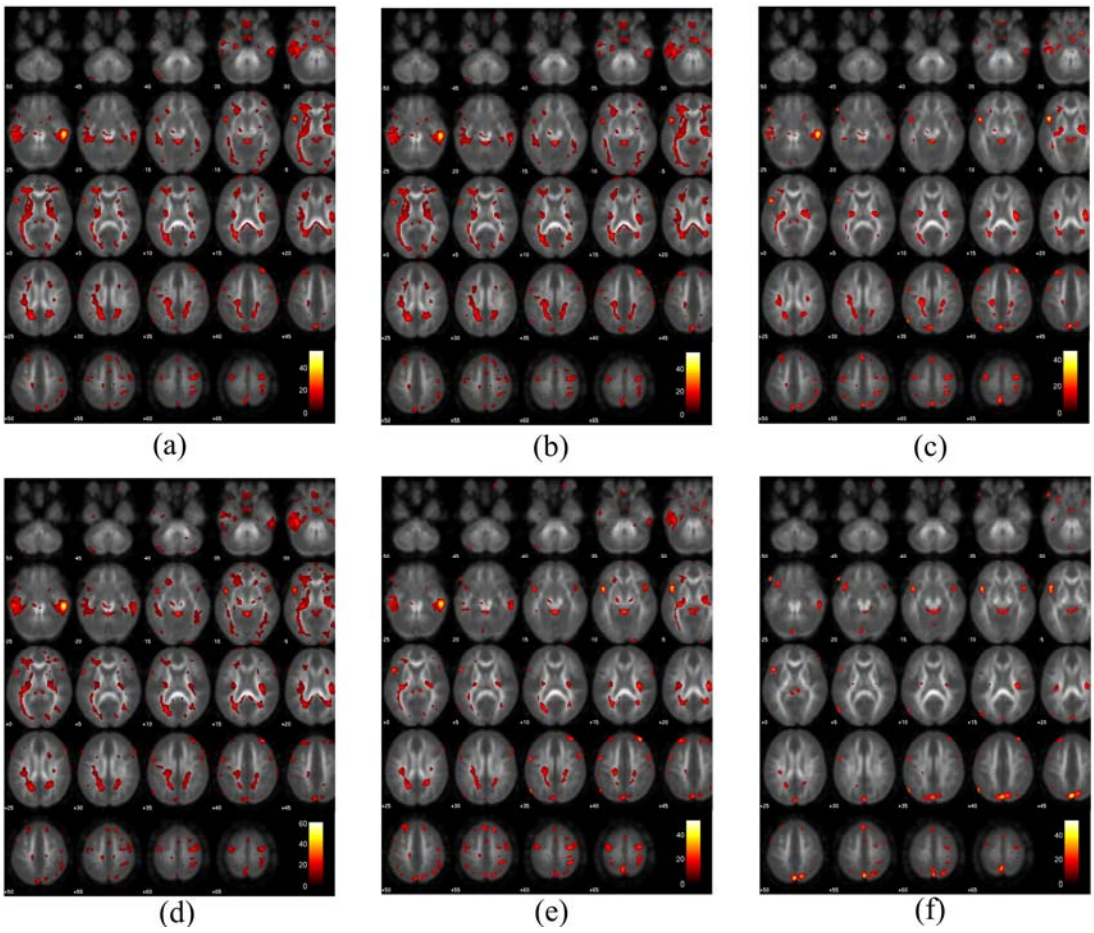

Figure 4.2 Coloured regions show where the mean diffusivity *(MD)* of the boxers is statistically significantly different from the *MD* of the controls, when analysed using ANOVA on the full dataset (a); ANCOVA on the full dataset with subject age as the confounding variable (b); ANCOVA on the full dataset with scanner as the confounding variable (c); ANOVA on the age-restricted dataset (d); ANCOVA on the age-restricted dataset with scanner as the confounding variable (e); and ANOVA on the scanner-restricted dataset. In all analyses, multiple comparisons were accounted for using a false discovery rate of 0.05.

Figure 4.2 (a) shows the results of ANOVA of the full group with no allowance for age or machine effects. Figure 4.2(b and c) show the results of analytical removal of the age effect and scanner effect, respectively. Qualitatively, the age effect is almost nil. While there is a small scanner effect (Figure 4.2(c)), it is primarily one of degree rather than substance, with some of the clusters identified in Figure 4.2(a) being reduced in size in Figure 4.2(c).

Figure 4.2(d and e) show results of analysis on the age-compatible dataset created by manually removing boxers with ages outside the range of the controls. When compared with Figure 4.2(a), there is little observable difference in the ANOVA results of the two datasets. Furthermore, performing an analytical scanner effect removal on the truncated dataset made little difference (Figure 4.2(e)). Figure 4.2(f) shows the results of manually removing the scanner effect by restricting the dataset to those who were scanned on the same scanner. As expected, since there were now only 7 controls, this shows a serious loss of statistical power.

Thus there is some justification for using either the full dataset without any corrections, or the age-restricted dataset without any corrections for machine. The reasons these emerge as the best two options are two-fold:

- There are two serious drawbacks with an analytical consideration of covariance using ANCOVA. Firstly, analysis of variance or covariance is a two-tailed test, whereas usually in these diffusion studies only one-tailed tests are desired, as the direction of change is generally known. For example, *MD* generally increases with non-acute brain damage, but if there is any decrease this needs to be separated out, rather than conjoined in one overall result. Secondly, ANCOVA is not one of the options in SnPM, so comparison between parametric and non-parametric analyses would not be convincing if one of them allowed for covariate effects and the other did not.

- Manually removing the scanner effect by truncating the dataset is not a good option in this study because of the loss of statistical power.

4.3.3 One-tailed t-tests of full group of 81 boxers and 12 controls

There were regions of increased *MD*, decreased *FA*, and decreased *MD* in the boxer group compared to the controls. These regions included the lower brain, the splenium, and cortical regions located laterally and dorsolaterally in both the frontal and posterior lobes. Any apparent differences detected near the edge of the brain should be interpreted with caution because of the possibility of susceptibility and misregistration artifacts in this region. No regions of increased *FA* were detected.

Figure 4.3 shows regions of significantly decreased *FA* were similar to those with increased *MD*. The decreases in *FA* were consistent over neighbouring slices and were located primarily in the WM (Table 4-1). Regions of decreased *FA* and/or increased *MD*, including those that exhibited both effects simultaneously, included the midbrain, internal capsule (including the posterior limb), putamen/globus pallidus, medial temporal lobe, inferior frontooccipital fasciculus and inferior longitudinal fasciculus, and the cerebral peduncle/corticobulbar/corticospinal tracts.

Both the boxers and controls showed regions of positive correlation between the *MD* and age (Figure 4.4). This effect appears to be stronger in the boxer group throughout multiple cortical and subcortical regions, particularly in cerebellar regions, with a strong, symmetric correlation of *MD* with age on the lateral periphery of both cerebellar hemispheres. Tests for negative correlation of *MD* with age for boxers and controls were both negative.

The results showed noticeable lateral symmetry in the brain abnormalities displayed by the boxers.

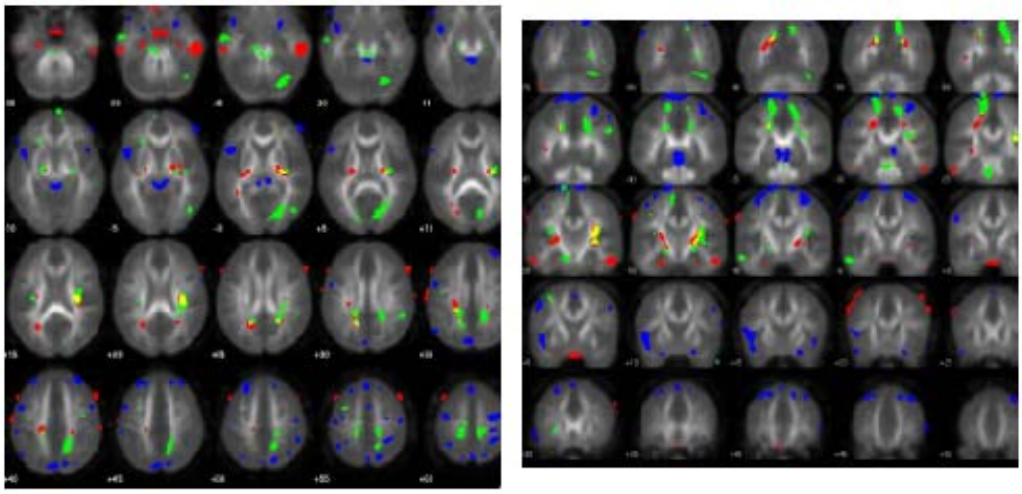

Figure 4.3 Coloured regions showing where the *MD* and *FA* values of the boxers' brains are statistically significantly different from the controls' ($p < 0.001$), axially and coronally. These regions are superimposed on an average *FA* map of normalised, undamaged brain. Slices are 5 mm apart. Red represents increased *MD*, green is decreased *FA*, yellow is the overlap of increased *MD* and reduced *FA*, and blue is decreased *MD*.

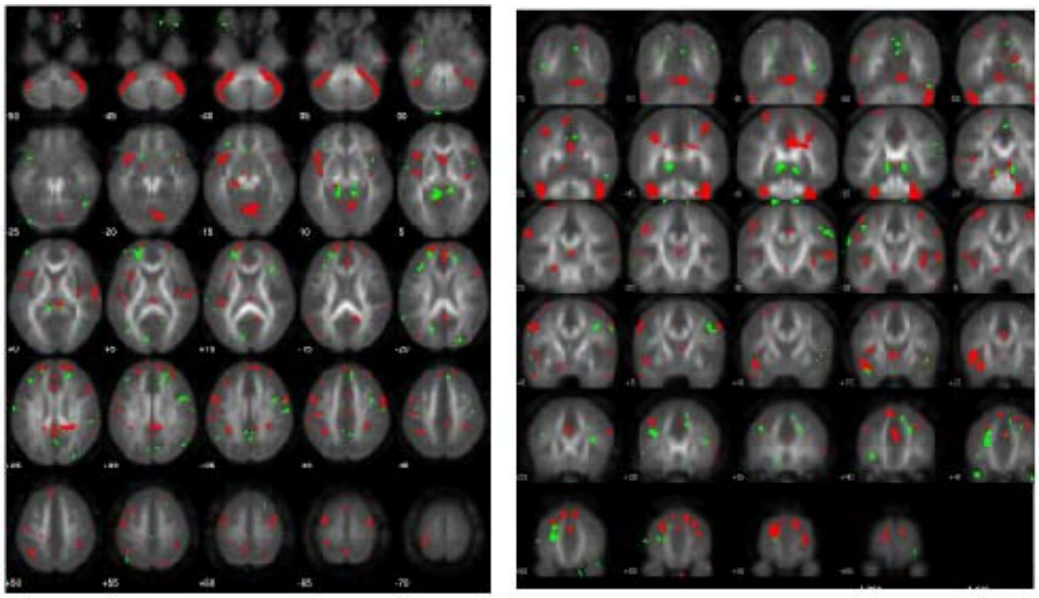

Figure 4.4 Positive correlations between *MD* and age for boxers (red) and controls (green) in axial and coronal sections. Regions of statistically significant correlation ($p < 0.001$) are superimposed on an average *FA* image of normalised, undamaged brain to contrast WM and GM.

Table 4-1 Statistically significant clusters where boxers' values of *FA* are less than the controls.*

Cluster max							*FA*		
x	**y**	**z**	**Tissue**	**Region**	**Corr.*p***	**t vox**	**Boxers**	**Controls**	**% dec.**
14	-60	42	WM	Precuneus	0.000	5.50	0.32 ± 0.04	0.35 ± 0.07	9
28	-72	-22	GM	Declive	0.000	4.97	0.22 ± 0.02	0.25 ± 0.02	10
16	-84	2	WM	Cuneus	0.000	4.93	0.28 ± 0.03	0.32 ± 0.05	14
-12	-20	-24	WM		0.000	4.11	0.46 ± 0.04	0.49 ± 0.06	6
46	-76	-4	GM	Mid. Occip. Gyrus	0.000	4.47	0.24 ± 0.03	0.28 ± 0.03	12
-12	-28	64	WM	Sub-gyral	0.000	4.72	0.31 ± 0.05	0.36 ± 0.04	15
52	-46	30	GM	Supramarginal Gyrus	0.000	4.03	0.23 ± 0.03	0.28 ± 0.04	17
-34	4	52	UNC	Mid.Frontal Gyrus	0.002	3.96	0.26 ± 0.04	0.29 ± 0.03	11
-34	-20	16	UNC	Insula	0.008	3.64	0.30 ± 0.04	0.34 ± 0.05	10
-26	28	-8	WM	Inf Frontal gyrus	0.009	3.61	0.34 ± 0.04	0.37 ± 0.07	7
22	-78	-42	WM	Pyramis	0.021	3.69	0.29 ± 0.04	0.32 ± 0.04	10
-42	-14	38	UNC	Precentral gyrus	0.147	3.92	0.27 ± 0.03	0.30 ± 0.05	12

Table 4-2 Statistically significant clusters where boxers' values of *MD* are greater than the controls.*

Cluster max							*MD* ($\times 10^{-3}$ mm^2 s^{-1})		
x	**y**	**z**	**Tissue**	**Region**	**Corr p**	**t vox**	**Boxers**	**Controls**	**% inc.**
-26	-16	-32	UNC	Sub-gyral	0.000	4.10	0.79 ± 0.08	0.67 ± 0.11	17
34	-22	18	GM	Insula	0.000	4.07	0.73 ± 0.06	0.65 ± 0.06	13
-24	-18	6	WM	Extra-nuclear	0.000	3.93	0.62 ± 0.03	0.56 ± 0.11	11
-28	-62	14	WM	Sub-gyral	0.000	3.92	0.75 ± 0.05	0.67 ± 0.05	12
26	-54	24	WM	Sub-gyral	0.000	3.60	0.72 ± 0.05	0.66 ± 0.03	10
24	-32	38	WM	Sub-gyral	0.016	3.45	0.64 ± 0.04	0.59 ± 0.05	9
-40	-48	0	WM	Sub-gyral	0.038	3.49	0.70 ± 0.04	0.63 ± 0.05	10
28	-16	-28	GM	Parahipp. Gyrus	0.094	3.86	0.80 ± 0.05	0.74 ± 0.05	9

* Clusters are recorded in decreasing order of their statistical significance (corr. *p*). (x,y,z) are the Montreal Neurological Institute (MNI) coordinates (in mm) of the most significant voxel in each cluster. That voxel is then identified as being white matter (WM) or grey matter (GM). 'UNC' signifies a voxel that was unable to be classified. 'corr *p*' is the corrected *p*-value for that cluster. 't vox' is the *t*-value for the given maximum voxel. *FA (MD)* values show the mean and standard deviation at the cluster maximum. '% dec (inc).' is the percentage decrease (increase) in the mean boxers' *FA (MD)* compared with the controls.

Table 4-3 Statistically significant clusters where boxers' values of *MD* are less than the controls.*

Cluster max							*MD* ($\times 10^{-3}$ mm^2 s^{-1})		
x	**y**	**z**	**Tissue**	**Region**	**Corr.p**	**t vox**	**Boxers**	**Controls**	**% dec.**
-48	12	-6	GM/CSF	Superior temp gyrus	0.000	7.66	1.06 ± 1.3	1.26 ± 0.17	18
26	16	-28	GM/CSF		0.000	5.69	1.06 ± 1.1	1.23 ± 0.12	14
2	-38	-16	GM/CSF		0.000	4.90	1.17 ± 1.1	1.37 ± 0.23	14
36	-8	64	GM/CSF	Mid Frontal gyrus	0.000	4.83	0.94 ± 1.7	1.22 ± 0.33	23
32	-44	58	GM/CSF	Inferior pariet. Lobule	0.000	4.73	0.95 ± 1.2	1.14 ± 0.28	17
-24	30	52	GM/CSF	Mid. Frontal Gyrus	0.000	4.47	0.94 ± 1.2	1.10 ± 0.17	15
-52	6	44	GM/CSF	Mid. Frontal Gyrus	0.000	4.38	0.99 ± 1.4	1.16 ± 0.17	15
32	-30	62	UNC	Precentral Gyrus	0.000	4.18	0.92 ± 1.3	1.12 ± 0.26	18
18	44	44	GM/CSF	Superior Front gyrus	0.000	4.17	1.01 ± 1.4	1.19 □ 0.24	16
54	6	38	GM/CSF	Inf. Frontal Gyrus	0.000	3.90	0.94 ± 1.4	1.11 ± 0.20	15
-42	-52	56	GM/CSF	Inf. Parietal Lobule	0.000		1.20 ± 2.1	1.41 ± 0.32	14
48	16	-10	GM/CSF	Sup. Temp. Gyrus	0.001	3.58	1.12 ± 1.3	1.25 ± 0.15	11
-46	-16	54	GM/CSF	Precentral Gyrus	0.002	3.94	0.93 ± 1.1	1.06 ± 0.14	12
52	-42	50	UNC	Inf. Parietal Lobule	0.002	3.89	1.02 ± 1.4	1.22 ± 0.25	16
50	-14	54	GM/CSF	Precentral Gyrus	0.002	3.86	0.89 ± 1.3	1.05 ± 0.17	15
-58	-32	44	GM/CSF	Postcentral Gyrus	0.008	3.90	0.94 ± 1.3	1.09 ± 0.17	13
40	-62	50	GM/CSF	Sup. Parietal Lobule	0.019	3.79	1.09 ± 1.7	1.27 ± 0.27	15
-22	8	-30	GM/CSF	Uncus	0.074	4.08	1.03 ± 1.1	1.16 ± 0.12	11

* Clusters are recorded in decreasing order of their statistical significance (corr. *p*). (x,y,z) are the Montreal Neurological Institute (MNI) coordinates (in mm) of the most significant voxel in each cluster. That voxel is then identified as being white matter (WM) or grey matter (GM). 'UNC' signifies a voxel that was unable to be classified.'corr *p*' is the corrected *p*-value for that cluster. 't vox' is the *t*-value for the given maximum voxel. *MD* values show the mean and standard deviation at the cluster maximum. '% dec.' is the percentage decrease in the mean boxers' *MD* compared with the controls.

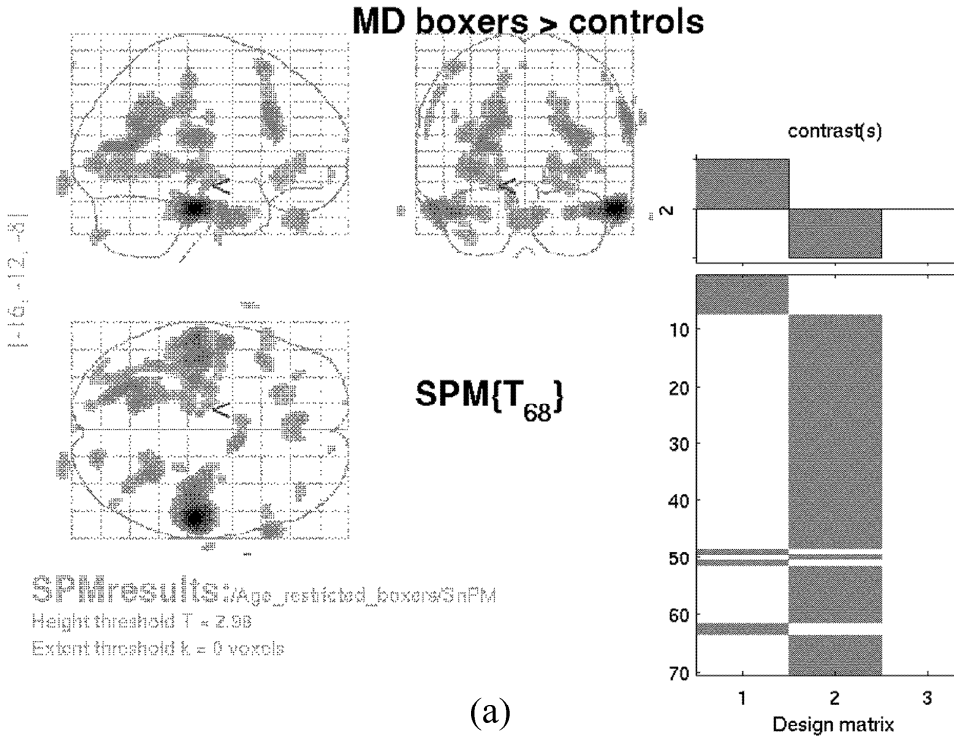

(a)

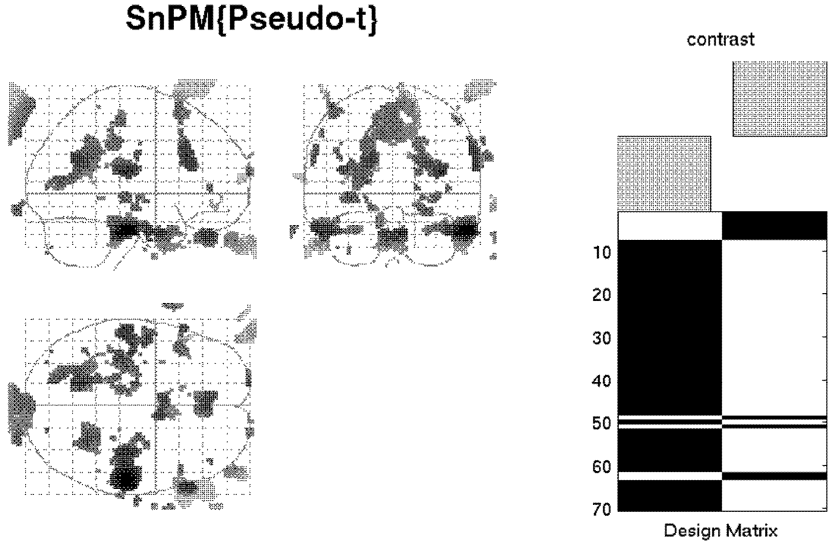

(b)

Figure 4.5 Comparison of parametric (a) and non-parametric (b) analyses of the same data. Shading represents voxels where the average boxers' *MD* is greater than the average controls' *MD*. Note: These are "glass-brain" views rather than in-plane views, where the data in the third dimension are superposed as that dimension is collapsed.

4.3.4 Non-parametric analysis

Figure 4.5 gives a qualitative comparison between the results using the same data and same analysis parameter selections with SPM2 and SnPM2. The regions identified by each as where the boxers' *MD* are statistically significantly greater than the controls are shown to be similar. Although no meaningful quantitative comparison can be made, these results give confidence that the data are amenable to parametric analysis.

4.4 ***Discussion***

4.4.1 Background

This voxel-based analysis of DTI data provides an important complement to previous attempts to localize cerebral injury caused by non-severe head trauma. These efforts have included conventional MRI and functional imaging (Bigler 2001; McAllister, et al. 1999) as well as psychometric assessment to link structural damage to functional damage (Mathias, et al. 2004).

This study differs from many diffusion studies in that these subjects were not scanned because of recent known trauma. Our results therefore relate to the cumulative non-acute effects of repeated blows to the head. Chronic TBI, which represents the cumulative, longterm neurological consequences of repetitive concussive and subconcussive blows to the brain has been studied primarily in relation to boxing, though it may also apply to other contact sports such as soccer, football, ice hockey, and martial arts (Rabadi and Jordan 2001). It has been hypothesized (Slemmer, et al. 2002) that repeated TBI may result in cumulative damage to cells of the brain, but the researchers lacked the means to test this *in vivo*. In vitro tests revealed that cells of the hippocampus may be susceptible to cumulative damage following repeated mild traumatic insults, which is consistent with the abnormalities detected in this study in the medial temporal lobe in the boxer group. Those researchers also postulated that cell damage from repeated mild shocks may be quite different from that activated by a single more severe shock.

The changes in *MD* and *FA* observed in this study indicate that the diffusion abnormalities in boxers are not spread uniformly throughout the brain, and that specific brain regions may be more sensitive to injury from boxing-related TBI. The

results are important in furthering our understanding of *MD* and *FA* as markers of TBI, and demonstrate the utility of DTI in providing evidence of specific structural abnormalities after nonsevere TBI.

Abnormalities in multiple brain regions found in this study were manifested as decreases in *FA,* and both increases and decreases in *MD*.

4.4.2 Changes in FA

Although there are fewer reported studies of *FA* than of *MD*, there is general agreement that TBI will cause a decrease in *FA* (Arfanakis, et al. 2002; Chan, et al. 2003; Huisman, et al. 2004). Our findings of significant decreases in *FA* in the boxers support these non-boxing-related studies. Importantly, the areas of decreased *FA* and increased *MD* were located in similar regions, with several overlaps, and were primarily located in the WM (Figure 4.3).

Table 4-1 lists the average values of *FA* for boxers and controls at the clusters that show a statistically significant decrease. This decrease ranged from 7% to 17%.

4.4.3 Changes in MD

Findings from previous studies of *MD* are less consistent than for *FA*. Some have reported increases in *MD* after TBI (Goetz, et al. 2004; Zhang, et al. 2003), while others have reported decreases (Liu, et al. 1999; Takayama, et al. 2000). Others studied acute closed head injuries within 48 hours of the trauma and discovered both increased and decreased diffusion in different parts of the brain (Huisman, et al. 2003). The results presented in this thesis suggest that both increases in *MD* and decreases in *MD* can result from repetitive blows to the head. Furthermore, it was found that the increases in *MD* were primarily in WM (median distance to the nearest boundary was 4 mm), while the decreases in *MD* were close to WM/GM boundaries (median distance to the nearest boundary was 1mm), and mainly in the GM. This separation of the changes in *MD* into WM and GM has not been reported before. However, there is also the possibility of partial volume effects making a significant contribution to this result. Partial volume effects occur when a given voxel comprises more than one type of tissue. For example, voxels on the boundaries of the ventricles may well include CSF, WM and GM. Such heterogeneous composition clearly affects the diffusion values in affected voxels in a

non-quantifiable way. Since the voxels reported above are near WM/GM boundaries, they are susceptible to partial volume effects, so the results must be interpreted with caution.

The decreases in *MD* in grey matter are consistent with the well documented presence of cortical damage in TBI (McAllister, et al. 1999). A previous conventional MRI study of nine patients suffering traumatic brain injury ranging from mild to severe, about a year after receiving head trauma, discovered that such patients had decreased grey matter concentration (Gale, et al. 2005). This may be linked to the finding of the present study of reduced *MD* in the cortical grey matter. Similar morphometric studies are needed to complement future DTI studies.

An increase in the whole-brain diffusion of boxers compared with controls has been observed (Zhang, et al. 2003). By using voxel-based analysis to localize the areas of increased diffusion, this study complements and extends that work. They reported an increase in the whole-brain *MD* of boxers compared to controls of nearly 4%. This compares with the results of the present study, shown in Table 4-2, where significant clusters had *MD* increases ranging from 9% to 17%. These findings are consistent with a heterogeneous distribution of damage, with some parts of the brain (mainly WM) being substantially more susceptible than others. Our finding of regions where boxers had smaller *MD*s than the controls (Table 4-3) has two important features. First, almost all of the clusters were identified as comprising both CSF and GM. Second, the *MD* values in all of these clusters were higher than those in the Table 4-2 clusters (which are predominantly WM), and were lower for the boxers than for controls. The values presented are higher than would be expected for brain tissue alone. This suggests that these clusters represented a mixture of CSF and tissue. Decreases in *MD* in the boxers compared to the controls may be related to differences in the partial volume averaging of GM and CSF.

Both the boxers and controls showed regions of positive correlation between their *MD*s and age (Figure 4.4). With different numbers of boxers and controls, it is hard to make a comparison between the relative strengths of the boxers and controls correlations. However, there seems to be a strong positive correlation in the cerebellum of the boxers with age, which is not apparent with the controls. This may suggest that boxers sustain chronic damage to their cerebellum, which increases with age. Based on this

interpretation, age may be seen as a proxy variable for length of time fighting, linking cerebellar damage with the number of shocks sustained. However, (Zhang, et al. 2003) found no correlation between whole-brain diffusion and total rounds of performance, or years of boxing. Also, given that our controls also showed a positive correlation, albeit a weaker and spatially different one between diffusion and age, further study is needed to determine whether the boxers are different in this regard.

A prospective MR study of sports-related concussion in eight college football players. found effects of mild TBI in several regions, including cerebellar (Jantzen, et al. 2004). Another study investigated 13 infants with severe TBI and found "unexpected cerebellar atrophy" (Soto-Ares, et al. 2001). A study of 11 healthy volunteers and 27 patients (26 –86 years old) found that diffusion increased with age in periventricular WM (Chun, et al. 2000). It is possible that other regions have age-dependent diffusion characteristics. Further investigation is needed to determine why the stronger correlation reported in this paper between age and *MD* in the boxers did not manifest itself in statistically significant group differences in *MD* between the boxers and the controls in the cerebellar region.

4.4.4 Conclusion

This study has shown that DTI's ability to identify microstructural abnormalities makes it an important diagnostic tool. As far as the author is aware, this is the first study to use VBA to objectively analyze microstructural changes throughout the entire brain caused by cumulative, chronic blows to the head. This is an important step in providing *in vivo* evidence of the effects of chronic head injury, and evaluating the competing theories about concussion. The results of this study show that these effects on the diffusion in the brain may differ between WM, GM, and CSF. These results add another dimension to understanding the adverse impact on the brain that multiple concussions can have. While they are not incompatible with current theories on the biomechanics and adverse physical impact of head trauma (Shaw 2002), observations of the location and extent of cerebral abnormalities within the brain provide important new information about the adverse physical impact of non-severe head trauma in contact sports such as boxing.

This study provides important evidence that repeated mild closed head injury, even in the absence of major trauma, causes specific structural abnormalities in the brain, with increased *MD* and/or decreased *FA* in the internal capsule, putamen, medial temporal lobe, inferior frontooccipital and inferior longitudinal fasciculus, cerebral peduncle, and corticobulbar and corticospinal tracts. Decreased *MD* was also observed in the cortical grey matter. These observations indicate that the diffusion abnormalities in these boxers were not spread uniformly throughout the brain and that there were specific brain regions that may be more sensitive to injury from boxing-related TBI. The lateral symmetry of the observed abnormalities is to be expected if the boxer group, on average, received as many blows to one side of the head as the other.

These results are important in furthering the understanding of *MD* and *FA* as markers of TBI and demonstrate the utility of DTI in providing evidence of specific structural abnormalities after non-severe TBI.

5 Multivariate Diffusion Tensor Analysis

5.1 Background

Conventional univariate analysis necessarily ignores much of the diffusion information contained in the tensor and the metrics derived from it. With three quasi-independent groupings of diffusion metrics (ADC, anisotropy and propagation – see chapter 2) and several different metrics in each grouping, much information is lost if metrics are analysed separately. As this study will show, even though a particular metric may not be strong enough to produce statistically significant univariate results, when combined with other metrics in multivariate analysis, it can make an important contribution. Also, since the three metric groupings represent different physical properties of the diffusion, it is important to include as much of that information in the analysis as possible. This will be best achieved by selecting a diffusion metric from each grouping.

Not all metrics within a single grouping are equivalent (Kingsley 2006b), and it is known that some metrics are more susceptible to displaying bias under noise than others in processing tensor data (Anderson 2001; Armitage and Bastin 2000; Basser and Pajevic 2000; Bastin, et al. 1998). Therefore a simulation program was written to examine the different metrics' bias under different imaging conditions.

In this chapter, the results of the simulations are presented, and then three different multivariate methods for voxel based analyses of DTI data are developed. The purpose of this multivariate approach is to enable a more robust statistical comparison between the patient and control groups than is possible when testing the metrics separately.

One multivariate approach used was to evaluate the Hotelling's T^2 statistic at each voxel to test the null hypothesis that the boxer means were the same as the control means for all three metrics. A difference in one or more of the means could be enough to reject the null hypothesis and to identify that voxel as having a structural difference. This is similar conceptually to univariate testing, except now the Student's *t*-statistic has been replaced by the Hotelling's T^2 statistic.

The other two approaches used linear discriminant analysis (LDA). The first used LDA to form a new "linear combination" metric at each voxel, which was subjected to

standard two-sample *t*-tests. The second approach used LDA to classify each subject as either patient or control, with that classification then checked against the actual status of the subject, with LDA's "predictive value" being recorded at each voxel.

These uses of the Hotelling's T^2 statistic and the linear discriminant function from LDA in voxel based analyses of DTI data are both novel.

These analyses were applied to the age-restricted boxer dataset comprising 59 boxers and 12 controls. Because the Hotelling's T^2 values were calculated using in-house software then mapped as an image, the multiple comparison corrections in SPM were not available for the Hotelling's data. In order to standardise the analyses, FDR corrections were not done on the data in SPM (univariate and LDA's linear combination). Instead, a *p*-value threshold of 0.001 was used for voxel significance. This is represented by an *F*- or T^2 - value of 11.81 ($t = 3.44$).

5.2 Simulations

To test the various metrics for lack of bias with noise, the approach of (Kingsley 2006b) was followed. A tensor was selected as the "ground truth", which was then subjected to Gaussian noise based on a selected signal-to-noise ratio (SNR). Next, the "noisy" data were processed as though they were the received signals. The resulting metrics were then compared with their "ground truth" equivalents to check for any inherent bias in the system.

The process used for these simulations was:

1. Select typical eigenvalues λ_1, λ_2 and λ_3 to form the "ground truth" tensor

$$\mathbf{D} = \begin{pmatrix} \lambda_1 & 0 & 0 \\ 0 & \lambda_2 & 0 \\ 0 & 0 & \lambda_3 \end{pmatrix}.$$

2. Select *b*-factors for each gradient direction, and the gradient sampling scheme. Usually the *b*-factors are the same for each gradient direction, and around 1 000 s/mm^2. However this is often one of the parameters that is being investigated in the simulation, so sometimes values up to 3 000 s/mm^2 or higher are used for comparison. The gradient sampling scheme comprises the directional cosines g_x,

g_y, and g_z, with $g_x^2 + g_y^2 + g_z^2 = 1$. These g vectors, together with their *b*- factors, enable the 6 elements of the **b** matrix to be found. This is the 3 × 3 symmetric matrix that replaces the scalar *b* value of single direction imaging.

a. The normalized gradient direction vector is given by

$$\mathbf{G_n} = (g_x, g_y, g_z)^T, \text{ with } g_x^2 + g_y^2 + g_z^2 = 1.$$

b. Ignoring imaging gradients, the relative magnitudes of the b_{ij} terms can be found from

$$\mathbf{g} = \mathbf{G_n}\,\mathbf{G_n^T} = \begin{bmatrix} g_x^2 & g_x g_y & g_x g_z \\ g_x g_y & g_y^2 & g_y g_z \\ g_z g_x & g_z g_y & g_z^2 \end{bmatrix}, \text{ then } \mathbf{b} = b\,\mathbf{g}.$$

The *b* factor thus acts as a proportionality term.

Although it is common to ignore imaging and intrinsic gradients, they can be included in the **b** matrix here if desired.

3. Select the SNR of the $b = 0$ signal. Typically values of 15:1 – 30:1 apply for a single DTI acquisition. This can be improved by signal averaging. Signals with $b > 0$ have lower SNR, because of the decay described by (Eq. 3.3) $S = S_0 \exp[(-\text{Trace}(\mathbf{bD})]$. With low SNR and high *b*- factor, SNR in individual diffusion weighted images can easily drop to 3:1 or worse. Then Rician statistics and associated biases must be considered.

   For comparison purposes, it can be instructive to do simulations at high SNR (~ 30-50:1) to show the intrinsic properties and trends of the system, then at lower SNR to show the systematic deviations that might occur in a realistic situation.

4. Calculate $\mathbf{bD} = b\mathbf{gD}$ (from steps 1 and 2) for each gradient direction (where the tensor contraction is defined as $\mathbf{U}:\mathbf{V} = tr(\mathbf{U}\mathbf{V}^T)$).

5. Calculate the theoretical *S* for $b = 0$ and for each gradient direction (i.e. for each **bD**) using the signal equation given in step 3.

   To each *S* add Gaussian noise with a mean of 0 and standard deviation σ, where $\sigma = S_0/\text{SNR}$. (This is added to each orthogonal channel, real and imaginary, of

the 2 quadrature receivers, though the signal can be all in one channel.) This results in noisy signal intensities *M*.

6. Calculate the "observed" *bD* and *D* for each gradient direction:
   Since, for any two gradient directions, $S_1 = S_0 e^{-b_1 D}$ and $S_2 = S_0 e^{-b_2 D}$,

   then $D = \ln(\frac{S_1}{S_2}) / (b_2 - b_1)$.

   This can be written as

   $bD = -\ln(M/M(b=0)) = -\ln[M(b=0)] - \ln M$

   where *M* is the noisy signal

   D is the effective apparent diffusion coefficient (ADC) in this direction.

7. It is now possible to calculate the six "observed" tensor elements from *D* measured in at least six noncollinear directions. If exactly six directions are used, the calculation can be done analytically. If, as is usually the case in practice, more than 6 directions are used, then a fitting procedure is required to form the tensor.

8. From the observed tensor, many derived parameters can now be calculated. These are then compared with those from the "ground truth" tensor to see how much discrepancy has been introduced by the noise.

9. Repeat steps 6-9 at each voxel (at least 1000 times, though preferably 10 000 – 50 000 or more). More runs are needed with low SNR.

10. Analyse the results.

11. Change one or more parameter(s) and repeat the whole process.

For this study, the tensor eigenvalues were 9×10^{-4}, 7×10^{-4}, and 5×10^{-4} mm^2/s respectively, 26 gradient directions were specified, and b=1000 s/mm^2. For comparison purposes, the resulting simulation distributions were normalised to have a mean of 0 and standard deviation of 1.

5.2.1 Simulation Results

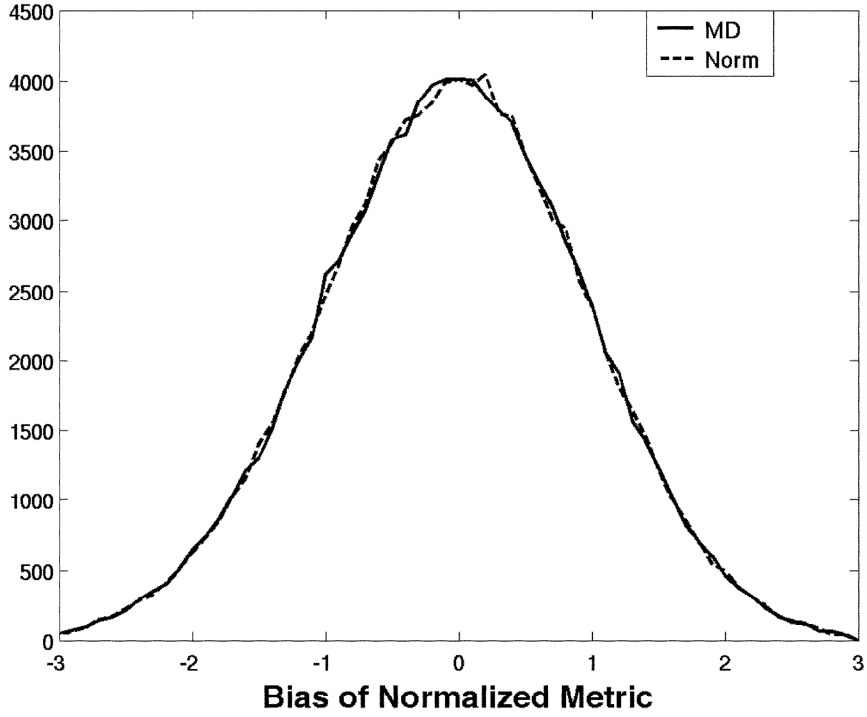

(a)

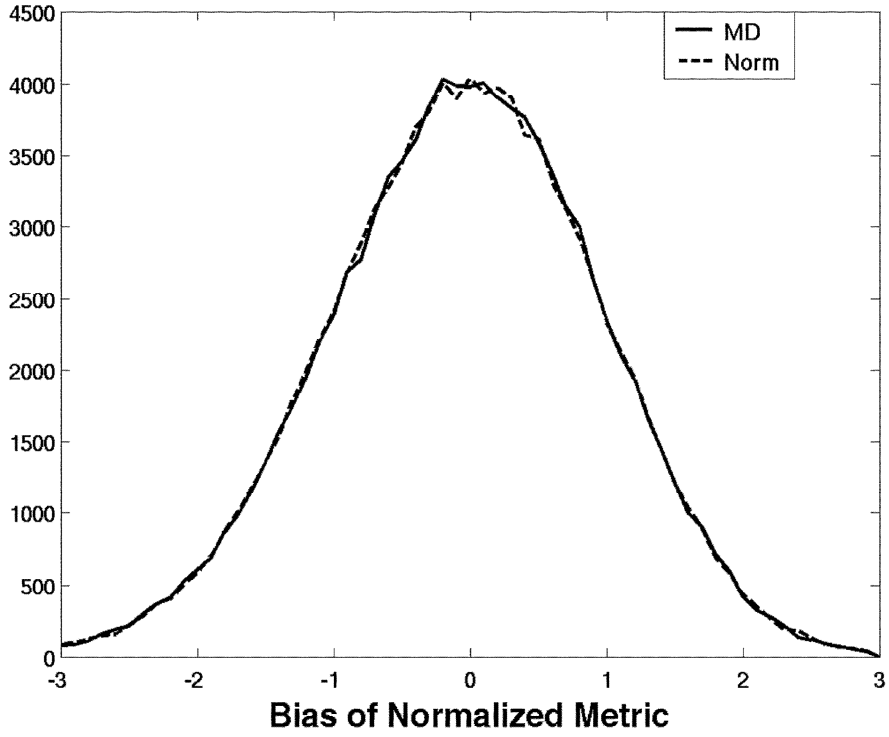

(b)

Figure 5.1 Distribution of ADC bias from 100 000 simulations, with b = 1 000 s/mm2, no. gradients = 26, eigenvalues 9×10^{-4}, 7×10^{-4}, and 5×10^{-4} mm2/s and SNR (for b = 0) of (a) 30, and (b) 15.

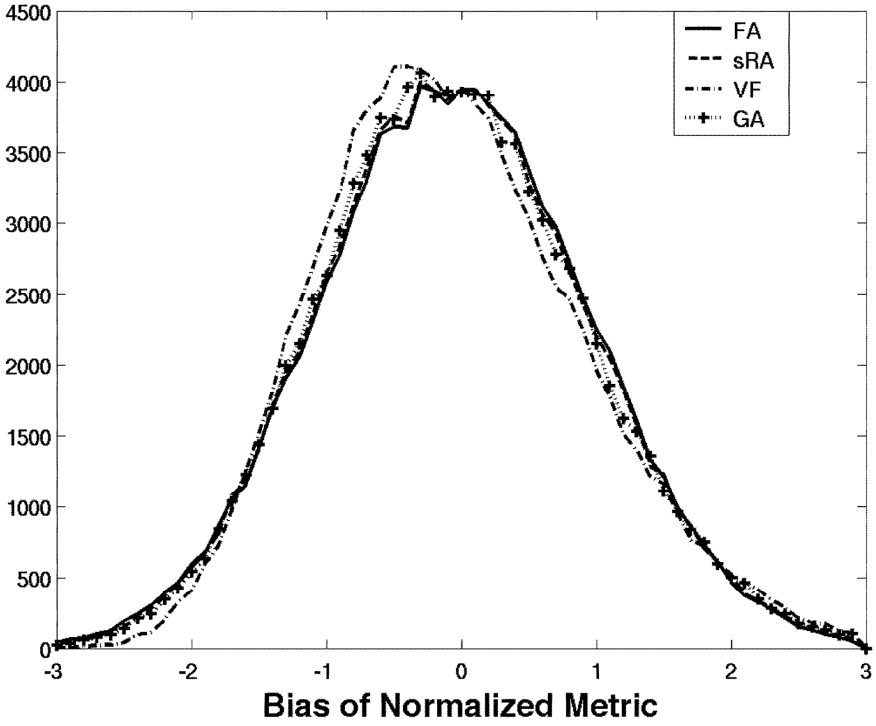

(a)

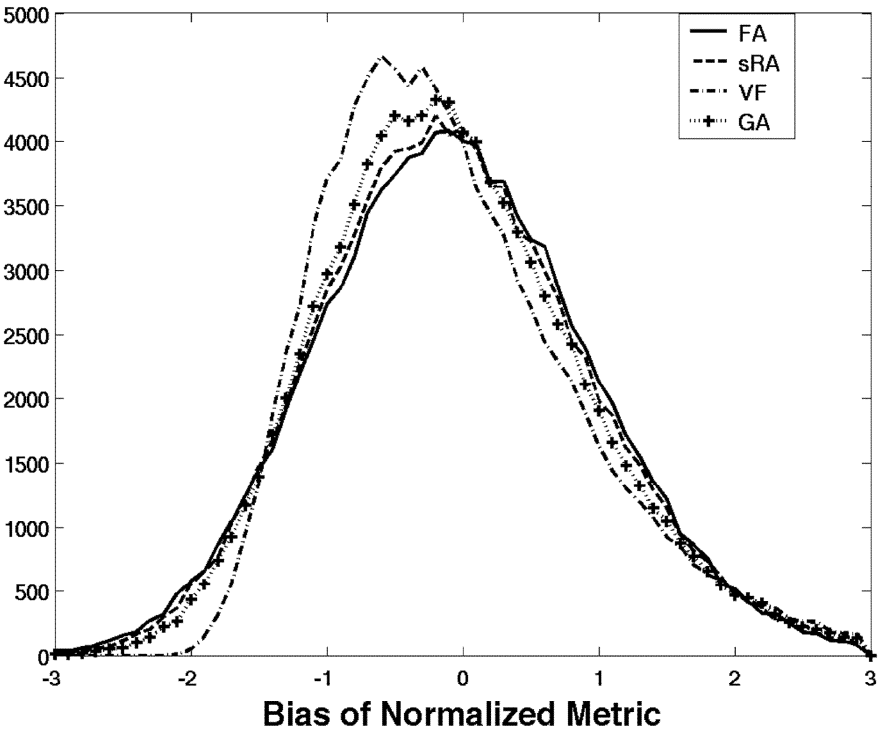

(b)

Figure 5.2 Distribution of anisotropy bias from 100 000 simulations, with b = 1 000 s/mm^2, no. gradients = 26, eigenvalues 9×10^{-4}, 7×10^{-4}, and 5×10^{-4} mm^2/s and SNR (for b = 0) of (a) 30, and (b) 15.

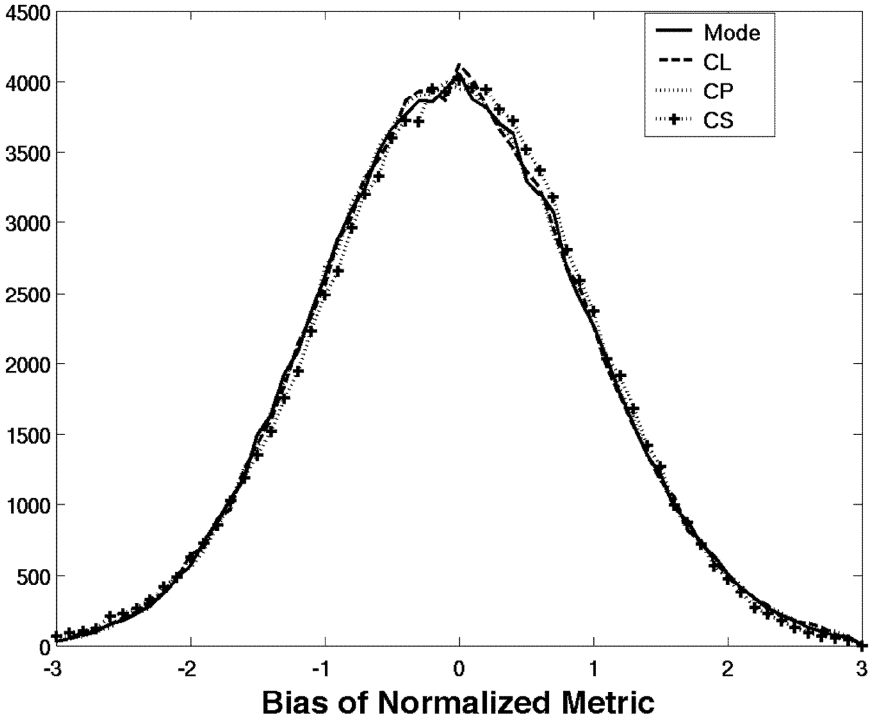

(a)

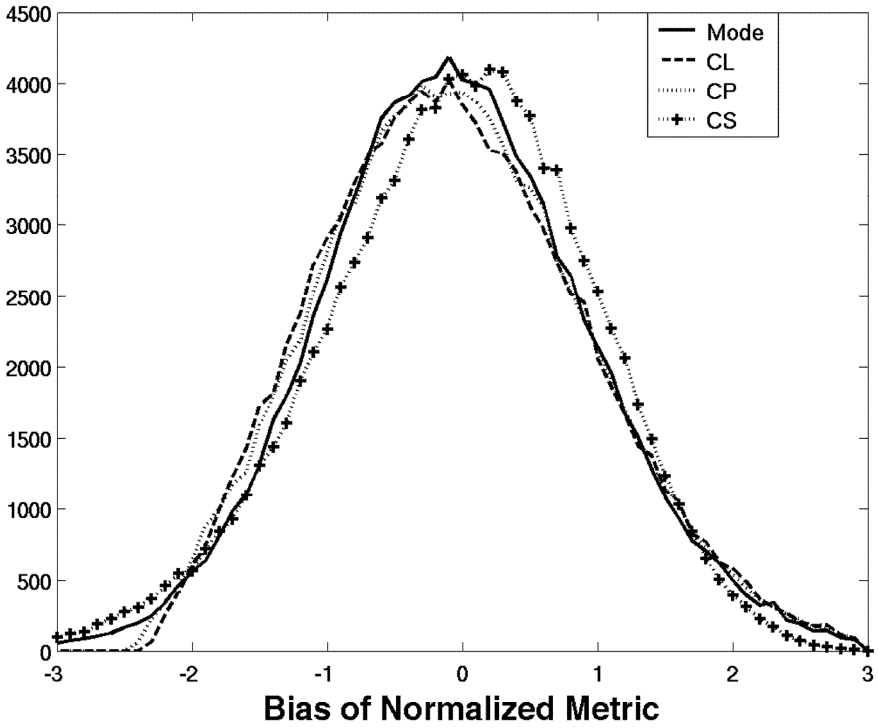

(b)

Figure 5.3 Distribution of propagation bias from 100 000 simulations, with b = 1 000 s/mm^2, no. gradients = 26, eigenvalues 9×10^{-4}, 7×10^{-4}, and 5×10^{-4} mm^2/s and SNR (for b = 0) of (a) 30, and (b) 15.

Figure 5.1 shows that both *MD* and norm are unbiased even at low SNR. Of the anisotropy metrics, Figure 5.2 shows that both *VF* and *GA* exhibit slight negative bias, which becomes more pronounced at low SNR. From a bias perspective, either *FA* or *sRA* are therefore the preferred anisotropy metrics. In Figure 5.3 at low SNR, the propagation metrics are reasonably unbiased, although *CS* shows a slight positive bias. All are unbiased at the higher SNR. If orthogonal metrics are required (see (Ennis and Kindlmann 2006)), *norm*, *FA* and *mode* are suitable. However, the more commonly used pair of *MD* and *FA* is also suitable (augmented with *mode* in this study for fuller analysis).

5.3 Conjunction/Disjunction Analysis

Conjunction and disjunction are two different ways of simultaneously analyzing multiple metrics. For a voxel to be identified as significant under conjunction, *all* the metrics separately must return a positive result at that voxel. In contrast, under disjunction it is enough for *any* of the metrics to be positive for a voxel to be identified as significant.

Instead of using *MD* as the ADC metric, *norm* is also valid (Kingsley 2006b). Since *norm*, *FA* and *mode* are orthogonal (Ennis and Kindlmann 2006), the probabilities of their interactions are greatly simplified. From basic probability theory of the union and intersection of independent variables (Moore and McCabe 2006), it is straightforward to find the probabilities of false positives (FP) and false negatives (FN) under both conjunction and disjunction situations. (Since *mode* was far less sensitive than *norm* and *FA*, it was not included in these exploratory conjunction/ disjunction analyses.)

The relevant contrasts used were:

- Conjunction: Boxers' norm > controls' AND boxers' FA < controls';
- Disjunction: Boxers' norm > controls' OR boxers' FA < controls'.

Then, if at a given voxel the probability of a FP with *norm* is α_{norm} and of a FN is β_{norm}, and similarly for *FA*, then the combined probabilities are given by:

Conjunction:

$$P(FP) = \alpha_{norm}. \alpha_{FA} \quad 5.1$$

$$P(FN) = \beta_{norm}+\beta_{FA}-\beta_{norm}. \beta_{FA} \quad 5.2$$

Disjunction:

$$P(FP) = \alpha_{norm} +\alpha_{FA} - \alpha_{norm}. \alpha_{FA} \quad 5.3$$

$$P(FN) = \beta_{norm}. \beta_{FA} \quad 5.4$$

In order to achieve a final result with a *p*-value of 0.001 for comparison with univariate analyses, Equations 5.1 – 5.4 were used to find appropriate *p*-values for the individual metrics that were input into the conjunction/disjunction analysis. For convenience, the two input *p*-values were taken to be the same, but this need not be the case. Indeed, with unbalanced input metrics such as *norm* and *FA*, a more sophisticated analysis would optimise the *p*-values to give maximum sensitivity in the result. This would entail reducing the *p*-value for *norm* and increasing it for *FA*, since *norm* is the stronger metric. This could maximize the disjunction result, but conjunction, by its very nature, will always only be as strong as the weakest component. With these data, conjunction is not going to offer more than *norm*, regardless of the *p*-values.

In principle, Equations 5.1 – 5.2 suggest that conjunction is good for reducing the rate of false positives relative to the input data, but at the cost of increasing the rate of false negatives (i.e. loss of power or sensitivity); and vice versa for disjunction. Thus disjunction increases the power of the analysis relative to the inputs, but the results will include more false positives.

As expected, Figure 5.4 shows that with these data, conjunction reduces the power of the analysis not just relative to the input data, but also compared to the best univariate result (*norm*). Figure 5.5 does not show the expected increased sensitivity of disjunction. This could well be a result of using non-optimized input *p*-values.

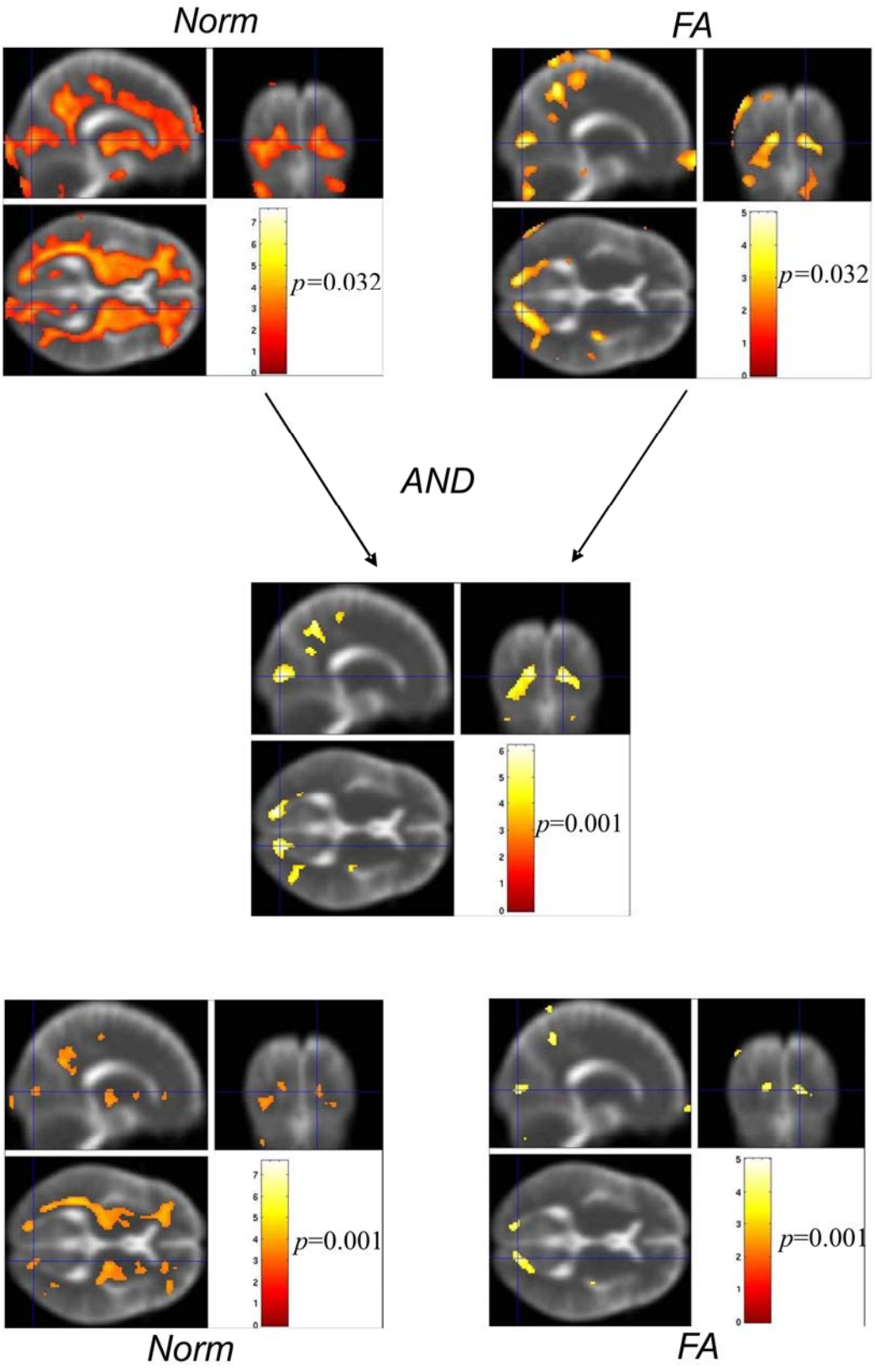

Figure 5.4 Top 3 images: Using conjunction analysis with appropriate initial p-values to give a final p-value of 0.001. Bottom 2 images: Single metric results for comparison.

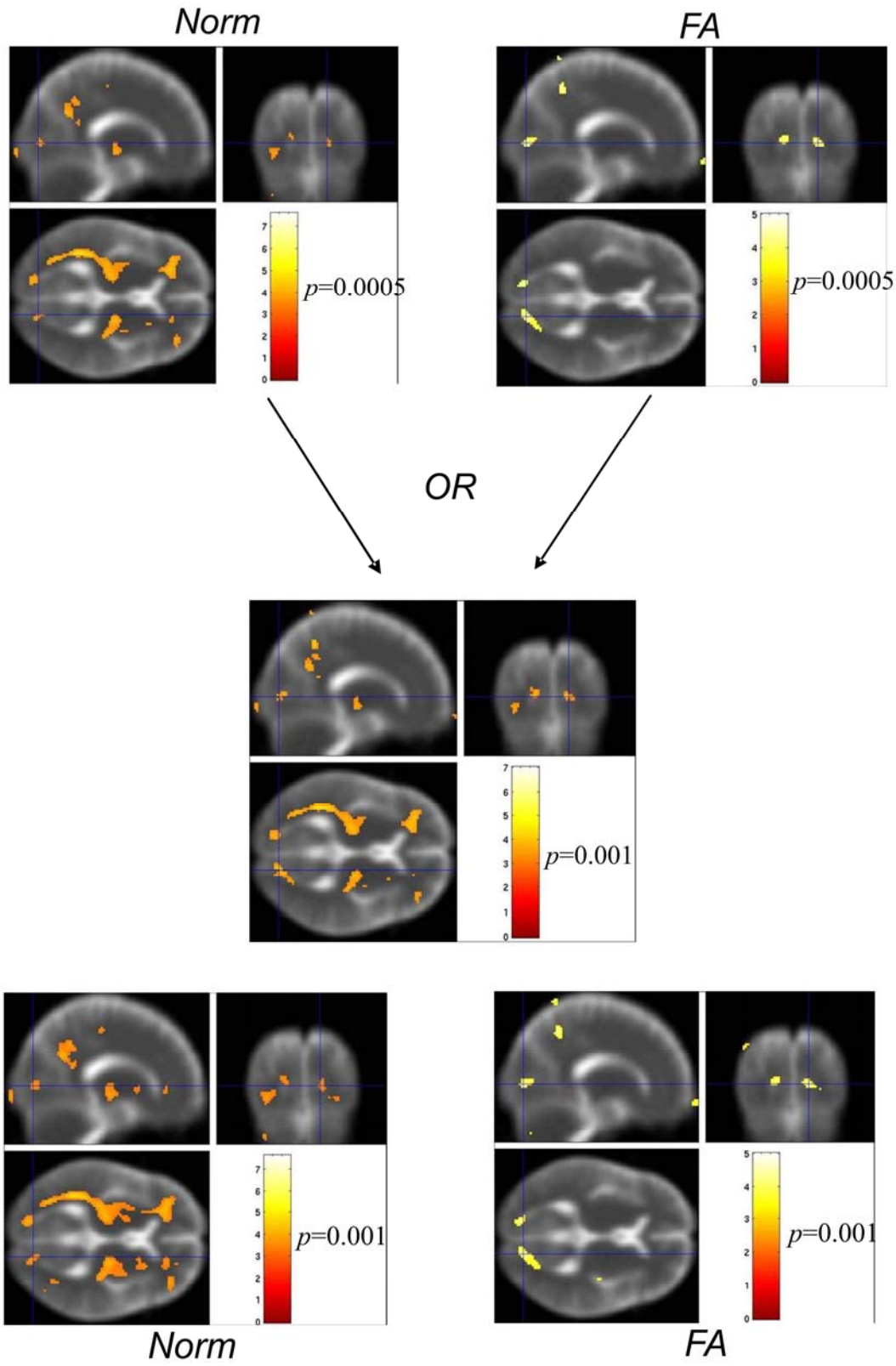

Figure 5.5 Top 3 images: Using disjunction analysis with appropriate initial p-values to give a final p-value of 0.001. Bottom 2 images: Single metric results for comparison.

5.4 Two-Sample Hotelling's T-Squared Test

Hotelling's T^2 statistic (Siotani 1956) was used to perform multivariate hypothesis tests of the data using firstly *MD* and *FA*; and then *MD, FA* and *mode*. The purpose was to see whether a difference could be detected between the boxer and control groups using multivariate data. The assumptions for this analysis are that the data from both populations are normally distributed and have a common variance, and that subjects from both populations have been independently sampled.

In the following summary of Hotelling's T^2 statistic, it should be noted that though the equations are applied to each voxel, the (*x,y,z*) coordinate subscripts have been omitted for clarity.

Suppose population 1 has n_1 subjects and data $\mathbf{X_{11}}, \mathbf{X_{12}}, \ldots, \mathbf{X_{1n_1}}$

and population 2 has n_2 subjects and data $\mathbf{X_{21}}, \mathbf{X_{22}}, \ldots, \mathbf{X_{2n_2}}$

where $\mathbf{X_{ij}} = \begin{pmatrix} X_{ij1} \\ X_{ij2} \\ . \\ X_{ijp} \end{pmatrix}$

and X_{ijk} is the observation for metric k of subject j from population i, and p is the number of metrics being used. For example, if the boxers are labelled group 1, then the fourth boxer would have data vector $\mathbf{X}_{14} = \begin{pmatrix} MD_{14} \\ FA_{14} \\ Mode_{14} \end{pmatrix}$.

The aim is to test the null hypothesis that the sample means of every metric are the same for each group. The null hypothesis is rejected if either the *MD* or the *FA* or the *mode* means are different.

The sample mean vectors are defined as $\bar{\mathbf{x}}_\mathbf{i} = \frac{1}{n_i}\sum_{j=1}^{n_i} \mathbf{X_{ij}}$

Then the sample variance-covariance matrices are:

$$\mathbf{S_i} = \frac{1}{n_i - 1}\sum_{j=1}^{n_i}(\mathbf{X_{ij}} - \overline{\mathbf{x}_\mathbf{i}})(\mathbf{X_{ij}} - \overline{\mathbf{x}_\mathbf{i}})^T$$

Since the variances are assumed to be the same, the common variance-covariance matrix can be estimated by the pooled variance-covariance matrix:

$$\mathbf{S_p} = \frac{(n_1 - 1)\mathbf{S_1} + (n_2 - 1)\mathbf{S_2}}{n_1 + n_2 - 2}$$

Then the two-sample Hotelling's T^2 statistic is given by:

$$T^2 = (\bar{\mathbf{x}}_\mathbf{1} - \bar{\mathbf{x}}_\mathbf{2})^T \left\{ \mathbf{S_p}\left(\frac{1}{n_1} + \frac{1}{n_2} \right) \right\}^{-1} (\bar{\mathbf{x}}_\mathbf{1} - \bar{\mathbf{x}}_\mathbf{2})$$

and the F-statistic $F = \frac{n_1 + n_2 - p - 1}{p(n_1 + n_2 - 2)} T^2$ is approximately represented by the $F_{p, n_1 + n_2 - p - 1}$ distribution and threshold values.

The null hypothesis is then rejected at α level of confidence if $F > F_{p, n_1 + n_2 - p - 1, \alpha}$ This F-statistic map can then be used to identify voxels that are significantly different between the two groups.

Results of Hotelling's Analyses

The individual metric images in Figure 5.6(a-c) show qualitatively that there is one strong metric (*MD*) and two weak ones (*FA* and *mode*). This explains the loss of power (sensitivity) in the multivariate analysis when the weakest metric is included (Figure 5.6e). Nevertheless, both analyses, and in particular the bivariate one (Figure 5.6d), retain most of the main structure of the strongest single metric result (Figure 5.6a). It is primarily the smaller, more scattered clusters that have been undetected.

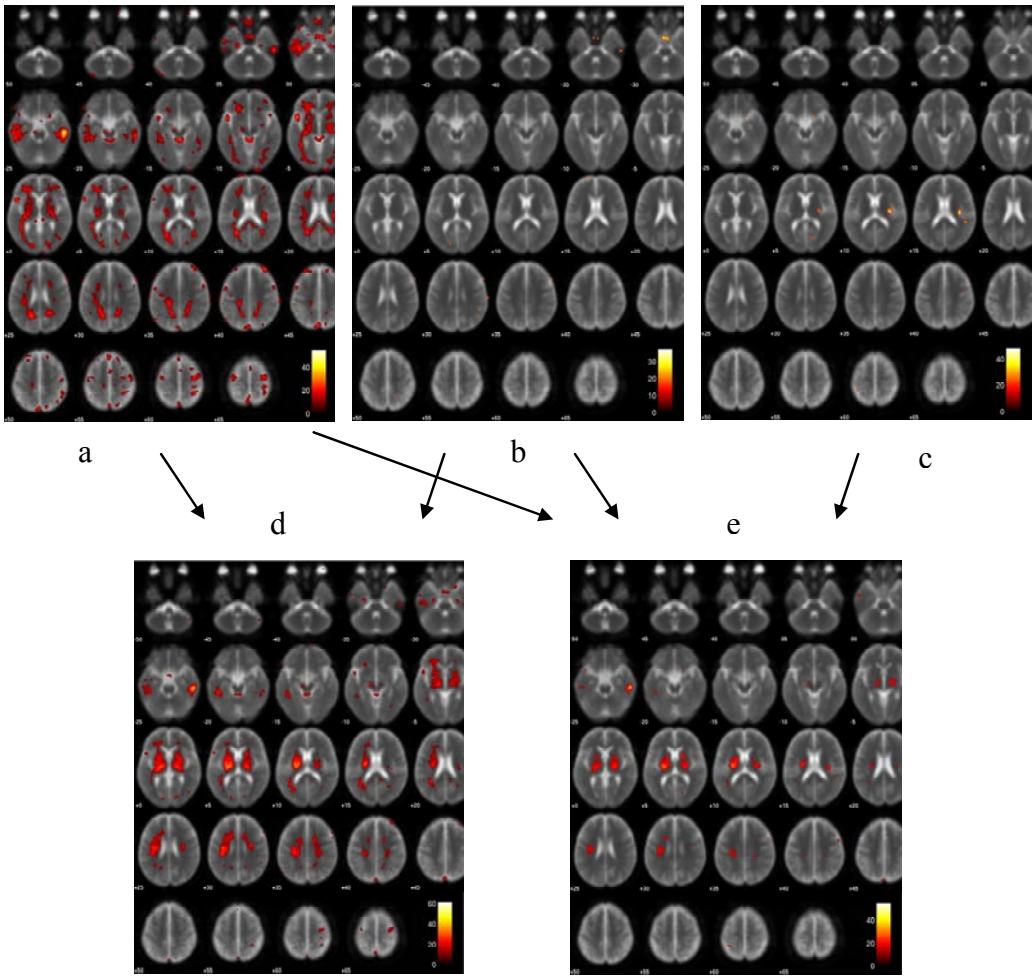

Figure 5.6 Comparison of single metric (a-c) and multi-metric (d, e) Hotelling's analyses of the same data, with significant voxels using T2-tests with p = 0.001 coloured. Top row: (a) MD, (b) FA and (c) mode separately; bottom row: (d) MD and FA combined, and (e).

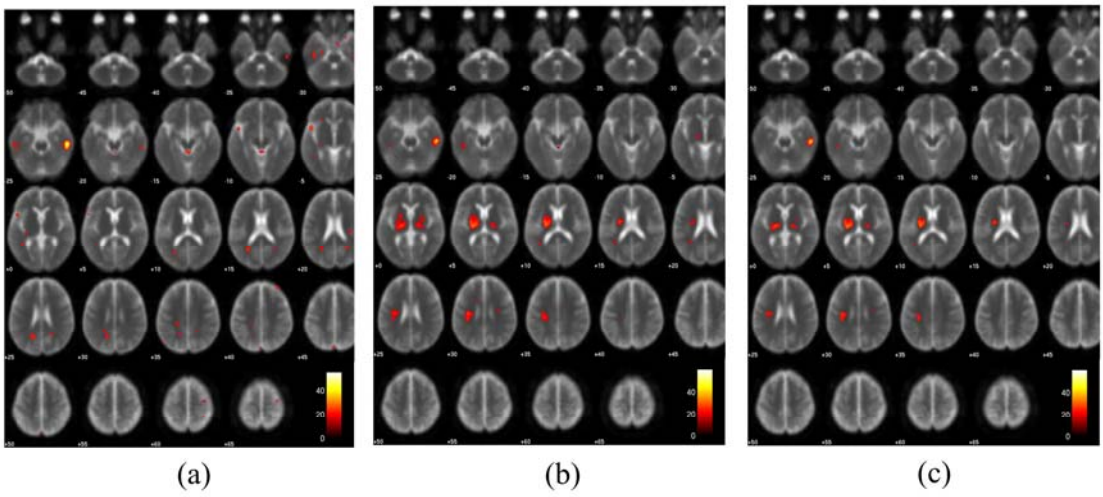

Figure 5.7 Testing the specificity of the different analyses at different false positives rates. Coloured regions show differences between boxers and controls using t-tests of: (a) MD with FDR < 0.01; (b) MD and FA combined, with FDR < 0.01, and (c) MD and FA combined, with FDR < 0.005.

5.5 Discriminant Analysis

LDA's purpose is to classify objects (in this study, human subjects) as belonging to one of two groups (in this study, patient or control) based on a set of characteristics (or "predictors") that describe the objects (in this study, diffusion metrics). This is a two-stage process. In the first stage, LDA is said to be operating in "training mode", while in the second, it is in "testing mode". Training mode is based on a set of observations for which both the predictors and the group membership of each object are known. LDA uses an iterative approach to find the discriminant function that best separates, or discriminates, the groups based on the input predictors. This is done by finding the discriminant function that maximizes the ratio of between group variance to within group variance, so that maximum group separability is obtained. Once testing is complete, and the linear discriminant function found, LDA can be used in testing mode. Here, the discriminant function is used to predict the group a new observation comes from, where that group is unknown.

To achieve its purpose, LDA must find a classification *rule* or model that best separates the groups. Critical in achieving this is finding which *set of features* best determines group classification of the objects.

The underlying assumptions of LDA (Fung 1995) are that:

- the observations come from a random sample
- each group is normally distributed, although LDA is relatively robust to non-normality caused by skewness (but not robust to outliers)
- each group has the same variance/covariance matrix.

LDA is similar to multiple regression, the difference being that LDA can be used only for classification - i.e. it is restricted to categorical target variables. In general, it writes the data as a linear discriminant function of the form

$$y = a_0 + a_1 x_1 + a_2 x_2 + \ldots + a_n x_n \qquad 5.5$$

where a_i are the linear discriminant coefficients to be determined, and x_i are the input metrics or predictors. The a_i are determined in such a way as to obtain maximum discrimination between the two groups of interest. Then, the expression can be used to

classify an unknown subject. Using the subject's x_i, if $y \geq 0$ the subject is assigned to one group; if $y < 0$ they are assigned to the other.

The Fisher's Linear Discriminant function in the *Matlab* Statistical Pattern Recognition toolbox[1] was used to perform the LDA in this study (Vojtech and Vaclav 2004).

It has previously been shown that, using *FA* and *MD*, LDA can provide a much more successful discrimination between the subtypes of multiple sclerosis compared with the metrics used individually (Lin, et al. 2006). LDA has also been used with MR imaging and MR spectroscopy data to identify brain tumours (Galanaud, et al. 2006). The latter study "shows the clinical value of a multivariate statistical analysis based on multimodal MRI and MR". The methods presented here have taken this approach a step further by applying LDA at each voxel.

5.5.1 LDA's "Linear Combination" Metric

This method of multivariate analysis uses only the training mode of LDA. Having found the coefficients of Eq. 5-5 from the training dataset, the value of the discriminant function at each voxel for each subject was recorded. This in effect became a new variable, which was then subjected to inter-group statistical testing. Since LDA maximises the difference between boxers and controls at each voxel, it could be expected that this new variable would be more sensitive to inter-group changes than any of the three metrics from which it was derived.

5.5.2 LDA's "Predictive value" Mapping

The predictive ability of LDA can be investigated by using LDA in testing mode. Here, having already obtained the discriminant function (Eq. 5-5), this is then evaluated at each voxel for any single subject, and if y is less than zero the subject is classified as a control; if it is greater than or equal to zero, the subject is classified as a boxer. Since in this study the classification of each subject was already known, the LDA classification could be compared with the actual one. The proportion successfully classified at a particular voxel is the predictive ability of LDA at that voxel.

[1] http://cmp.felk.cvut.cz/~xfrancv/stprtool/

Ideally in LDA, a different training dataset from testing dataset will be used. However, that is not always practicable, in which case the training can be done by leaving out the individual object about to be tested, to avoid bias. This is called "leave-one-out" (LOO) training. In a departure from this practice with the boxer study, the full dataset was used for training. This was done because testing 70 subjects at each of 10^5 voxels with LOO would be computationally time-consuming. The process was greatly simplified, and the computing time kept manageable, by using the same dataset for training as for testing. While this might have risked the introduction of bias to the analysis, as long as the training dataset is reasonably large, as in this case, then the effect of leaving one out would be small. To test this, the "strongest" voxel (i.e. the one showing most difference between boxers and controls) had leave-one-out LDA performed on it. The difference between the coefficients of Eq. 5-5 of the LOO training and full dataset training was less than 1%. Since it could be expected that the voxel showing maximum discrimination would show the most bias if there was any, this can be regarded as the maximum error from not using LOO. Given the saving on complexity and computing time, this was regarded as acceptable.

5.6 Results

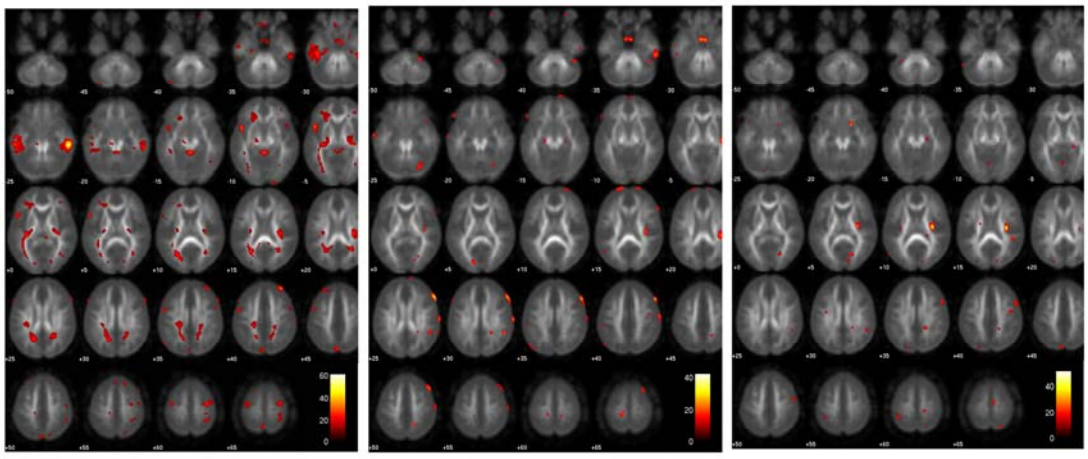

Figure 5.8 Univariate 2-tailed analyses comparing boxer data with controls, with p = 0.001, using (a) MD, (b) FA, (c) mode.

Before utilising multi-metric analyses, it is important to understand the behaviour of the metrics individually. Figure 5.8 displays standard two-sample two-tailed *t*-test results

for each metric, and shows there is one strong metric (*MD*) and two weak ones (*FA* and *mode*) in identifying differences between the professional boxer brains and the control brains (as did Figure 5.6). LDA can give quantitative results to verify this. Results are presented in this section showing the relative quantitative strengths of the different metrics at a particular voxel.

The individual brains were then segmented into WM and GM to explore the quantitative data further. In order to directly compare the relative strengths of the different metrics it is necessary to normalize their values to fit a standard normal distribution with a mean of 0 and standard deviation of 1. These data are then used in the LDA, and the coefficients of the normalized data can be directly compared. The distributions of coefficients are shown in Figure 5.9 for WM (a) and GM (b). Figure 5.9b shows the *FA* and *Mode* coefficients centred on zero with reasonably small variance, indicating less change in these metrics in GM than in WM (Figure 5.9a).

However, the coefficients of normalized MD in GM (Figure 5.9b) are also centred close to zero, with only a slightly larger spread. This suggests there may be little change in any of the metrics in GM. To test this hypothesis, the statistical map produced by the analysis of the linear combination metric was segmented in WM and GM parts. These were then superposed on an anatomical *FA* image, and the results are shown in Figure 5.10. This shows clearly that most of the differences in brain structure between boxers and controls have occurred in WM.

To explore the behaviour of the different metrics in WM and GM further, the distributions of the most frequent value (the statistical mode) for each boxer and each control were formed for each metric. The resulting histograms, with 500 bins, are shown in Figure 5.11. The changes in the boxers' statistical mode of the metric compared with the controls were: *MD* in WM, 6.8%; *MD* in GM, 2.9%; *FA* in WM, -3.5%; *mode* in WM, 0.0%. From these it appears that although *FA* is a weak indicator of brain damage at the voxel level, when averaged over the whole brain it may be more sensitive.

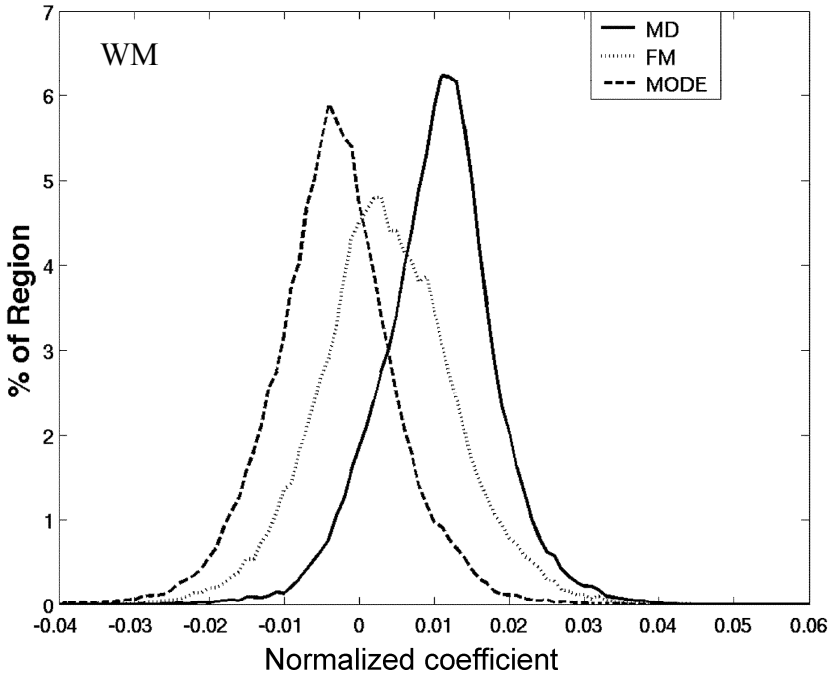

(a)

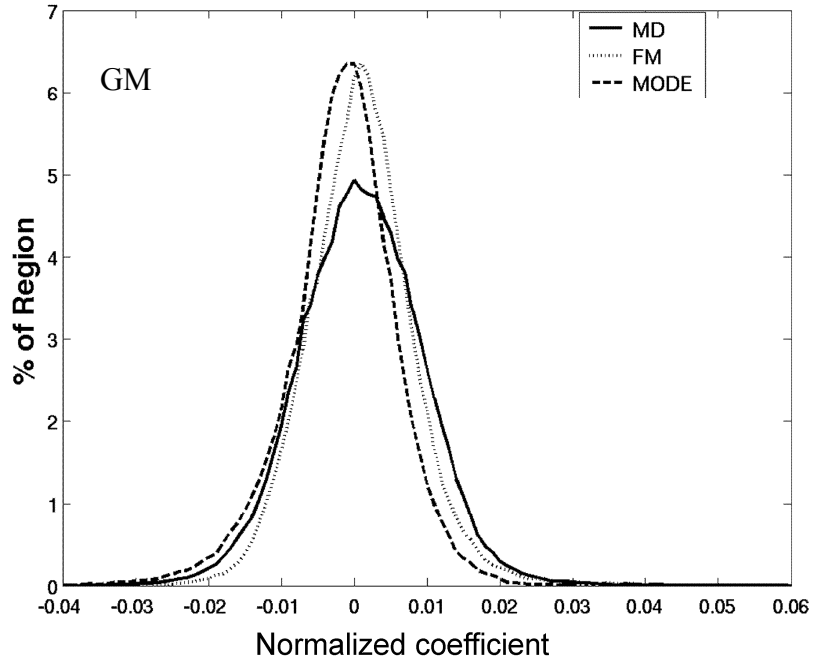

(b)

Figure 5.9 Histograms of the percentage of (a) white matter, and (b) grey matter taken by the different values of the normalized LDA coefficients.

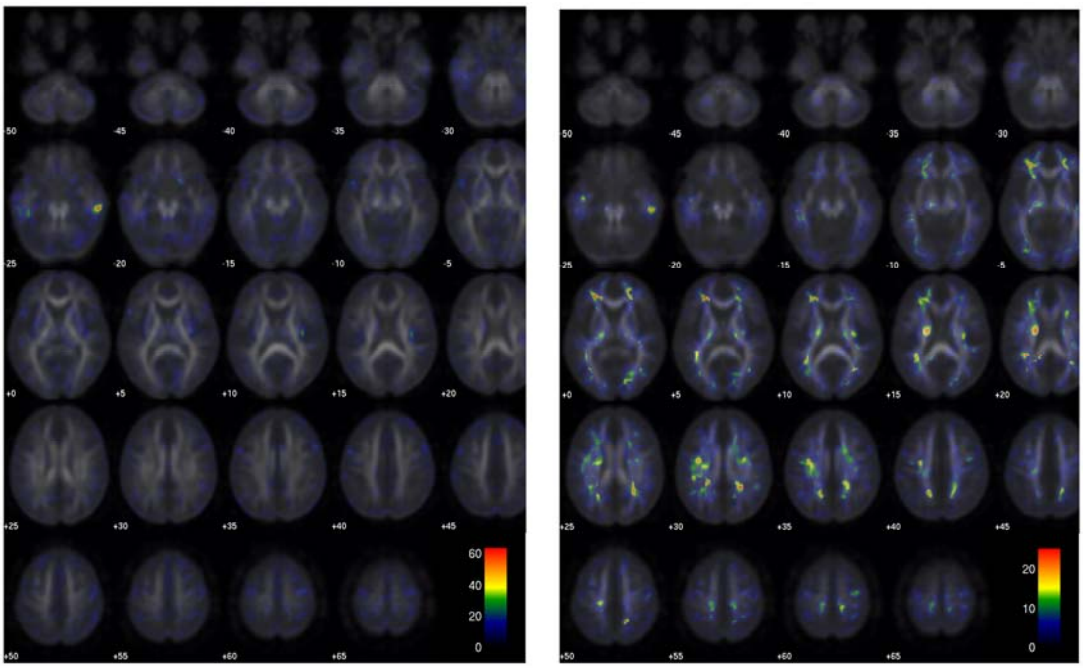

Figure 5.10 Statistical map of *F*-values from the LDA linear combination metric analysis segmented into (a) GM and (b) WM.

FA then, while not a strong candidate for univariate VBA of these data, is important on larger scales. *Mode* is different. While also weak across most voxels, it does show sensitivity at some (see the example in the next section). But at the larger histogram scale it shows no difference between boxers and controls. Its histogram in WM (Figure 5.11d) is interesting, in that it is both centred and skewed to the right; that is, away from planar diffusivity and towards increasing linear diffusivity. Only 6% of the WM voxels had *mode* < 0, which flags more planar propogation. Included in this range would be voxels with crossing fibres, so this figure suggests crossing fibres may not be very prevalent in these data.

Predictive Value

Since the predictive values and the linear combination statistic values are both derived from the same linear discriminant function, it might be expected that, by choosing suitable thresholds, the images of the maps of each would completely overlap. However, this was found not to be the case. Using a predictive value threshold of 0.8 (80% success rate), the results are shown in Figure 5.12.

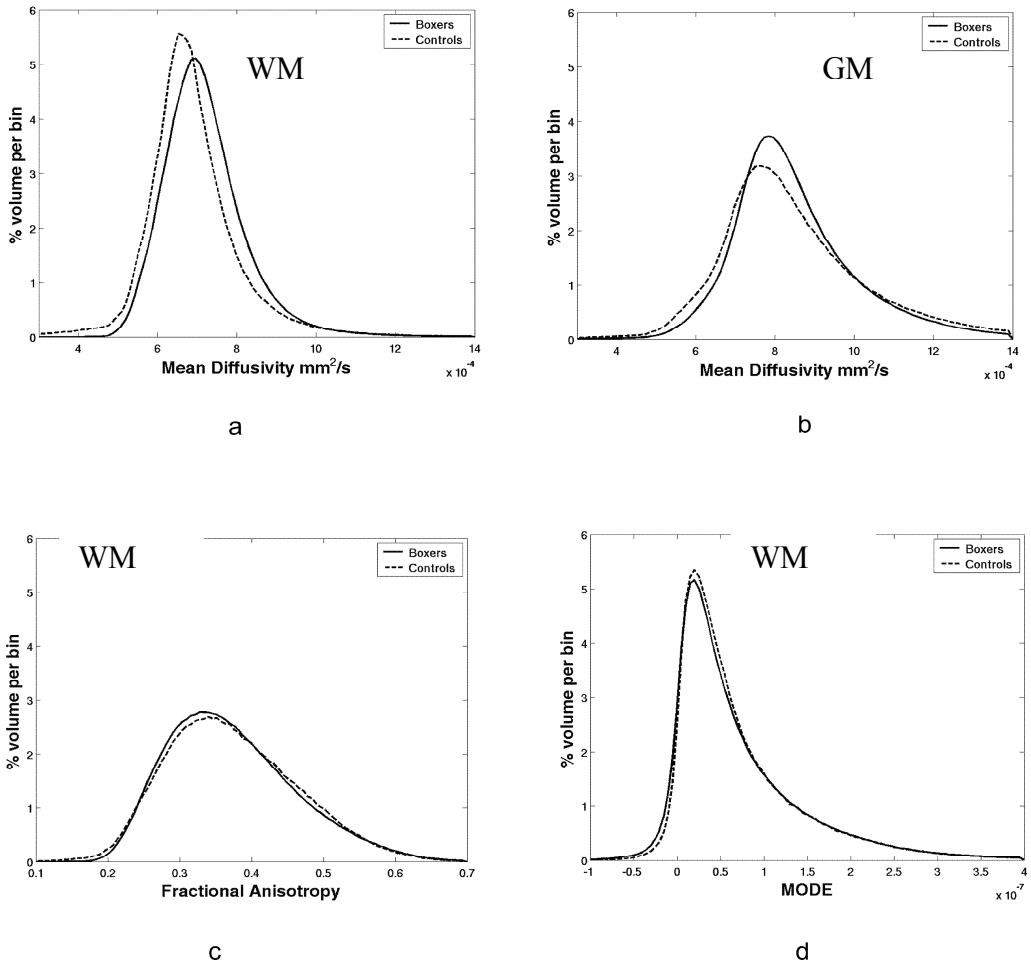

Figure 5.11 Histograms showing the number of voxels with each value of the metric as a volume percentage of the whole brain, using 500 bins.

By lowering the predictive ability threshold, more overlap could be achieved; nevertheless there are regions that predictive ability has identified and the linear combination has not. This is rather unexpected, and may result from the low number of controls (12) weakening the analysis when the linear combination metric is statistically analysed. The predictive ability values do not undergo this second stage of analysis.

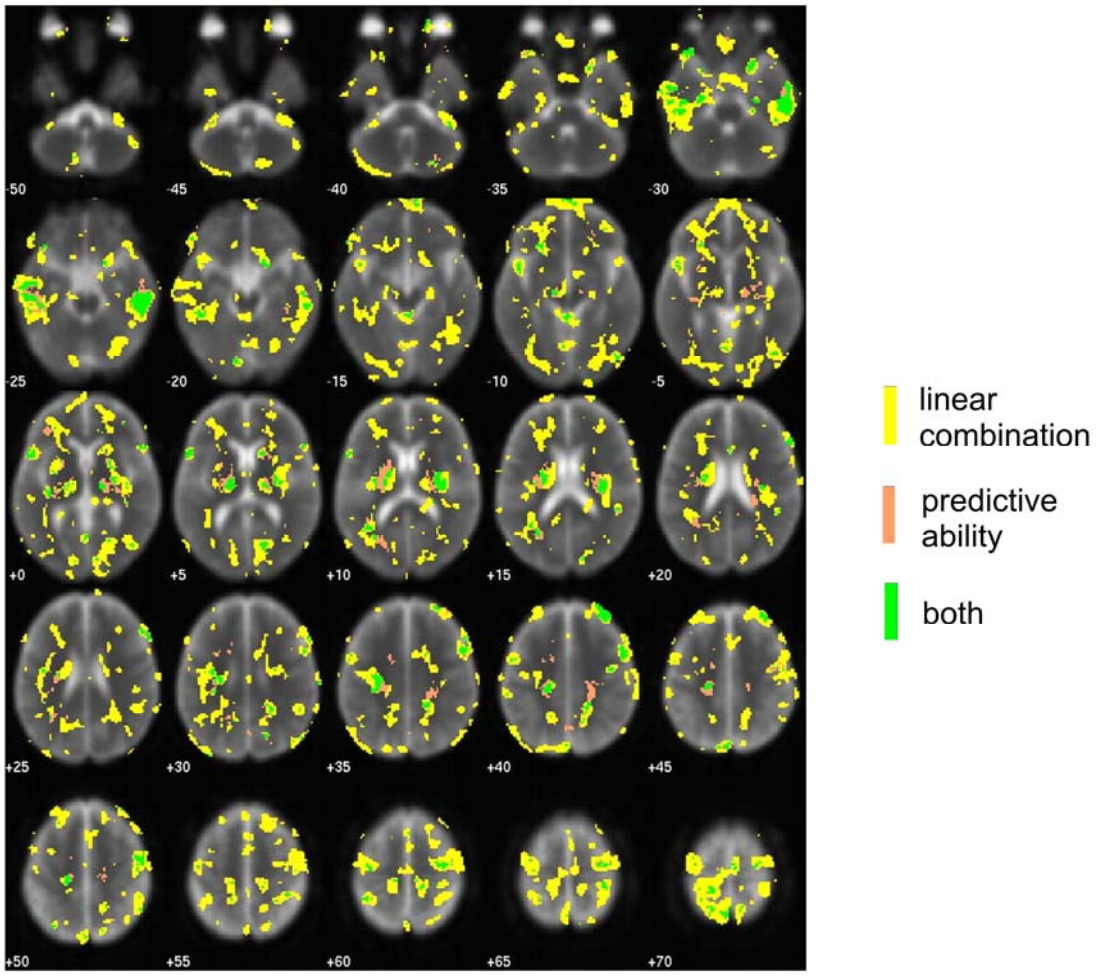

Figure 5.12 Comparison of LDA's "linear combination" metric and the "predictive ability" results from the same dataset.

5.7 Comparison of the Different Methods

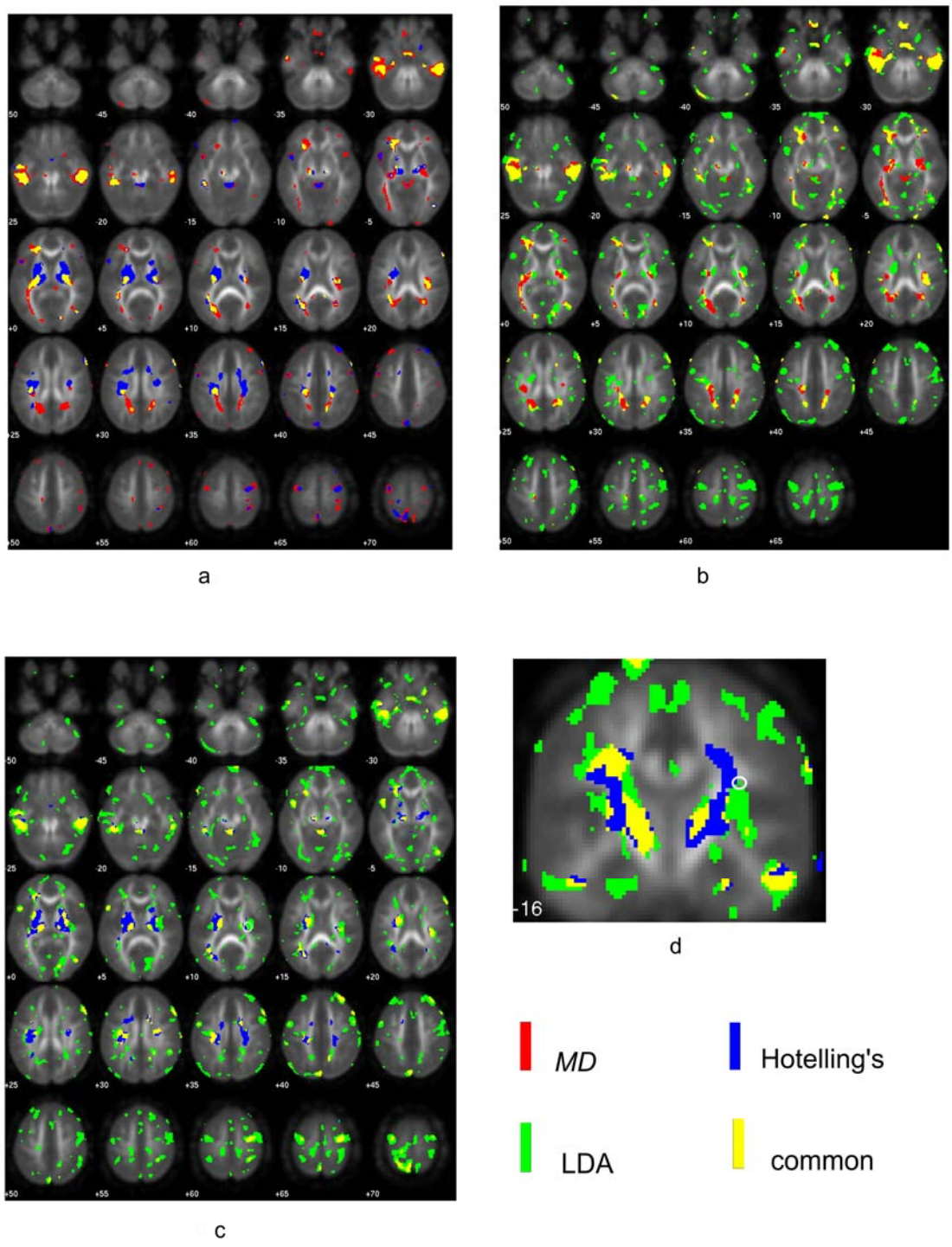

Figure 5.13 Differences between boxers and controls as identified by the displayed methods, and the voxels in common to those two methods.

Figure 5.13 shows a pairwise comparison between the multivariate (Hotelling's and LDA) and the univariate (*MD*) results. The regions unique to each method, and the regions common to both, are shown in different colours. Figure 5.13a shows that Hotelling's T^2 confirms the main area of damage identified by *MD*: bilateral damage to the region of the inferior temporal gyrus. In addition, however, the Hotelling's approach identified major subcortical damage in the striatum and thalamus that were not detected by *MD* alone. By contrast, Hotelling's did not detect some of the diffuse WM damage shown by *MD*.

Figure 5.13b and Figure 5.13c show that LDA provides the more sensitive multivariate approach. LDA supports the main damage identified by both the univariate *MD* analysis and the multivariate (*MD* and *FA*) Hotelling's analysis, although the extent of subcortical damage in the striatum and thalamus is less evident. An additional feature of the LDA analysis was that it revealed more diffuse microstructural damage than the other methods. Figure 5.13d is a coronal view of the damage to the subcortical and internal capsule regions, showing that the subcortical damage in boxers appears most prominent at the level of the posterior limb of the internal capsule when analysed with Hotelling's and LDA multivariate methodologies.

Table 5-1 quantifies the extent of the regions identified by the different methods, thereby showing the comparative sensitivities. Results of the hypothesis-testing methods (univariate, Hotelling's, and Linear Combination) are based on the calculation of the *F*- or T^2 - statistic thresholded at 11.41. The predictive ability results are based on a threshold of 0.8. Because the two thresholds are not directly comparable, it is not meaningful to quantitatively compare the predictive ability results with the other three methods from this table. It has been included for completeness, to compare its cross-tabulation results – i.e. how it performs *with* each of the other methods, rather than how it performs *compared* to them.

The diagonal elements of the table give the proportion of the brain identified as significantly different by the respective methods. LDA is 2.5 times as sensitive as Hotelling's, which itself is 1.25 times as sensitive as *MD*. The cross-tabulated, off-diagonal elements give the overlap, the conjunction, of the two methods being considered. The Hotelling's – Linear Combination pairing has the greatest overlap, i.e. the greatest number of "significant" voxels in common, with Hotelling's sharing 60%

Table 5-1 Proportion of the brain identified as statistically significant by both methods in the cross-tabulated pairings

	Univariate	Hotelling's	Linear Comb.	Predictive ability
Univariate	0.040	0.018	0.023	0.009
Hotelling's	0.018	0.050	0.031	0.017
Linear Comb.	0.023	0.031	0.126	0.018
Predictive ability	0.009	0.017	0.018	0.027

of its significant voxels with the Linear Combination. That same Hotelling's – Linear Combination overlap represented 62% of Hotelling's significant voxels and 25% of the Linear Combination's significant voxels.

The linear discriminant analysis is more robust than Hotelling's with respect to being effected by a weaker metric, since if one metric is weak at a particular voxel, it is down-weighted there without penalising the others. An example of the results of LDA at a single voxel in the insular cortex region (with MNI coordinates (36 -16 12)) is shown in Figure 5.14. This is a scatterplot of the *FA* of each subject against the *MD*, with boxers and controls plotted with different symbols for identification purposes. The LDA is then calculated and superimposed on the graph. Using metric values statistically normalised to a mean of 0 and standard deviation of 1, the discriminant function (Eq. 5.5) for this voxel was:

$$y = 0.0265 + 0.0116 \times MD_z - 0.0042 \times FA_z - 0.0384 \times mode_z$$

where the *z* subscript refers to normalised values. The coefficients show that at this voxel, *mode* is the strongest metric, followed by *MD*, with *FA* the weakest. This illustrates the importance of LDA – in this voxel important information about the difference in diffusion between the boxers and the controls is encoded in the *mode* metric. Univariate analyses (using *MD* or *FA*, since overall *mode* is too weak to use by itself) will lose this information. Furthermore, unlike in Hotelling's test where *mode* penalizes the others when it is weaker, this is not the case in LDA, which simply adjusts

the weights appropriately – including *mode* when it can contribute to identifying a difference between the groups, and down-weighting it when it cannot.

When this function is evaluated for an individual subject, a value of $y < 0$ (Figure 5.14, upper left) is classified as a normal brain map (control), while $y \geq 0$ (Figure 5.14, lower right) is classified as a different brain map (boxer). The predictive ability of the LDA in separating boxers from controls in the testing *mode* at this voxel was 0.90 (i.e. 90% of the individual subjects were correctly classified as a boxer or a control). For ease of visualisation in 2 dimensions, *mode* was omitted from the plot and the LDA. This of course gave different coefficients, and a reduced predictive value. This is done purely for illustrative purposes. *Mode* was omitted, even though it was the strongest metric in this voxel, to show the more widely used metrics *MD* and *FA*, and the relationship between them. Figure 5.14 also shows the expected pattern that, with non-acute head injury, *MD* increases and *FA* decreases (Inglese, et al. 2005; Salmond, et al. 2006) .

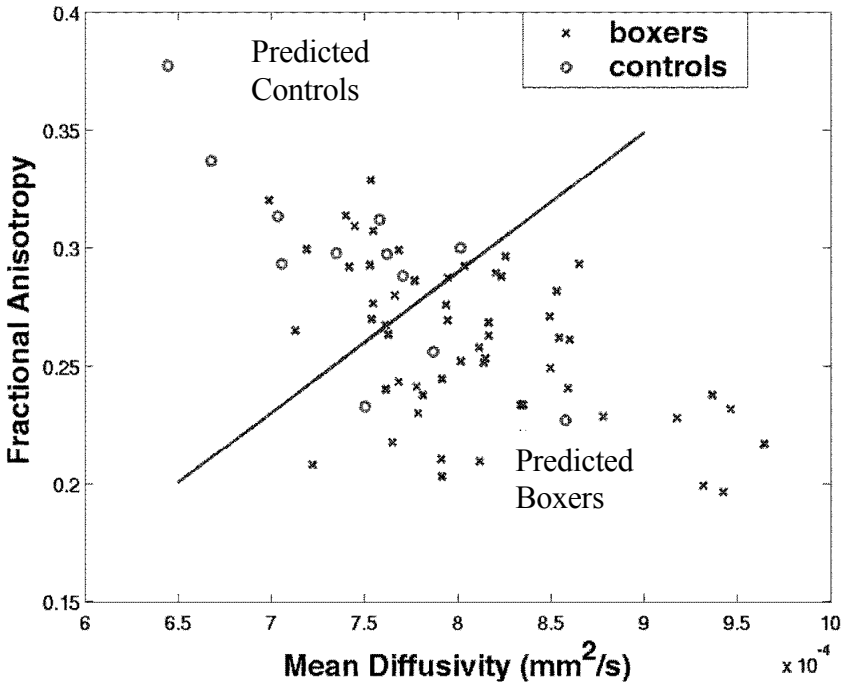

Figure 5.14 Scatter plot of FA v. MD for voxel with MNI coordinates (36 -16 12). The linear discriminant function with the FA and MD metrics (the "separator") is superimposed. The predictive ability using all three metrics in the LDA was 90%.

5.8 Conclusions

A special form of multivariate analysis – conjunction and disjunction analysis – produced inconclusive results, largely because of the unbalanced strengths of the input metrics. With balanced metrics they offer better options for improving the sensitivity or specificity of the analysis than just changing the *p*-value for the univariate analysis. However, whether they offer anything that the other multivariate methods used in this study do not remains unclear. Their requirements that the metrics be

- orthogonal for analyses
- well-balanced for conjunction (and in neuro imaging this is unlikely to be the case – the ADC metric will normally be more sensitive than the anisotropy metric)
- either well-balanced or else needing *p*-value optimization for disjunction

mean conjunction/disjunction analysis is not the preferred multivariate method.

Three more robust methods of analysing and displaying differences in brain structure between young professional boxers and an age-matched healthy control group using more than one metric have been presented. These approaches involve Hotelling's T^2 tests of multivariate data, Student's *t*-tests of multivariate data derived by LDA, and the predictive ability of the linear discriminant function.

These methods were used with the boxer data because multivariate analyses were hypothesised to be more sensitive to differences between groups than the most sensitive univariate analysis. This study supports this idea, with LDA being more sensitive than the Hotelling's method, and both of them more sensitive than any of the univariate tests. Both methods confirmed the findings of the most sensitive individual metric, of large-scale bilateral changes in the region of the anterior inferior temporal gyrus of the boxers. Further, multivariate analysis identified major subcortical changes that had not been evident with univariate analysis. A weakness of this retrospective study is the low number of control subjects, which considerably reduces the power of the analyses. This may be especially important given the imbalance between the "strengths" of the

different metrics. Despite this limitation, these new methods enable us to identify major subcortical damage in the brains of the professional boxers that was not evident using univariate analysis. With this increased sensitivity, segmented analyses were possible. These showed that the damage to the boxers was primarily in WM.

The Hotelling's analyses of the data showed improved specificity and comparable sensitivity with the best individual metric. The Linear Combination metric from LDA showed improvements in both sensitivity and specificity. Mapping the predictive value gives an alternative method for displaying tissue differences, and showed similar results to the Linear Combination method. The differences between the two LDA results suggest the predictive ability might be useful for low-powered studies. With large sample sizes, the two methods would be expected to give similar results.

Hotelling's and LDA methods complement each other and extend the findings of separate univariate analyses. LDA's linear combination was more sensitive and provided more detail of the microstructural damage in the boxers, while Hotelling's statistic revealed fewer, more consolidated subcortical clusters. Hotelling's highlights the most serious damage, while LDA reflects the diffuse nature of the mild, repetitive, closed head injury.

This study also supports previous reports that LDA may be able to make an important contribution in the clinical setting, where a positive or negative diagnosis is often required. LDA provides such a binary decision, based on multiple components.

6 Investigating the Use of Diffusion Tensor Data to Track Cognitive Decline in Parkinson's Disease

6.1 Background

The previous two chapters have explored the use of DTI data to identify abnormalities in the brains of the boxers by statistical comparisons of the boxers group with the control group. In this chapter I investigate the use of diffusion metrics as biomarkers of microstructural change. The study used here examined a sample of 12 patients with Parkinson's disease, and diffusion measures were investigated for their ability to track variation in cognitive ability in these PD subjects. In principle the approach could have potential in many different situations involving brain damage or degeneration. *MD* has been investigated as a bio-marker for cancers (Lee, et al. 2007; Moffat, et al. 2006; Theilmann, et al. 2004), brain tumors (Hamstra, et al. 2005), and traumatic brain injury (Huisman, et al. 2004). This voxel-based DTI investigation of bio-markers related to cognitive decline in PD is novel.

Parkinson's disease (PD) is a degenerative neurological disease with a diagnosis based on motor impairment (Gelb, et al. 1999). However, it is also recognised as being a far more complex multi-system disorder than one associated only with motor deficits (Hristova and Grozdev 2007; Idiaquez, et al. 2007; Owen, et al. 1992). Cognitive impairment adds a significant burden to PD patients, with many of them (possibly up to 80%) progressing to frank dementia, in which everyday personal, social and occupational function is severely compromised (Emre 2003; McKeith 2004).

Early attempts to assess cognitive decline in non-demented patients with well-defined Parkinson's disease investigated the predictive value of different motor symptoms (Caparroslefebvre, et al. 1995). These approaches have not gained widespread use. The motor status of PD patients does not adequately predict their cognitive status, although those in the more advanced stages tend to show more cognitive decline. MRI could provide the necessary tools with which to detect subtle brain changes associated with this cognitive decline and thus help inform future predictive models. Brain imaging has recently begun to be used to demonstrate differences between unimpaired and

cognitively impaired PD subjects. For example, an fMRI study found "significant signal intensity reductions during a working-memory paradigm in specific striatal and frontal lobe sites in patients with cognitive impairment compared with those patients who were not cognitively unimpaired" (Lewis, et al. 2003b).

Most MRI studies of PD to date have been volumetric, using T_1 images to determine the location and extent of atrophy. One such study sought to discover whether medial temporal lobe (MTL) atrophy correlated with cognitive impairment in PD and PD dementia (PDD) (Tam, et al. 2005). They reported that such atrophy was evident in both PD and PDD, and was not more pronounced in the latter. The authors concluded "that when dementia develops in PD, anatomic structures apart from the hippocampus are predominantly implicated." Another example used manually drawn ROIs to determine atrophy (Bruck, et al. 2004), and found that early stage PD subjects exhibited hippocampal and prefrontal atrophy.

DTI studies involving PD patients have only appeared in the literature in the last couple of years. Some of these have used *FA* measures to investigate white matter pathway integrity (see, for example, (Park, et al. 2007; Trivedi, et al. 2007)). One voxel based DTI analysis of PD found that "Patients with Parkinson's disease had significantly decreased FA in the region of interest along a line between the substantia nigra and the lower part of the putamen/caudate complex, in which most of the nigrostriatal dopaminergic neurones are included. Loss of FA in this region was obvious even during the early clinical stages of Parkinson's disease" (Yoshikawa, et al. 2004).

Dementia with Lewy bodies (DLB) is a disease closely related to cognitive impairment in PD. The clinical and causal distinction between DLB and PDD is not clear (Galvin, et al. 2006; Williams-Gray, et al. 2006). Indeed, DLB is often regarded as a similar, if not the same, disorder except that the individual did not commence with a prior motor disorder without dementia also being present. Therefore a study that found a potential role for DTI in tracking the progression of DLB (Bozzali, et al. 2005) is significant in the context of this thesis. Their findings support the hypothesis that DTI might provide different and important information about the progression of neuropsychological disease. Since DLB patients by definition are showing dementia, it is of interest to broaden the scope of the investigation to include both non-demented PD patients, who

have a range of cognitive impairments but do not reach the criteria for dementia, as well as PDD.

A recent voxel-based DTI study of 12 patients in early stages of PD and 12 controls investigated whether the trace of the tensor (which is effectively *MD*) could be used as a marker to identify future subjects at risk of developing PD (Scherfler, et al. 2006). Although significant changes in *MD* were found in some regions, such as both olfactory tracts, between the patients and controls, the results concerning its suitability as a marker were inconclusive. Their study suffers from three weaknesses:

1. A small sample size.

2. Being cross-sectional, it is using static information to try to draw conclusions about a progressive condition.

3. It does not include any subjects about whom results are being sought: non-symptomatic patients who are at risk of developing the illness at a later date.

My investigation of DTI measures as possible bio-markers of cognitive decline in PD has important similarities to and differences from this one:

1. With only 12 subjects, it too suffers from having a small sample size.

2. It too is a cross-sectional study where, ideally, a longitudinal one should be used. However, in an attempt to mitigate this and draw some helpful, albeit tentative conclusions, I have replicated the progression of cognitive decline in an individual by studying different subjects with a wide range of cognitive ability and impairment. This reflects the progressive development of the condition, rather than a simple binary categorization of "at risk" or "not at risk". A bio-marker that tracks such progression has great importance for the treatment and monitoring of the disease.

3. To test the ability of the diffusion metrics to track the progression of cognitive decline, I have introduced a more sophisticated and informative benchmark measure than the simple "PD patient" or "control" used by (Scherfler, et al. 2006). I used a neuropsychological measure (described later) that was based on

a wide range of cognitive abilities known to be sensitive to impairment in PD, and which therefore provided surrogate measures of cognitive decline.

This study has three main aims:

1. Using *MD*, *FA* and *mode* to identify *in vivo* regions where microstructural changes are associated with cognitive decline in PD, to determine whether these metrics could be bio-markers of this decline;

2. To discover whether a multivariate regression with all three diffusion metrics would provide a more sensitive approach than using each metric separately;

3. To find different ways of looking at the brain and of localizing the relevant microstructural changes. Three approaches were used to do this:

    a. Voxel based analysis, which has the advantages of being objective (not requiring any a priori information) and covering the whole brain. It is not restricted to the boundaries of anatomically defined regions of interest, and therefore is able to show where structural abnormalities cross these boundaries. Its disadvantage is that a voxel by itself is too small to be of interest; rather it is the clustering of voxels together that is of interest. However, defining what grouping of voxels constitutes a cluster, and comparing the relative significances of different clusters, is problematic.

    b. Region of interest (ROI) analyses using pre-determined anatomical regions. The size of these regions makes them of interest in themselves. The risk in averaging the data over a region for this approach is that smaller, subtle sub-regional differences will become masked.

    c. Meta-regions were constructed by an expert operator to reflect the functional nature of specific cognitive skills. This entailed combining the ROIs that were known to have some involvement in the cognitive task being considered into a single meta-region.

An advantage of DTI metrics as bio-markers is that they can be evaluated at all three of these scales. This offers considerable flexibility in identifying structural changes in the brain that are related to cognitive impairment.

Increased appreciation and understanding of cognitive heterogeneity and the progression of cognitive decline in PD are among the highest priorities facing researchers today. The identification of relevant markers is fundamental to identifying patients at risk of dementia and for targeting treatment and prevention of this important non-motor characteristic in PD.

6.2 Subjects and Methods

6.2.1 Overview

Diffusion tensor MRI data were acquired in Christchurch from 12 patients with a diagnosed PD confirmed by a specialist neurologist (Prof Tim Anderson). These patients were selected expressly on the basis of clinical judgment of variation in cognitive ability, ranging from intact everyday cognition through to those who expressed some difficulty and/or early signs of frank dementia. Formal neuropsychological testing was undertaken (by a suitably trained masters student in psychology, Saskia van Stockum) which spanned 5 general domains sensitive to the range of cognitive impairments that can be expected in PD and PDD patients. These tests provided measures of cognitive decline, including visuoperception, executive function, working memory, problem solving and episodic memory, and standardized scores were used to generate a global score relative to normative data (Total Neuropsychological, or TotNP). The TotNP score ranged from zero (unimpaired) to a maximum score of 25 (equivalent to severe cognitive impairment in each domain; see details below). Regression analyses of TotNP against the DTI metrics were then performed.

6.2.2 MR Data Acquisition

Diffusion tensor MRI data were acquired using the GE 1.5T scanner at Southern Cross hospital in Christchurch, using a single shot 2D spin echo EPI acquisition with TE/TR = 90ms/10s. Data were acquired axially with a matrix of 128 × 128 × 30 covering a field of view of 240 mm × 240 mm × 150 mm, with 25 uniformly distributed gradient

directions, with a *b*-value of 1000 s/mm^2, and 3 acquisitions with no diffusion weighting (total acquisition time 4 min 40s).

6.2.3 Neuropsychological Tests

The Mini-Mental State Examination (MMSE) (Ankrom, et al. 2002) is one of the most commonly used instruments for assessing cognitive impairment in neurological diseases. It has been used for nearly 30 years, and has gained widespread acceptance. However, it is not without its shortcomings, as has been pointed out (Simard 1998). These include:

- A lack of sensitivity in the early stages of dementia (Nelson, et al. 1986; Simard and van Reekum 1999). As discussed earlier, with healthcare in the 21st century moving towards early intervention, this is a particularly serious weakness;
- Limited measures of memory functions, including only minimal assessment of working memory;
- No assessment of executive functions.

In summary, MMSE does "not measure all cognitive domains" (Athey and Walker 2006). Domains related to cognitive decline and dementia in PD include the following, with a short description of the measures used in this study:

1. Episodic verbal memory (Hamilton, et al. 2004; Janvin, et al. 2005; Levy, et al. 2002; Troyer, et al. 1998). The measures used included the total correct scores for trials 1-4 of the California Verbal Learning Test (CVLT) Short Form and CVLT Long Delay, which emphasise strategic aspects of learning and memory.
2. Executive function (Azuma, et al. 2003; Litvan, et al. 1991; Mahieux, et al. 1998; Piatt, et al. 1999). The measures used included Delis and Kaplan's verbal (FAS) fluency test and an Action (verb) fluency test.
3. Problem solving (CroninGolomb and Braun 1997; Croningolomb, et al. 1994). One measure was used: the Matrix Reasoning test from the Wechsler Abbreviated Test of Intelligence, which examines visuoperceptual problem solving skills.

4. Working memory (Dalrymple-Alford, et al. 1994; Lewis, et al. 2003a; Werheid, et al. 2002; Woods and Troster 2003). The measures used included the Wechsler Digits Backwards test and the Werheid et al. Digits Ordering Test.

5. Visual perception (CroninGolomb and Braun 1997; Dalrymple-Alford 2001; Levin, et al. 1991; Mahieux, et al. 1998). The measures used included the Fragmented Letter test from the Visual Object and Space Perception battery and the Judgment of Line Orientation test.

Using these domains, for this study a combined measure of the scores obtained from neuropsychological tests in these domains was derived. Cognitive tests were employed on the basis of probable sensitivity to PD, dementia in PD and/or the related disorder, dementia with Lewy Bodies, and were thus expected to be among the most useful in identifying cognitive heterogeneity and progressive impairments in PD. The list is very close to a summary by (Marinus, et al. 2003) who identified "domains" of attention (predominantly working memory), memory and learning, executive functions, visuospatial functions, but less so verbal functions and general thinking and reasoning, as being important in PD (different workers use slightly different terms and specific tests when describing "domains").

Other researchers have selected similar groupings of these domains. Examples include visual memory, visuospatial ability, and executive functions (Janvin, et al. 2003); memory and executive function (Huang, et al. 2007); and attention, memory, visuospatial functions, and executive functions (Vingerhoets, et al. 2003).

One review of cognition in PD (Dubois and Pillon 1997) suggested the following: visuospatial functions, working memory, long-term memory, implicit memory (but which is problematic as it is often dependent on motor skills) and executive functions (in which they include problem solving). Their main concern was to provide an overall evaluation that would also provide relevant summaries of pertinent individual domains.

Based on normative data obtained from the relevant professional manuals or published literature, each participant's measure was categorized as follows:

If the standardized score was found to be below the normative mean by …	… then it was assigned the score of …
more than 2.5 standard deviations	5
between 2.5 and 2 standard deviations	4
between 2 and 1.5 standard deviations	3
between 1.5 and 1 standard deviations	2
between 1 and 0.67 standard deviations	1
less than 0.67 standard deviations	0

The scores were averaged within each domain, and then the resulting 5 values were aggregated to produce the "TotNP" score. For example, a TotNP score of "16" could mean a score of 4 across four domains with the fifth intact (i.e., "0"); or 2 domains scoring 4 and the others scoring 3, 3 and 2 respectively.

The assumption is that an increase in TotNP is associated with increasing cognitive impairment in PD, which may be caused by distributed changes in the structure of the brain. Since diffusion measures are also sensitive to changes in structure, this study investigated whether changes in TotNP could be explained by the changes in one or more diffusion metrics. If so, then these diffusion metrics could be used to track changes in the cognitive state of a PD patient. The advantage is that diffusion measures can be used to interrogate brain structure at various scales, down to the voxel level.

TotNP was also used to classify each patient as belonging to one of the following categories (similar standard divisions for category 1 and category 2 have been used by Dalrymple-Alford and his co-workers, e.g. (McKinlay, et al. 2004)):

1. PD-U: Unimpaired cognition or evidence of only minimal impairments. A maximum of two of the five cognitive domains below -0.67 SD/25th percentile rank of normative reference data, including a maximum of only one measure below -1.0 SD/16th percentile, and no measures below -1.5 SD/7th percentile;

2. PD-I: Mildly impaired. This includes:

    a. Patients with mild cognitive impairment (MCI). These were defined as having objectively documented cognitive decline on the cognitive measures, including minimal evidence of -1.0 SD/16th percentile on two of the five cognitive domains and at least -0.67 SD/25th percentile on a third domain (in my colleagues' experience, matched controls usually score slightly above average relative to the normative data on these tests)

    b. Patients who do not fit either category 1 or 3;

3. PD-D: Objectively documented impaired cognition, with impairments in any 2 or more of the five domains at -2.0 SD/3rd percentile and at least -1.5 SD/7th percentile in a third domain.

6.2.4 Statistical Analysis

As well as regression analyses, rather than more traditional between-group comparisons, another departure from the methodology of the previous chapters is in the data used to draw conclusions. Besides standard hypothesis testing, with a null hypothesis that the regression line has zero gradient, regression offers another potentially more useful statistic: the regression coefficient R^2. One of its main advantages over *t*- or *F*-statistics is that it makes no assumptions about the underlying distributions. There is, of course, still the risk of some correlations being detected by chance. So a sensible R^2 threshold must be applied to minimize this risk. Thresholds in other areas of research typically range from an R value between 0.5 (Loucks 1997) and 0.7 (Mtumbuka and Edwards 2004) (i.e. R^2 between 0.25 and 0.49). A seminal functional MRI study did a pixel-by-pixel correlation of signal intensity with the stimulus protocol and used a threshold of R = 0.5 (Boecker, et al. 1994). I chose to be on the conservative side and selected $R^2 = 0.5$ (R = 0.71) as the criterion.

With spatial normalization of the images being a critical factor in imaging analysis, and often being the limiting factor in population studies with different subjects, it is important to be as confident as possible that the process is working maximally. There are as yet no suitable quantitative measures of the accuracy of the process, so qualitative

comparisons are all that is possible. With the intensity-based (non label-based) normalization done by SPM, the template must have the same general intensity distribution as the image being normalized.

Since the data for this study were acquired using an EPI sequence, there were two templates that met this requirement – EPI and T_2. As distinct from T_1 for example, both the EPI and T_2 templates have CSF displayed as hyperintense, as does the EPI image. However, a disadvantage of the T_2 template is that it produces a layer of hyperintense fat around the scalp. Spin echo EPI sequences such as those used to gather the data in this study include spectral spatial pulse fat suppression, so the EPI template is generally preferred. The three templates are shown in Figure 6.1. For comparison, two of the most poorly aligned images were selected and normalized to the T_2 and EPI templates. The results are shown in Figure 6.2. Qualitatively, there is little between the resulting normalized images. The EPI template was therefore selected for normalization.

The diffusion tensor was then fit at each voxel, and from this the frame-independent *MD*, *FA* and *mode* were calculated. After normalization, these images were smoothed using an 8 mm FWHM Gaussian kernel. In-house software written in Matlab performed simple and multiple linear regressions of the selected neuro-psychological score with the selected diffusion metric or metrics. Various levels of analysis were then performed.

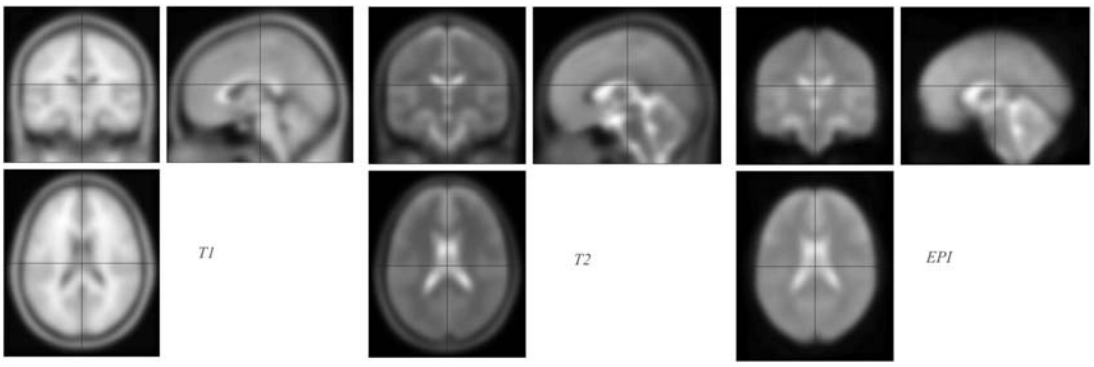

Figure 6.1 The Montreal Neurological Institute (MNI) T_1, T_2 and EPI templates available for spatial normalization of images.

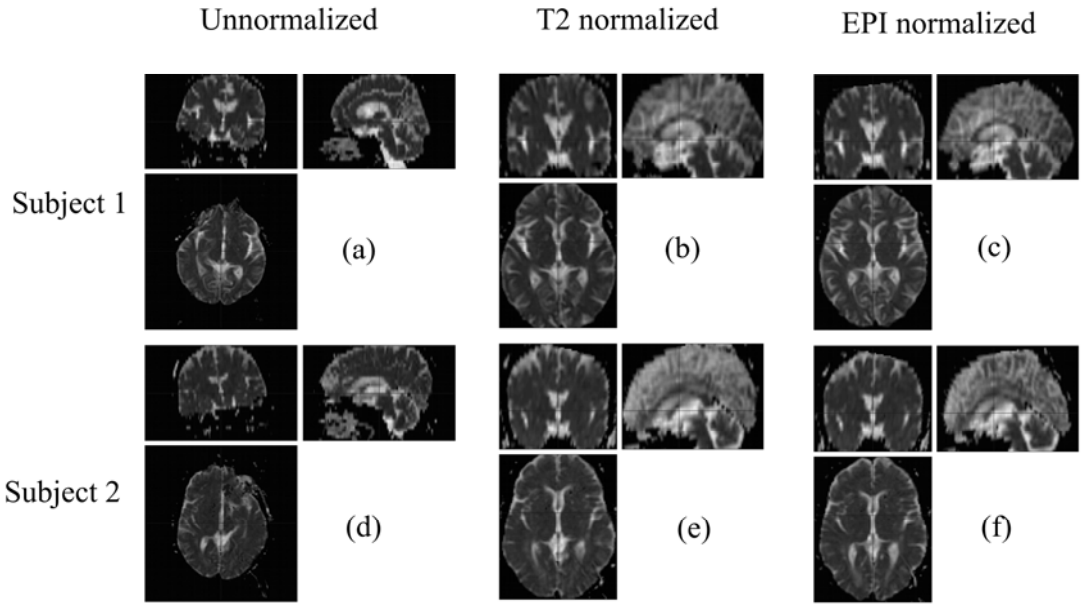

Figure 6.2 Sections of two different subjects (a-c and d-f respectively), unnormalized (a, d), normalized to the MNI T_2 template (b, e), and normalized to the MNI EPI template (c, f).

1. Voxel-based analyses (VBA) over the whole brain, using either TotNP or MMSE as the independent variable.

2. Region of interest (ROI) analyses. These averaged the diffusion values of all the voxels in the ROI, and regressed these against TotNP. (Since TotNP showed stronger correlation with the diffusion metrics – see Results section – it was used in preference to MMSE.) The appropriate voxels were identified using the relevant masks in MarsBar (Brett, et al. 2002) for the hippocampus and parahippocampal region, caudate and putamen, thalamus, and amygdala.

3. Domain-specific analyses. This represented a more functional analysis of the situation than the anatomically-defined ROI approach. It was driven by the knowledge that few, if any, brain functions and operations are the sole preserve of a single anatomical region such as the hippocampus. Several quite disparate and distinct parts of the brain can contribute to complex functions such as episodic memory. This functional investigation entailed forming four new meta regions, based on the four domains of TotNP:

a. Episodic memory
b. Executive function
c. Working memory
d. Visual perception

So, for example, all the anatomical ROIs that might primarily be expected to be involved in episodic verbal memory were included in the first meta region. Problem solving was not included because it probably reflects more distributed neural system involvement.

6.3 Results and Discussion

6.3.1 Comparison of MMSE and TotNP

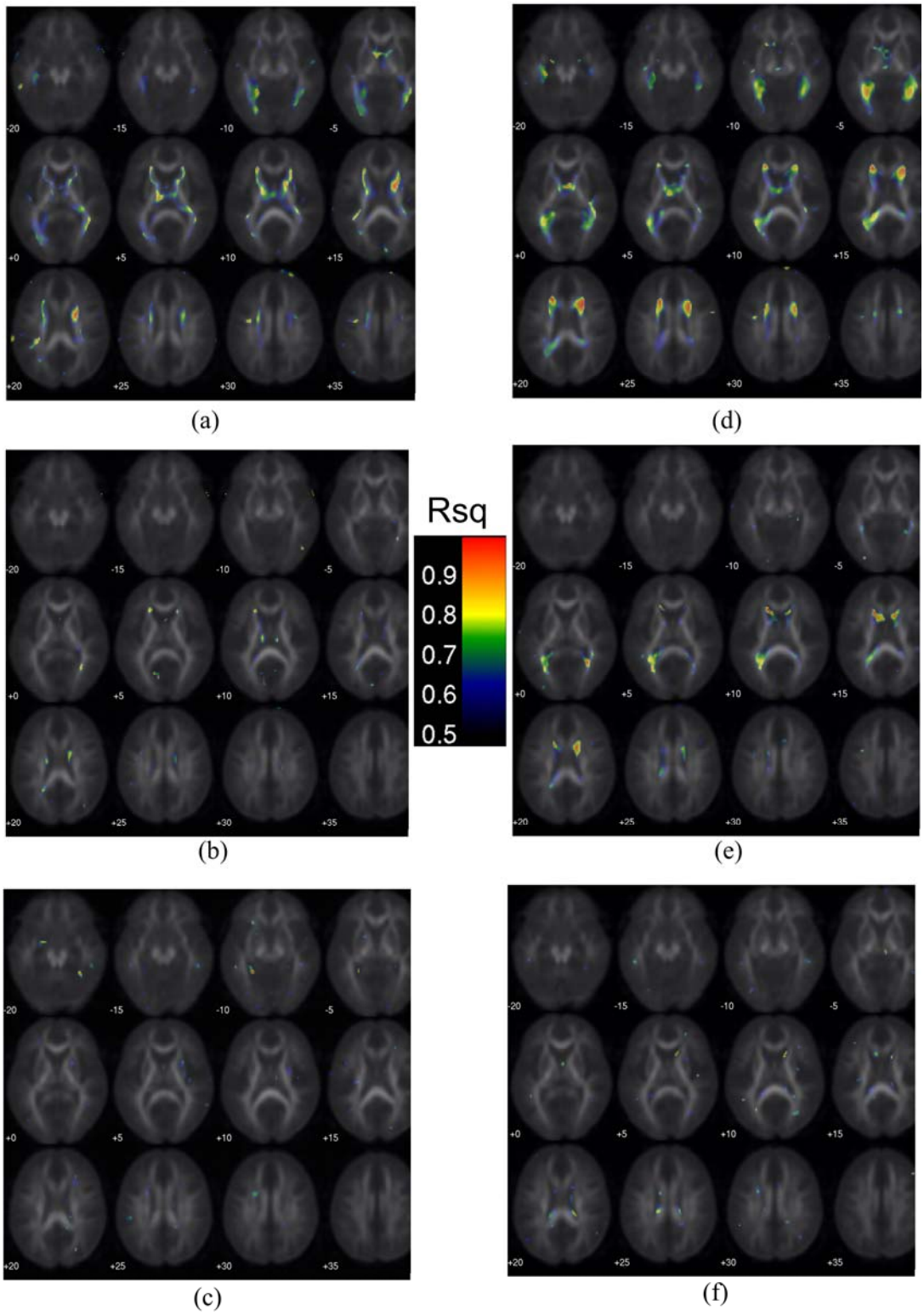

Figure 6.3 R^2 values of univariate regression of *MD, FA* and *mode* against MMSE (a-c, respectively) and against TotNP (d-f, respectively), with an R^2 threshold of 0.5.

The three metrics, *MD, FA* and *mode*, were individually regressed firstly against MMSE, then against TotNP at a voxel level. The results are shown in Figure 6.3Figure 6.3, with an R^2 threshold of 0.5 (i.e. a correlation coefficient threshold of 0.7) so only the strongest correlations are displayed. From these results it is clear that TotNP has a stronger overall correlation with all three diffusion metrics than MMSE. Since both TotNP and MMSE represent neuro-psychological bio-markers of cognitive decline, an investigation of whether diffusion measures can also be used as bio-markers needs the most sensitive comparison available. For this reason, TotNP was used as the regressor in the remaining analyses.

6.3.2 Investigation of Imaging Bio-markers

1. Voxel-based analyses (VBA)

The three diffusion metrics, *MD, FA* and *mode*, were individually regressed firstly against MMSE, then against TotNP at a voxel level. The results are shown in Figure 6.3, with an R^2 threshold of 0.5 (i.e. a correlation coefficient threshold of 0.71) so only the strongest correlations are displayed. From these results it is clear that TotNP has a stronger overall correlation with all three diffusion metrics than MMSE. Since both TotNP and MMSE represent neuro-psychological markers of cognitive decline, an investigation of whether diffusion measures can be used as bio-markers for this decline needs the most sensitive comparison available. For this reason, TotNP was used as the dependent variable in the remaining analyses.

Voxel based analysis revealed voxels with strong correlation between one or more diffusion metric and the TotNP score, with R^2 values up to 0.9. Figure 6.4Figure 6.4 compares the different analyses. It shows that of the three individual metrics, *MD* is the most sensitive, with *FA* and *mode* being considerably weaker. When the analysis was repeated with all three metrics in multiple regression, Figure 6.4d shows visually that increased sensitivity was achieved.

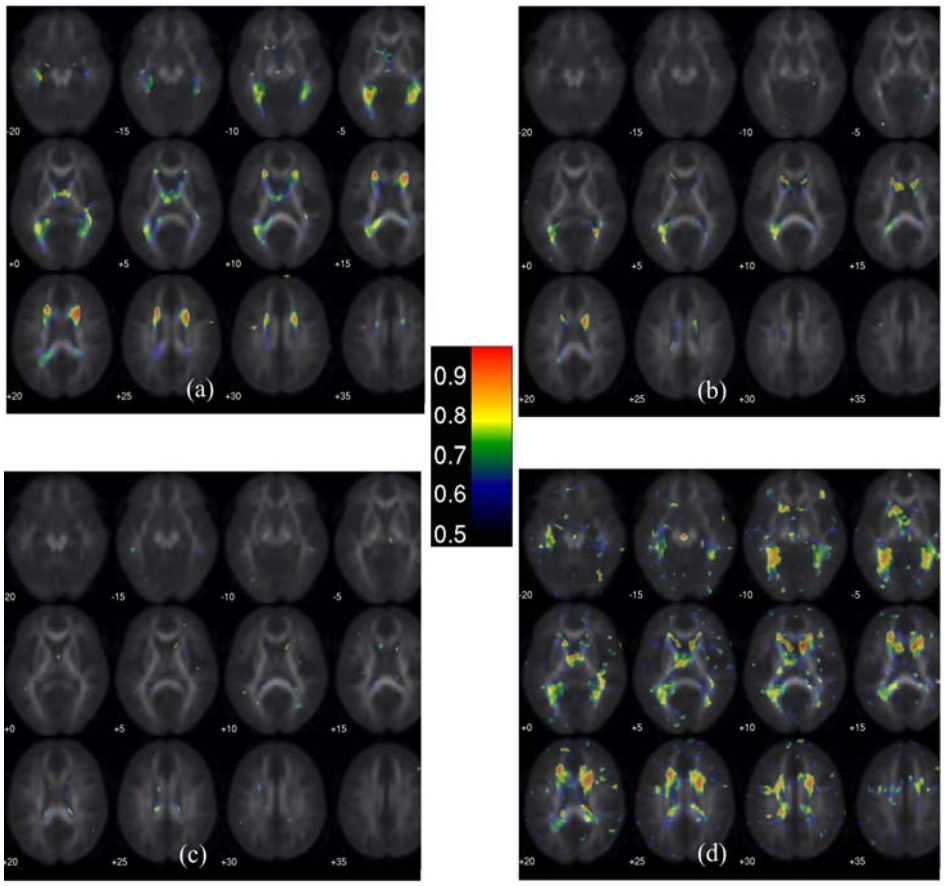

Figure 6.4 Comparision of different analyses: colour maps of R^2 values at each voxel for different metrics regressed against TotNP, superimposed on an FA template of a normalized, undamaged brain, for (a) mean diffusivity (b) fractional anisotropy (c) mode (d) multiple regression of all 3 metrics.

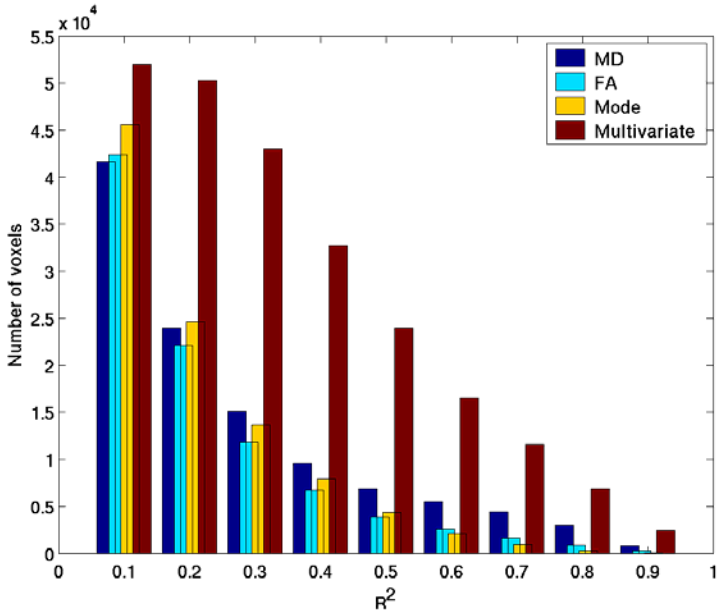

Figure 6.5 Sensitivity comparisons: bar graphs of the number of voxels in each R^2 range, for different metrics regressed against TotNP at every voxel, with no R^2 threshold imposed.

Multiple regression analysis (Figure 6.4d) suggested more marked abnormalities across similar brain regions to those identified by *MD*, together with increased evidence of diffuse cortical degeneration. This is an important finding, showing that, as well as the choice of diffusion metrics, the analysis method employed can also affect the apparent suitability of the metrics as bio-markers. The multivariate approach enhances the power of the procedure to detect a relationship between the metrics and cognitive impairment.

Figure 6.5 shows a quantitative comparison of the different analyses. A quantitative measure of the relative sensitivity of the different measures over the range of interest ($R^2 > 0.5$) is shown in Table 6-1. This highlights the superiority of using multivariate methods, which here are more than three times as sensitive as the best univariate analysis (*MD*).

Table 6-1 Number of voxels with $R^2 > 0$ for each method, also expressed as a proportion of the number of multivariate voxels, indicating relative sensitivity.

Method	No. of Voxels	Proportion of multivariate
Multivariate	49084	1.0
MD	15467	0.32
FA	6182	0.13
Mode	3784	0.07

2. Region of interest (ROI) analyses.

Regions known to be susceptible to changes during PD are:

- caudate/putamen (Hegde, et al. 2006);
- hippocampus/parahippocampal regions (Bertrand, et al. 2003; Braak, et al. 1996; Junque, et al. 2005);
- thalamus (Braak, et al. 1996; Hegde, et al. 2006);

The caudate/putamen plays an important role in learning and memory (Middleton and Strick 1994). Also, as part of the basal ganglia, it is responsible for the control of voluntary movement (Alexander, et al. 1990).

The hippocampus has an important role in declarative memory, and spatial awareness and navigation (Bliss and Collingridge 1993; Eichenbaum 2006; Nadel and Moscovitch 2001; Olton, et al. 1979).

The thalamus has multiple functions. These include (McCormick and Bal 1997; Schmahmann 2003):

- Regulating states of sleep and wakefulness, and general consciousness;
- Regulating arousal, the level of awareness and activity. Damage to the thalamus that inhibits this function leaves the subject in a state of coma.
- Motor performance
- Learning, memory and executive functions.

At the ROI scale, each metric was averaged across all the voxels in the region being considered, for each subject. These three averages for each subject were then used in multiple regression against TotNP. The results (Table 6-2) reveal high R^2 values for the three regions identified above. To have such strong correlations over whole regions suggests that diffusion metrics could well have an important role to play as bio-markers of cognitive impairment in PD.

Table 6-2 Results of multiple regression against TotNP at different regions of interest.

ROI	R^2
Caudate/putamen	0.82
Hippocampus/parahippocampal	0.74
Thalamus	0.64

Figure 6.6 shows the correlation of TotNP with *MD* in the hippocampus/ parahippocampus as an example of ROI results. This is an extremely important region of the brain and is the subject of intensive research in neuroscience. Although having only 12 subjects means that any conclusions are tentative, this graph is nevertheless an important first step in suggesting that imaging could well provide important bio-markers that are able to track the differences in cognitive ability of PD patients.

Using a single metric (for ease of visualization) in Figure 6.6 produced an R^2 value of 0.65. This compares with a value of 0.74 for the same region when multivariate regression is used, showing the value of multivariate analyses.

However, it is unclear from these results whether there is a continuous progression along the regression line, or whether there is a clear split in the distribution between patients with dementia and those without. The former situation would be the preferred one in terms of being able to use the imaging bio-marker to predict the onset of dementia. It may also be possible for volumetric changes in some subjects to have contributed to the apparent diffusion changes (an enlargement of the ventricles, for example, can cause a spurious apparent increase in *MD*). A larger sample size is needed to help answer these questions.

3. Domain-specific meta-region analyses.

The four domain-specific meta-regions are shown in Figure 6.7. They are:

1. Prefrontal cortex (working memory)
2. Hippocampal/parahippocampal regions (episodic memory). (Note: this meta-region is the same as the hippocampus/parahippocampus ROI used in the previous section.)
3. Occipito-parietal cortex (visuo-perception)
4. Basal ganglia and frontal cortex (executive function)

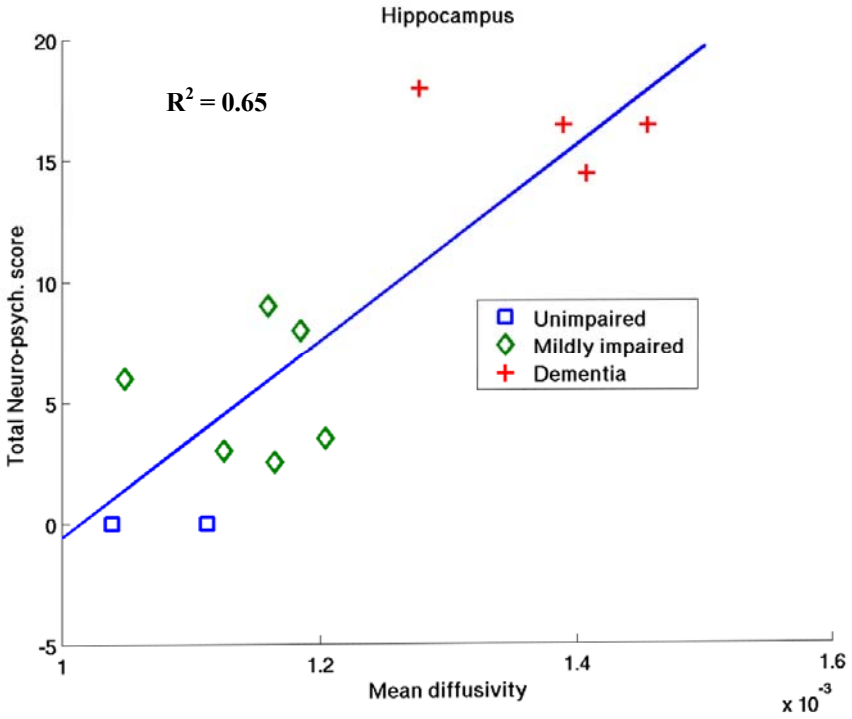

Figure 6.6 Correlation between total neuropsychological score (TotNP) and mean diffusivity (MD) in the hippocampal/parahippocampal regions, showing MD tracking differences in cognitive abilities from unimpaired cognition through to dementia.

By constructing meta-regions relevant to the cognitive impairment known to occur in PD it was thought that stronger correlations would be found between the neuropsychological variables and the diffusion metrics than with the pre-defined anatomical ROIs used above.

As well as regressing the diffusion metrics against TotNP, they were also regressed against the appropriate domain-component of TotNP for the particular region. This was done to test the hypothesis that meta-region regression would be more powerful when done against the appropriate domain rather than against the combined TotNP.

The results of these two analyses are recorded in Table 6-3. These data have two interesting features. Firstly, the R^2 values with TotNP were not higher in the meta-regions than in the anatomical ROIs (Table 6-2). In fact, overall they were considerably lower. Secondly, when TotNP was replaced by the domain component matching the meta-region, considerably stronger correlation was observed with the hippocampus/

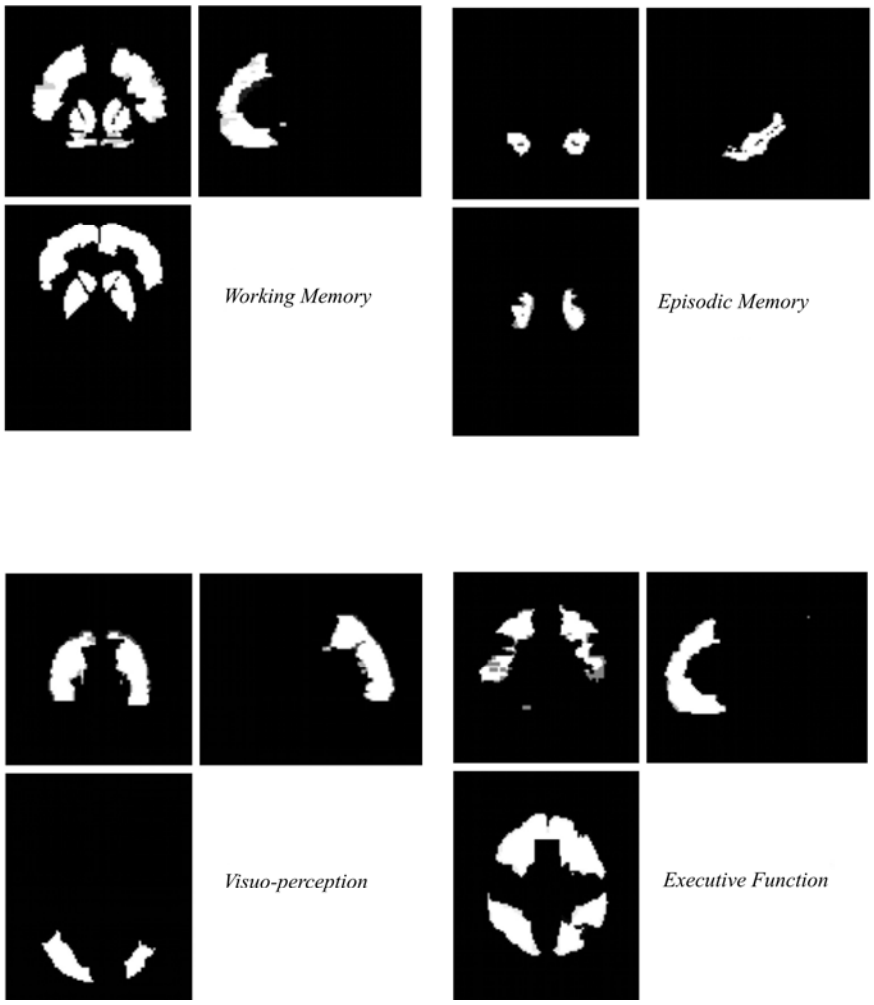

Figure 6.7 Three-plane sections of the four meta-region masks. For each triad top left is coronal, right is sagittal and bottom is axial.

parahippocampus and episodic memory. This meta-region already showed strong correlation with TotNP, and in increase in R^2 from 0.74 to 0.81 (which is an increase in R from 0.86 to 0.90) confirms the importance of the hippocampus/parahippocampus as a region of cognitive impairment. This result also shows that episodic memory is noticeably affected, and this may be a preferable domain to use in future diffusion bio-marker investigations rather than the full TotNP, at least in the hippocampus/ parahippocampus.

The other three regions showed weaker correlation with their respective domain components. Since they already had only weak correlations with TotNP, little can be inferred from this result.

These results therefore show that where there is a strong correlation between the diffusion metrics and neuropsychological scores, this can be strengthened further by selecting the appropriate domain score as the regression variable.

Table 6-3 Results of multiple regression of averaged diffusion metrics in each region against TotNP and against the domain-specific component of TotNP.

Meta-region	R^2	
	TotNP	**Domain component**
Occipito-parietal cortex (visuo-perception)	0.19	0.10
Hippocampal/parahippocampal (episodic memory)	0.74	0.81
Prefrontal cortex (executive function)	0.21	0.11
Basal ganglia/frontal cortex (working memory)	0.29	0.23

6.4 Conclusions

It should be reiterated at this stage that this study had a quite specific purpose – the investigation of biomarkers of cognitive decline in PD. The results presented here therefore relate only to that, and not to the neurostructural changes causing motor decline. Since TotNP was derived from five cognitive domains, it would be expected to be only very weakly correlated with motor impairment. (UPDRS scores were not available to test this hypothesis.)

Using diffusion metrics as surrogates of cognitive decline, and with the caveat that this was not a longitudinal study, these results suggest the following:

1. The hippocampal, caudate/putamen, thalamic regions and diffuse cortical regions are susceptible to microstructural changes affecting the progression of multiple cognitive decline in PD. There is thus some overlap with the regions found in the DLB study mentioned earlier (Bozzali, et al. 2005), and related PD studies.

2. *MD*, rather than *FA* or *mode*, may provide a sensitive univariate bio-marker, but the inclusion of all three diffusion metrics is likely to be a far more sensitive index of microstructural neuro-degeneration associated with these cognitive changes. An appropriate way of achieving a single bio-marker from the three diffusion metrics would be to use the linear combination metric derived using linear discriminant analysis methodology described in the previous chapter. This requires the inclusion of data from a control group, which was not available for this study.

3. Episodic memory may be the preferred domain with which to perform future tests of diffusion metrics for suitability as bio-markers of cognitive decline in PD.

7 Multi-modal Analysis: DTI and fMRI Connectivity in a Working Memory Task

7.1 Introduction

In the past decade, functional neuroimaging studies have significantly advanced our understanding of human cognitive functions. However, the advance in (our understanding of) human brain anatomy has been limited. (Takahashi, et al. 2007)

With DTI giving information about the structure and connectivity of the brain and fMRI giving information about function, combining both modalities in the same study can make important links between function and structure. In particular, of considerable interest are the fibre tract connections between distinct regions of the brain – for example, regions that are co-activated during a certain functional paradigm. FMRI can be used to identify regions of interest that are then used as the seed/terminal regions for DTI tractography. The importance of using activation-based regions as seeds and terminals rather than pre-defined anatomical regions is that distributed neural systems often involve many cognitive processes, especially "higher order" cognitive processes. Using regions that are co-activated by the same memory task, for example, will identify the particular connectivity between those regions, and therefore show the connectivity and the neuronal network that is known to be related to that memory task. Using more general regions as seeds and terminals does not allow for this degree of functionally specific identification of the fibre bundles.

The motivation for this study using DTI was thus two-fold:

1. It is feasible that activation-based tractography could provide diagnostic information for degenerative diseases. For example, working memory impairments are common in PD (Dalrymple-Alford, et al. 1994) and Alzheimer's disease (Celone, et al. 2006), and may be predictive and/or increase in patients who progress to dementia (Perry and Hodges 1999; Woods and Troster 2003). Should connectivity be shown to be reduced even when functional activity itself does not show a strong reduction at an early stage of significant decline in cognition, then connectivity may provide a potentially

important predictive tool. This will especially be true if, in the future, tractography methodology is able to quantify the connectivity. At that point, such information would also be an important addition to linear discriminant analyses (see Chapter 5), giving them an important extra variable.

2. While the main tracts joining regions of the typical brain are well known, activation-based tractography shows the actual fibre pathway layout for a particular individual. This could prove to be an important alternative to the more traditional pre-defined region-based connectivity for identifying specific functionally-related bundles. It would identify actual physical pathways of behaviourally relevant connections. When necessary (e.g. in tumour surgery) this could help a neurosurgeon prioritise regions or pathways that should ideally be preserved, by knowing which paths joined important co-activated regions.

Until recently, activation-based tractography has been hindered by two technical limitations:

1. Deterministic tractography algorithms, which become unreliable in voxels with multi-directional fibres (see Section 3.1.4). This makes the determining of fibre tracts between two small regions problematic, especially if they are a long way apart and have crossing fibres anywhere on the path between them.

2. Low-field scanners (1.5T or less) make it difficult to confidently identify the actual regions of activation/deactivation amidst the noise in the signal. For the resulting tractography to represent meaningful connectivity between two regions activated, for example, by memory stimuli requires that the seed and terminal regions selected are accurate.

The advent of second-generation tractography algorithms (see Section 3.1.4) and 3T scanners has helped overcome these difficulties, and DTI/fMRI connectivity studies are starting to appear in the literature. This combination of fMRI and DTI is expected to increase our understanding of the functional neuroanatomy underlying many of the cognitive functions in humans (Takahashi, et al. 2007). It has been used to study the linking of anatomical changes in the brain with cognitive development in the maturing adult (Durston and Casey 2006), and in the assessment of visual system abnormalities in preterm infants (Raafat, et al. 2007).

The importance of using functionally identified seed regions for tractography rather than anatomical ROIs is starting to be reported in the literature. Studies to date have covered fibre tracking around lesions (Schonberg, et al. 2006; Shinoura, et al. 2005), connectivity in the motor cortex (Cherubini, et al. 2007; Guye, et al. 2003), and connectivity of the visual system (Toosy, et al. 2004).

A recent connectivity study used a combination of fMRI and DTI to investigate the pathways connecting long-term memory-related areas identified using a word/non-word memory paradigm (Takahashi, et al. 2007). They wanted to discover whether the connection was a serial one (where A is connected to B which is connected to C) or a parallel one (where A and B are both connected to C). They drew conclusions based on the pooled results from 20 subjects, regarding tracts as being reliable if they were common to more than half the subjects. They found two fronto-temporal anatomical pathways between functionally defined memory-related areas, suggesting the specific functional relevance of the direct interaction between the dorsolateral prefrontal cortex and the temporal cortex.

As far as I am aware, mine is the first study to use fMRI to identify seed points from a working memory paradigm and then use DTI to investigate the fibre tract connectivity between these regions.

Working memory is an important cognitive process or set of processes used to temporarily hold, manipulate and mentally update current information in one's "mind". The *n*-back paradigm is commonly used in fMRI cognitive neuroscience literature and is known to provide reliable sites of brain activation to identify regions involved in working memory (Gevins and Cutillo 1993; Owen, et al. 2005). In a 2-back task, for example, the volunteer is asked to monitor a series of stimuli and to respond whenever a stimulus is presented that is the same as the one presented 2 trials previously (see Figure 7.1). A review of 5 primary studies using *n*-back paradigms with visual, non-verbal stimuli found that the prefrontal, premotor, and posterior parietal cortex regions were consistently activated (Owen, et al. 2005). Furthermore, an important finding from this review was that, "Although the importance of frontal and parietal regions in working memory is largely undisputed, no consensus has yet been reached regarding the fractionation of functions across these regions" (Owen, et al. 2005). Activation-based tractography could make an important contribution to this question,

by identifying credible sub-regions as seed/target regions for tractography across different variants (verbal/non-verbal; spatial/non-spatial) of the *n*-back task.

Although it may initially seem unexpected to find areas that are less activated during the performance of a more demanding task (e.g. a 2-back compared with 0-back memory task), there is growing interest in identifying regions of deactivation during a given task compared to rest (Greicius, et al. 2003; Gusnard and Raichle 2001; Mazoyer, et al. 2001; McKiernan, et al. 2003; Raichle, et al. 2001; Shulman, et al. 1997). Often these regions have a high resting state metabolism (Greicius, et al. 2003), and are thought to be engaged in self-referential activities when the brain is otherwise "at rest". The concept of a specific network of brain regions being active when we are at rest is often referred to as the "default mode network" (Fransson 2005; Rombouts, et al. 2005). Its activities include:

- monitoring the environmental (Gusnard and Raichle 2001)
- reviewing past knowledge (Rombouts, et al. 2005)
- planning of future behaviours (Binder, et al. 1999).

Such activities might be suspended during the performance of an active task, with a reallocation of processing resources to areas involved in the active task (McKiernan, et al. 2003). This would result in the regions involved in the self-referencing activities becoming "de-activated" during the performance of the active task.

Recent studies involving working memory have shown regions of deactivation. The following are relevant to my thesis, showing the possible role a better understanding of deactivation could have in identifying and treating degenerative neuropsychological diseases, and in identifying and monitoring TBI:

- Schizophrenia patients (Walter, et al. 2007). This study found less activation in frontoparietal and subcortical regions and a lack of deactivation of the superior temporal cortex in the patient group compared to the healthy controls.

- Alzheimer's disease (Rombouts, et al. 2005). This study suggested that altered activity in the default mode network may act as an early marker for AD pathology.

- TBI (Newsome, et al. 2007). In the 0- versus 2-back task they found the TBI patients did not show deactivation during a working memory task, while the control group did.

7.2 Subjects and Methods

The single subject in this study was a normal, healthy, young adult male volunteer. An advantage of having a single subject is that, unlike the head injury and Parkinson's disease studies presented earlier in this thesis, no spatial normalisation of the brain is required. A disadvantage is that few, if any, generalizations can be made from a single subject. At best, therefore, this study aimed to investigate the feasibility of a fuller connectivity study using *n*-back fMRI and DTI data in tandem.

Diffusion tensor MRI data were acquired using a GE 3T HDx scanner using an 8-channel brain receive coil, and a single shot 2D spin echo EPI acquisition with TE/TR = 76 ms/13 s and ASSET acceleration factor of 2. Data were acquired axially with a matrix of 128 × 128 × 49 covering a field of view of 240 mm × 240 mm × 147 mm, with 28 uniformly distributed gradient directions, with a *b*-value of 1000 s/mm^2, and 4 acquisitions with no diffusion weighting.

The *n*-back functional paradigm was used to investigate working memory (Braver, et al. 1997; Cohen, et al. 1997). This is shown schematically in Figure 7.1 (Nystrom, et al. 2000). The study used a block design with 6 runs, each of 3 minutes. The stimuli comprised fragmented uppercase letters, with a pseudo-random 70% of any letter visible, as an alternative to using both upper and lower cases when the general characteristic of the visual stimulus would change in size. The sequence of each 3-minute run was:

1. 6 second instruction
2. 18 letters for 0-Back (1 second presentation of each letter; 2.5 second pause for response), with 5 targets
3. 30 second fixation
4. second instruction
5. 18 letters for 2-Back (1 second presentation of each letter; 2.5 second pause for response), with 5 targets
6. 30 second fixation

Regions of relative activation and deactivation were identified from the fMRI data, and these were manually transferred to in-house software (Watts, et al. 2003) similar to that of the standard tractography package *DTI Studio* (Jiang, et al. 2006). Although this used first generation deterministic tractography (see Section 3.1.4), it was hoped that the advantages of 3T scanning would make region-to-region tracking possible.

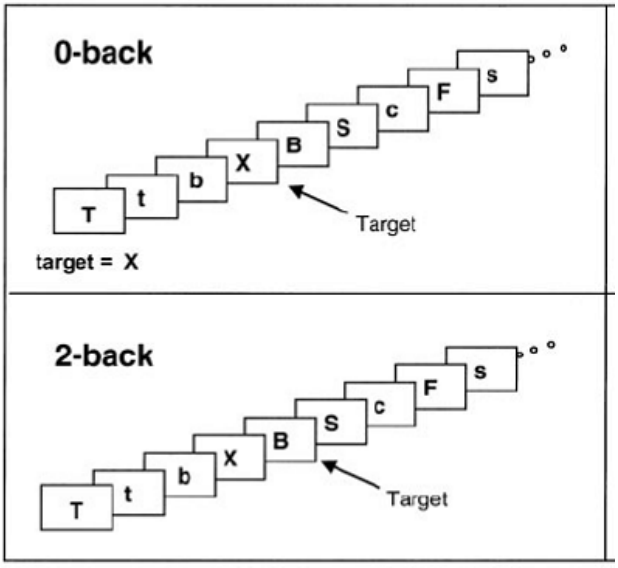

Figure 7.1 Trial schematic of *n*-back task conditions. Note that the sequence of stimuli may be identical between conditions, while the target changes by condition. In the 0-back conditions, subjects respond to a single pre-specified target (such as X) and thus do not require working memory. In the 2-back conditions, the target was any letter identical to the one presented 2 trials previously, thus requiring temporary storage and then updating of recent information. The general instruction was: "Is any currently shown letter a target?"

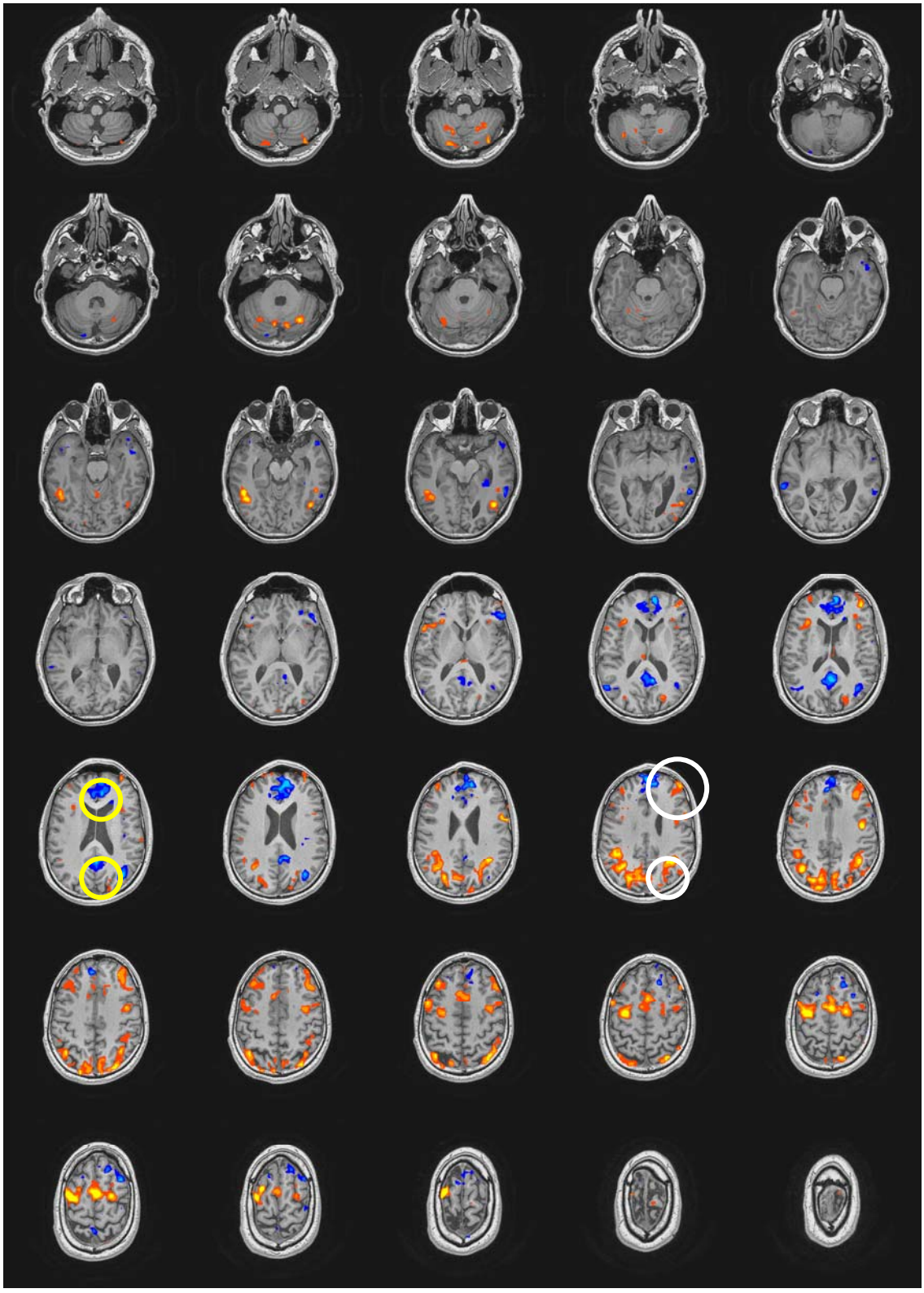

Figure 7.2 Activations (yellow/orange) and deactivations (blue) for 2-back versus 0-back. Regions selected for connectivity study are circled in yellow (deactivation) and white (activation). (t-statistic colour code : Red 5<t<6.5; orange 6.5<t<8; yellow t>8. Blue -5>t>-6.5; light blue -6.5>t>-8; teal t<-8.)

7.3 Results

Figure 7.2 shows the regions of activation and deactivation that occurred during the 2-back task compared with the 0-back task. A high *t*-threshold was chosen (5 and -5) in order to give confidence in the regions identified as activated and deactivated.

While these investigations searched for direct connections between the selected regions, it is feasible that they might be indirectly linked through a common third region. However, the results obtained when these secondary connection possibilities were investigated did not reveal any such architecture. This investigation was done by labelling each region as a seed, then observing whether the plethora of fibre bundles from each seed met at a common point. However, this finding cannot be used to conclude that such connections do not exist. The failure to identify any could simply be a result of the tractography methodology's lack of robustness to voxels with multi-directional fibres. Absence of evidence in this situation is not evidence of absence.

7.3.1 Activations

Activations were observed in several regions including, as expected, the dorsolateral prefrontal cortex and the posterior dorsal parietal cortex (circled white in Figure 7.2). These regions agree with the findings of similar studies discussed in the introduction to this chapter. They were therefore selected as the most reliable regions for this study, and used as the seed/terminal points for tractography.

It is known that the superior longitudinal fasciculus (SLF) provides a major connection between the prefrontal cortex and the posterior parietal cortex (Stuss and Knight 2002). My results in Figure 7.3 show evidence of both SLF I and SLF II tracts. While these bundles do not appear to be particularly robust, it should be remembered that with this methodology, voxels with crossing fibres will have terminated the fibre tracking even when tracts are strongly present. With the SLF likely to pass through fibre-dense sections of the brain near the corpus collosum, such a possibility is likely to have happened on several occasions.

7.3.2 Deactivations

As well as the regions of activation, of particular interest in these results are two main regions of deactivation (shown in blue in Figure 7.2).

Our study used a 2-back versus 0-back contrast rather then a memory task against rest. This was done to exclude non-memory related activity such as vision and motor from the observed activation (see Section 3.3.3). However, the 0-back task is regarded as a suitable control condition in the *n*-back paradigm (Owen, et al. 2005). The observation in this study that the two main areas of deactivation are in the medial prefrontal cortex/anterior cingulate and the posterior cingulate/ retrosplenial cortex was expected from previous studies. However, the medial parietal cortex (precuneus) that has been found to be deactivated in other studies (Rombouts, et al. 2005) was not found to be deactivated during the *n*-back task with this participant. The two identified regions in this study were therefore regarded as reliable seed/terminal regions for tractography, and results are shown in Figure 7.4. This shows fibres of the cingulum bundle joining the two regions, which is consistent with the literature (Stuss and Knight 2002).

7.4 ***Discussion***

Both the main activation and deactivation areas identified in this study compare well with those found in other similar studies. The high *t* threshold used ensured strong, positive regions were identified. The activated and deactivated regions used for tractography were consistent with the literature.

Deactivation studies have shown that the precuneus and surrounding dorsal posteromedial areas show some of the highest resting metabolic rates (Cavanna and Trimble 2006). Interestingly, we did not find any deactivation in those areas in this study. Possible explanations include:

- This subject, during this scan, used just as many processing resources in these areas during the 2-back as the 0-back task.
- The 0-back task may itself have already de-activated these areas compared to the rest state. Then, no further deactivation would be expected with 2-back compared with 0-back.
- The working memory task did not de-activate the precuneus.

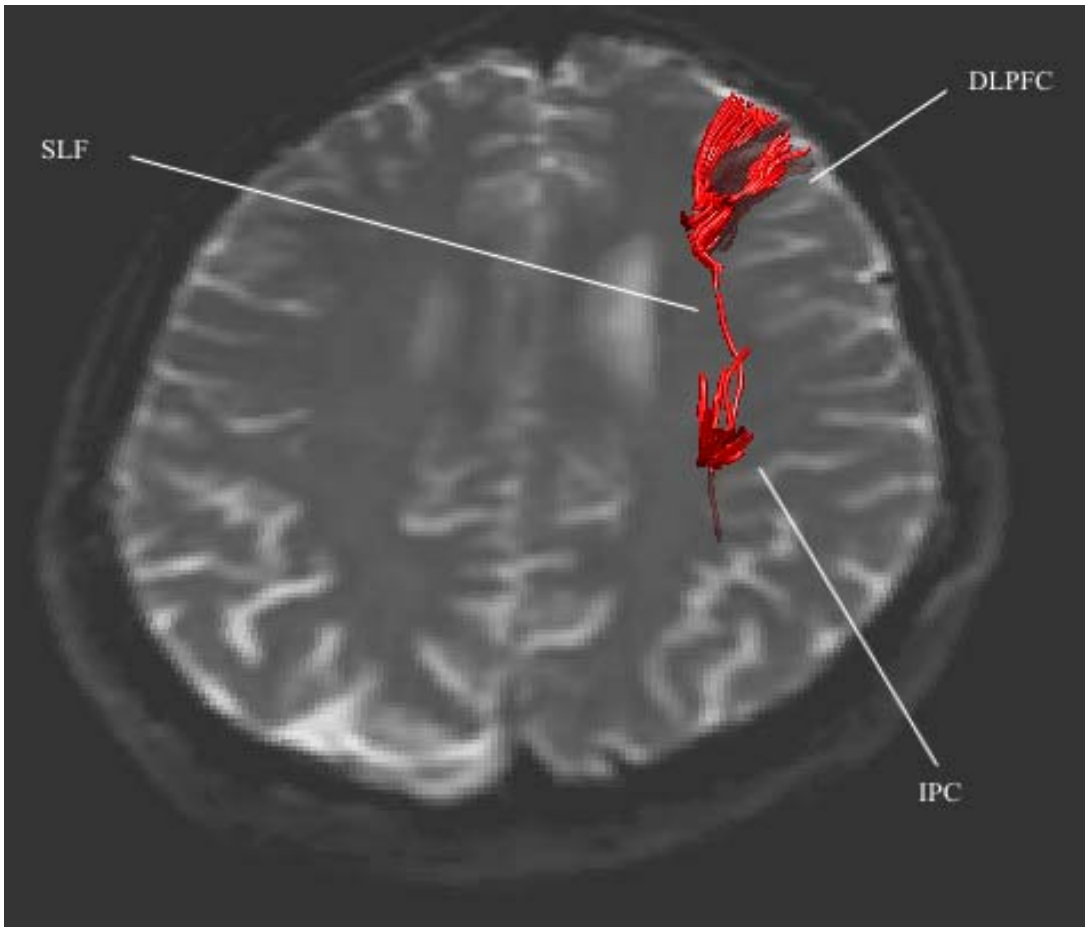

Figure 7.3 Fibre tracking between regions of activation in a 2-back v 0-back memory task. Regions are the dorsolateral prefrontal cortex (DLPFC) and the inferior parietal cortex (IPC) with the superior longitudinal fasciculus tract (SLF) connecting them.

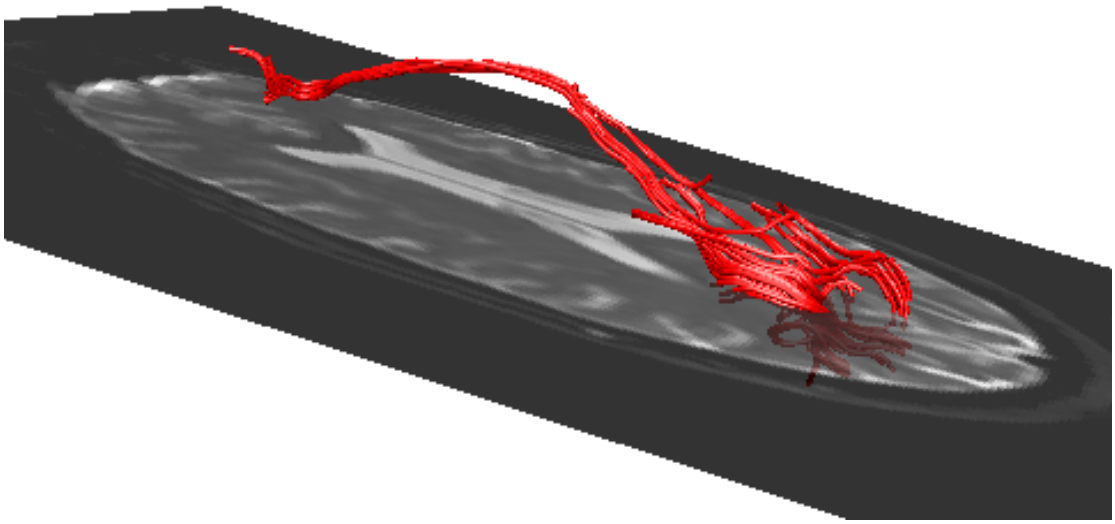

Figure 7.4 Fibre tracking between regions of deactivation in a 2-back v 0-back memory task showing the cingulum bundle.

A similar fMRI working memory study reached different conclusions (Rombouts, et al. 2005). Their study included testing 41 healthy elderly controls using 0-, 1- and 2-letter back tasks. They found deactivation in the precuneus of these subjects for both the 1- and 2-back versus 0-back contrasts. However, there are three differences between their study and ours which caution against a direct comparison and therefore concluding the results are contradictory:

- While their study was of elderly subjects, ours was of a young adult. Aging is associated with altered patterns of deactivation (Persson, et al. 2007). Persson et al. found though, that deactivation was greater in the younger subjects. So age alone may not explain the difference between Rombouts et al. and our results.

- Rombouts et al. presented the averaged deactivation of 41 healthy elderly control subjects. We are not told whether every subject displayed significant deactivation in the precuneus.

- In their stimulus paradigm Rombouts et al. showed a letter for 1 second then had a 1 second pause before showing the next. We showed a letter for 1 second, and then followed this with a 2.5 second pause (Section 7.2). Whether a longer delay time would reduce the deactivation in the precuneus in a young, healthy subject – perhaps giving sufficient time for the brain to be returning to its default state - is open to conjecture. Further study is needed.

Thus the observation that our single subject did not show deactivation in the precuneus does not support other similar findings in the literature, but nor can we say it contradicts them.

In summary, some evidence has been presented of connectivity between the activated regions, and between the de-activated regions, while no evidence for activation – deactivation connectivity was found. The tractography results suffer from the limitations of the methodology but the results, while not being conclusive in establishing significant connectivity between any of the memory-related regions of this subject's brain, are at least consistent with what was expected. Given the limitations of deterministic tractography, especially with the distance between some of the regions, there is sufficient evidence to suggest that a full connectivity study of memory using *n*-back paradigms and fMRI/DTI data with more sophisticated tractography software

could provide positive results. This approach could well be used in the future both as a diagnostic tool for degenerative diseases, and as a surgeon's guide with a particular patient undergoing tumour surgery for example.

8 Summary and Recommendations

8.1 Summary of Contributions

The flexibility of diffusion tensor imaging as an MRI modality has been exploited in three different ways in this study. Firstly its sensitivity to microstructural changes in the brain was used to identify regions of damage suffered by professional boxers and, potentially, others who receive repeated non-severe blows to the head. Secondly, the suitability of diffusion measures as biomarkers of cognitive decline in Parkinson's disease was investigated. Thirdly, the fibre tracking capability of DTI was used in conjunction with functional MRI data to investigate connectivity architecture related to memory.

8.1.1 Repetitive, non-severe head injuries

Using this unique data set, I have shown that repetitive, non-severe head impacts can be associated with brain abnormalities in many structures throughout the brain. This is an important finding, as the effects of this type of injury have not been reported in the literature. It is a field that is hard to obtain data from, since subjects with this condition are non-symptomatic and therefore hard to identify. It is ethically inadmissable to perform experiments on humans to achieve the condition, so the data and results presented here are important for furthering the understanding of mild closed head injury. Conclusive evidence of diffuse brain abnormalities in this group of professional boxers could have important implications for the protective clothing and brain monitoring of athletes involved in contact sports such as ice hockey, gridiron, Australian rules football, rugby league, rugby union, and association football.

8.1.2 Diffusion bio-markers of cognitive decline in PD

This is the first investigation of such bio-markers. The evidence presented here, though not conclusive because of the small sample size, nevertheless suggests that *MD*, or better still, the multiple regressor from all three diffusion metrics, could prove to track cognitive decline and thus be suitable bio-markers. This would then allow the localization of structural changes that are linked to cognitive decline. It would also be an important addition to the diagnostic and monitoring toolkit for Parkinson's disease.

8.1.3 Multivariate analysis

The use of Hotelling's test and multivariate regression in voxel based analysis of neuroimaging data are novel. Both showed increased sensitivity compared with the best univariate analysis. Linear discriminant analysis was used in a completely new way in this study, to form a new metric for group comparisons. This showed greatly improved sensitivity, and with the data used here, LDA identified many more regions of abnormality than the best single metric. An important development here was the formation of a new diffusion metric, the "linear combination" metric which incorporated information from all three component metrics. The methodology developed for the boxer study would be equally applicable to other studies, for example a PD study with a patient group and a subject group. The linear combination metric could prove to be a valuable bio-marker of brain damage.

8.1.4 Memory connectivity

Evidence of direct connectivity between regions activated in a 2-back v 0-back memory task has been presented. This is consistent with the literature, and combines functionally-seeded tractography with a working memory study. This, to my knowledge, has not been done before. The results are necessarily preliminary, but would support further work in this area.

Similarly, there is evidence of connectivity between deactivated regions in the same memory paradigm, which is again consistent with the literature. With the recent interest in deactivations, this could prove a profitable area of research in the future.

No evidence was found of indirect connectivity via a common third region.

8.2 Recommendations for Future Work

8.2.1 Chronic head injury

The results presented here would be enhanced with more information about the boxing history of the subjects. Data that could impact head injury such as the number of fights, number of knock-outs, and whether the boxer receives more blows to one side of the

head than the other, could be instructive. Analysis of covariance and linear discriminant analysis could both incorporate this information in their analyses.

8.2.2 Parkinson's disease

The results presented here would be enhanced by the inclusion of a control group, and the conducting of a longitudinal study. The former would allow a single multivariate diffusion measure to be formed (the linear combination), which could then be tested as a bio-marker. A longitudinal study would give a more direct indication of cognitive decline and the diffusion measures' ability to track it.

8.2.3 Working memory tractography

With the possibility and value of functionally-seeded working memory tractography established in this study, the next step is to use improved tractography technology (see below) and to study a group of subjects. This group should include those with and those without working memory impairment.

8.2.4 Linear discriminant analysis

In this study the use of the LDA metric was shown to greatly increase the sensitivity of the analysis. The logical next step is to include non-diffusion measures such as the number of years of boxing for each subject in the LDA. The great strength of LDA is that these measures, even if they contribute little to identifying abnormalities in the boxers, will not penalize the strong identifiers such as MD. Also, LDA should be applied to a different group altogether (such as PD). That will help establish whether or not it has general applicability in the field of neuroimaging.

LDA was shown to be able to identify a subject as a boxer or a control with a 90% success rate. This was done using data from a single voxel. Voxel-based predictions are not ideal, since there are far too many voxels to check individually, yet to rely on the finding of a single voxel would be unwise. Regional or whole-brain LDA prediction methods need to be investigated. One overall result is needed, but it should be based on as much data as possible.

8.2.5 Smoothing filter

Diffuse axonal injury associated with traumatic brain injury tends to be more on the scale of a voxel than several voxels. The findings presented in this work, particularly

from the linear discriminant analysis, support extending this to non-severe head injury. If this is the case, then further research is needed on the most appropriate processing parameters to use for these data. In particular, effects of the size of the smoothing filter on the results needs investigation. It is possible that the 8 mm FWHM filter used in this study, though acceptable in general to the research community, may have resulted in the non-detection of many small abnormalities. A smaller filter, or even no smoothing at all, might provide more detailed results than are shown in this study. The risk of reducing the filter size is two-fold: a reduction in SNR, and the loss of Gaussianity needed in random field theory compensations for multiple comparisons. The former may or may not be critical – further investigation is needed there. The latter could be circumvented by using false discovery rate corrections for multiple comparisons, or by using Bayesian statistics rather than standard hypothesis testing.

The scale of the microstructural damage causing cognitive decline in Parkinson's disease is even less well understood than with head injury. This renders a full investigation of the effects of filter size on these data potentially very rewarding and significant.

8.2.6 High resolution DTI

While whole-brain high spatial resolution DTI data is not practicable, obtaining high resolution images of specific regions in Parkinson's patients could be worthwhile. Indeed, if the mechanisms that make Parkinson's disease similar to, and differentiate it from Alzheimer's disease are to be understood, this could make a significant contribution. Regions such as the hippocampus and the caudate nucleus could benefit greatly from higher resolution studies.

The rather ambiguous correlation data between diffusion metrics and age in the cerebellum of the boxers needs further study. Higher resolution imaging, having less partial volume effect, might make an important contribution to this study.

8.2.7 Use of Bayesian Statistics

Conventional frequentist statistics in neuroimaging analysis suffers from two important drawbacks: the problem of multiple comparisons, and the reliance of the results on an arbitrary *p*-value threshold. Both of these problems are overcome by using Bayesian statistics, which are also more sensitive than frequentist analyses at conventional *p*-

values. These approaches are available in several of the main neuroimage processing software packages. The computing time is longer, though not prohibitively so.

8.2.8 Non-Euclidean tensor analysis

With directional information from the tensor being such an important part of its contents, particularly in fibre tracking, using analysis methods that do not compromise this is paramount. Riemannian analysis keeps tensors intact under transformations such as spatial normalisation, in contrast to the present approach of extracting scalar derivatives of the tensor and comparing these. Riemannian analysis also allows the averaging of tensors which will make possible grouped fibre tracking rather than the present individual approach.

8.2.9 Probabilistic tractography

Standard Euclidean tensor analysis can provide important tractography information, especially for single subjects. The results presented in Chapter 7 suggest the use of a more sophisticated tractography algorithm could be worthwhile in investigating memory connectivity.

APPENDIX I: PUBLICATIONS AND PRESENTATIONS

The following publications and presentations have ensued from the research presented in this thesis.

Publications

Michael H. Chappell, Jennifer A.Brown, John C. Dalrymple-Alford, Aziz M. Uluğ, Richard Watts.: Multivariate approaches increase the sensitivity of diffusion tensor imaging voxel-based analysis: cortical and subcortical microstuctural damage in young professional boxers. (Under review.)

Michael Chappell, Timothy Anderson, Jennifer Brown, John Dalrymple-Alford, Marcus Heitger, Saskia van Stockum, Richard Watts. Using MRI to identify Microstructural Changes in the Brain. The New Zealand Medical Journal Vol 119 No 1245 (17 November 2006), http://www.nzma.org.nz/journal/119-1245/2330/. Proceedings of Health Research Society of Canterbury's Scientific Meeting, Wednesday 1 November 2006

Michael H. Chappell, Aziz M. Uluğ, Lijuan Zhang, Marcus H. Heitger, Barry D. Jordan, Robert D. Zimmerman, Richard Watts: Distribution of microstructural damage in the brains of professional boxers: A diffusion MRI study. Journal of Magnetic Resonance Imaging, 24(3) (Sept 2006): 537-542 (Published Online: 28 Jul 2006.)

M. H. Chappell, T. J. Anderson, J. C. Dalrymple-Alford, S. van Stockum, R. Watts: Cognitive Impairment in Parkinson's Disease: Preliminary DTI Findings. Proc. Intl. Soc. Mag. Reson. Med. 14 (2006) 3416

Michael H. Chappell, Aziz M. Uluğ, Lijuan Zhang, Marcus H. Heitger, Barry D. Jordan, Robert D. Zimmerman, Richard Watts: Distribution of microstructural damage in the brains of professional boxers: A diffusion MRI study. Proc. Intl. Soc. Mag. Reson. Med. 13 (2005) 1385

Michael H. Chappell and Richard Watts. Fibre Tracking and Localising Brain Injury with MRI. Proceedings of the 23rd International Australasian Winter Conference on Brain Research 2005, Volume 23

Presentations

Oral presentation at the Organization for Human Brain Mapping (HBM) 13th Annual Meeting in Chicago, USA, June 2007. Using diffusion tensor imaging parameters as markers of cognitive decline with Parkinson's disease. Michael H. Chappell, Timothy J. Anderson, John C. Dalrymple-Alford, Saskia van Stockum, Richard Watts.

Oral e-poster presentation at the International Society for Magnetic Resonance in Medicine (ISMRM) 15th Scientific Meeting in Berlin, Germany, May 2007. Multivariate Linear Discriminant Analysis of DTI Data Improves the Detection of Microstructural Damage in Young Professional Boxers. Michael H. Chappell, Jennifer A. Brown, John C. Dalrymple-Alford, Aziz M. Uluğ, Richard Watts.

Oral presentation at the Christchurch School of Medicine and Health Sciences, Christchurch, New Zealand, 1 November 2006. Using MRI to identify Microstructural Changes in the Brain. Michael Chappell, Timothy Anderson, Jennifer Brown, John Dalrymple-Alford, Marcus Heitger, Saskia van Stockum, Richard Watts.

Oral presentation at the University of Canterbury Postgraduate Showcase '06 Conference, Christchurch, New Zealand, 18 October 2006. MRI Brain Imaging. Michael Chappell, Richard Watts, Jennifer Brown, John Dalrymple-Alford.

Poster presentation at the Organization for Human Brain Mapping (HBM) 12th Annual Meeting in Florence, Italy, June 2006. Using Orthogonal Metrics from the Diffusion Tensor in Conjunction, Disjunction and Linear Discriminant Analyses. M.H. Chappell, J.Brown, A. M. Uluğ, R. Watts.

E-poster presentation at the International Society for Magnetic Resonance in Medicine (ISMRM) 14th Scientific Meeting in Seattle, USA, May 2006. Cognitive impairment in Parkinson's disease: Preliminary DTI findings. Chappell MH, Anderson TJ, Dalrymple-Alford JC, van Stockum S, Watts R.

Oral presentation at the Van der Veer Institute for Parkinson's & Brain Research (VDVI) Brain Research Forum in Christchurch, NZ, March 2006. Cognitive Impairment in Parkinson's Disease: Preliminary DTI Findings

Oral presentation at the 23rd International Australasian Winter Conference on Brain Research (AWCBR) in Queenstown, NZ, August 2005. Fibre Tracking and Localising Brain Injury with MRI

Poster presentation at the International Society for Magnetic Resonance in Medicine (ISMRM) 13th Scientific Meeting in Miami, USA, May 2005. Distribution of Microstructural Damage in the Brains of Professional Boxers: A Diffusion MRI Study. M. Chappell, A.M. Ulug, L. Zhang, M. Heitger, B. Jordan, R.D. Zimmerman, R. Watts

Oral presentation at the New Zealand Physics and Engineering in Medicine (NZPEM) conference in Christchurch, NZ, November 2004. MRI Imaging of the Brain – A Boxer Study

APPENDIX II: MATLAB CODE

Linear Discriminant Analysis

Boxers59_FLD_Pt1.m

```
%This program creates data vectors from the 59 boxer data, restricted
%to the controls' age range, ready for Fisher Linear Discriminant
%Analysis in Boxers59_FLD_Pt2.m

%Get data from /home/mhc15/boxer_metrics/smooth4

%clear all ;
 warning off MATLAB:nonIntegerTruncatedInConversionToChar;

c1=fix(clock) ;
fprintf('\nJob started at %d:%d ...\n', c1(4), c1(5));
subjects = [14288  14360  15520  15552  15575  15582  15604  15780
15782  15919  16173  16212  16272  16284  16300  16351  16478  16686
16696  16712  16719  16728  16753  17169  17264  17282  17283  17284
17579  17604  17709  17713  17714  17731  17754  17779 17783  17796
17815  17827  18175  18180  18201  18491  18581  18619  18767  18768
18807  18821  17648  17649  18261  18263 18831  18921  18922  18938
21344  13887  13941  13958  13960  14009  14210  14211  18774  18007
17782  17820  18772] ;
% INPUT NUMBER OF METRICS BEING USED
met = 3 ;

n1= 59 ; % NUMBER OF BOXERS
n2= 12 ; % NUMBER OF CONTROLS
sub = n1+n2 ;
group = [ones(1,n1) ones(1,n2)+1] ;


% SET UP THE STRUCTURE
voxel=struct('data' , zeros(met,sub) ) ;

            FAdata=zeros(79,95,69);
            Davdata=zeros(79,95,69);
            MODEdata=zeros(79,95,69);

            for p=1:sub
                fprintf('\nProcessing subject %d ...', subjects(p)) ;
                wFA = sprintf('/home/mhc15/boxer_metrics/smooth4/
                                          sw%d_FA.img', subjects(p)) ;
                wDav = sprintf('/home/mhc15/boxer_metrics/smooth4/
                                         sw%d_Dav.img', subjects(p)) ;
                wMODE = sprintf('/home/mhc15/boxer_metrics/smooth4/
                                         sw%d_MODE.img', subjects(p));
                fidFA = fopen(wFA, 'r', 'ieee-le');
                fidDav = fopen(wDav, 'r', 'ieee-le');
                fidMODE = fopen(wMODE, 'r', 'ieee-le');

                for i=1:69
                    FAdata(:,:,i) = fread(fidFA, [79,95], 'float32');
                    Davdata(:,:,i)= fread(fidDav, [79,95], 'float32');
```

```
                    MODEdata(:,:,i)=fread(fidMODE, [79,95],'float32');
                end

                fclose(fidFA);
                fclose(fidDav);
                fclose(fidMODE);

                Davvec(p,:)=reshape(Davdata,1,[]);
                FAvec(p,:)=reshape(FAdata,1,[]);
                MODEvec(p,:)=reshape(MODEdata,1,[]);
            end


save FLD_box59.mat Davvec FAvec MODEvec;
c2=fix(clock) ;

fprintf('\nJob finished at %d:%d ...\n', c2(4), c2(5));
if c2(5)>= c1(5)
    mins=c2(5)-c1(5) ;
    hrs=c2(4)-c1(4) ;
else
    mins=60+c2(5)-c1(5);
    hrs=c2(4)-c1(4)-1 ;
end
fprintf('\nTime taken:  %d hours %d mins\n', hrs, mins);
```

Boxers59_FLD_Pt2.m

```
%This is the second of 3 programs to produce FLD images from
%multimetric data. This program converts smoothed, spatially
%normalised data into FLDs. The first, which creates the data vectors
%for this one, is Boxers59_FLD_Pt1.m. The data from this program can
%be used in Boxers59_FLD_Pt3.m to evaluate the FD Linear Combination
%at each voxel.
fclose('all');
clear all ;

% INPUT NUMBER OF METRICS BEING USED
met =3 ;

n1= 59 ; % NUMBER OF BOXERS
n2= 12 ; % NUMBER OF CONTROLS
sub = n1+n2 ;
group = [ones(1,n1) ones(1,n2)+1] ;

c1=fix(clock) ;
fprintf('\nJob started at %d:%d ...\n', c1(4), c1(5));

                suc=zeros(79,95,69) ;
                Davco=[0] ;
                FAco=[0] ;
                MODEco=[0] ;
                sp=[0] ;
                sc=[0] ;
                LC=zeros(79,95,69) ;
                FAcoeff=zeros(79,95,69) ;
                Davcoeff=zeros(79,95,69) ;
                MODEcoeff=zeros(79,95,69) ;
                const=zeros(79,95,69) ;

                fprintf('\nOpening the FLD_results.mat file ...\n');
                open FLD_box59.mat ;
                Davvec=ans.Davvec;
                FAvec=ans.FAvec;
                MODEvec=ans.MODEvec;
                fprintf('\nFile successfully opened and metric vectors
                                                        assigned \n');
                v=0 ;

                % Call the fisher function to do FLD on each voxel
                fprintf('Starting the voxel-by-voxel linear
                                            discriminant analysis\n');
                for z=1:69
                    for y=1:95
                        for x=1:79
                            v=v+1 ;
                            indat = [Davvec(:,v) FAvec(:,v)
MODEvec(:,v)] ;

                            if  min(min(abs(indat(1:2,:) )))>0 ;
%Don't process voxels with main metrics zero
                                [discrim, successrate ] =
                                       fisher(zscore(indat)', group, met,
                                                        sub, n1, n2) ;
                                suc(x,y,z)=successrate ;
```

```
                                FAcoeff(x,y,z)=discrim.W(2) ;
                                Davcoeff(x,y,z)= discrim.W(1) ;
                                MODEcoeff(x,y,z)= discrim.W(3) ;
                                const(x,y,z)= discrim.b;

                            end
                        end
                    end
                end


filesuc = fopen(     ['/home/mhc15/boxer_metrics/smooth4/LC/suc.img'],
'wb', 'ieee-le') ;
fileFAcoeff = fopen( ['/home/mhc15/boxer_metrics/smooth4/
                                        LC/FAcoeff.img'], 'wb','ieee-le');
fileDavcoeff =fopen( ['/home/mhc15/boxer_metrics/smooth4/
                                     LC/Davcoeff.img'], 'wb', 'ieee-le') ;
fileMODEcoeff =fopen(['/home/mhc15/boxer_metrics/smooth4/
                                    LC/MODEcoeff.img'], 'wb', 'ieee-le') ;
fileconst = fopen(['/home/mhc15/boxer_metrics/smooth4/LC/const.img'],
                                                        'wb', 'ieee-le') ;


fwrite(filesuc, suc, 'float32') ;
fwrite(fileFAcoeff, FAcoeff, 'float32') ;
fwrite(fileDavcoeff, Davcoeff, 'float32') ;
fwrite(fileMODEcoeff, MODEcoeff, 'float32') ;
fwrite(fileconst,const, 'float32') ;

fclose(filesuc) ;
fclose(fileFAcoeff) ;
fclose(fileDavcoeff) ;
fclose(fileMODEcoeff) ;
fclose(fileconst) ;

c2=fix(clock) ;
fprintf('\nJob finished at %d:%d ...\n', c2(4), c2(5));
if c2(5)>=c1(5)
    mins=c2(5)-c1(5) ;
    hrs=c2(4)-c1(4) ;
else
    mins=60+c2(5)-c1(5);
    hrs=c2(4)-c1(4)-1 ;
end
fprintf('\nTime taken:  %d hours %d mins\n', hrs, mins);
```

Boxers59_FLD_Pt3.m

```
%FORMS THE LINEAR COMBINATION AT EACH VOXEL, USING RESULTS OF FISHER
%LINEAR  %DISCRIMINANT FROM Boxers59_FLD_Pt2.m

fclose('all');
clear all ;
c1=fix(clock) ;
%Now input the id numbers of the controls and the patients
patients = [14288  14360  15520  15552  15575  15582  15604  15780
15782  15919  16173  16212  16272  16284  16300  16351  16478  16686
16696  16712  16719  16728  16753  17169  17264  17282  17283  17284
17579  17604  17709  17713  17714  17731  17754  17779 17783  17796
17815  17827  18175  18180  18201  18491  18581  18619  18767  18768
18807  18821  17648  17649  18261  18263 18831  18921  18922  18938
21344] ;

controls = [13887  13941  13958  13960  14009  14210  14211 18774
18007 17782 17820 18772] ;

    FAdata=zeros(79,95,69);
    Davdata=zeros(79,95,69);
    MODEdata=zeros(79,95,69);
    LinComb=zeros(79,95,69);

%Form the coefficient images
****************************************
    FAcoeffdata=zeros(79,95,69);
    Davcoeffdata=zeros(79,95,69);
    MODEcoeffdata=zeros(79,95,69);
    constdata=zeros(79,95,69);

    FAcoeff =  sprintf('/home/mhc15/boxer_metrics/smooth4/
                                                    LC/FAcoeff.img');
    Davcoeff = sprintf('/home/mhc15/boxer_metrics/smooth4/
                                                   LC/Davcoeff.img');
    MODEcoeff =sprintf('/home/mhc15/boxer_metrics/smooth4/
                                                  LC/MODEcoeff.img');
    const =    sprintf('/home/mhc15/boxer_metrics/smooth4/
                                                     LC/const.img');

    fidFAcoeff = fopen(FAcoeff, 'r', 'ieee-le');
    fidDavcoeff = fopen(Davcoeff, 'r', 'ieee-le');
    fidMODEcoeff = fopen(MODEcoeff, 'r', 'ieee-le');
    fidconst = fopen(const, 'r', 'ieee-le');
   for i=1:69
       FAcoeffdata(:,:,i) = fread(fidFAcoeff, [79,95], 'float32');
       Davcoeffdata(:,:,i) = fread(fidDavcoeff, [79,95], 'float32');
       MODEcoeffdata(:,:,i)= fread(fidMODEcoeff, [79,95], 'float32');
       constdata(:,:,i) = fread(fidconst, [79,95], 'float32');
   end

        fclose(fidFAcoeff);
        fclose(fidDavcoeff);
        fclose(fidMODEcoeff);
        fclose(fidconst);

        %Change the 3D images into vectors
        FAc=reshape(FAcoeffdata,79*95*69,1);
```

```
    Davc=reshape(Davcoeffdata,79*95*69,1) ;
    MODEc=reshape(MODEcoeffdata,79*95*69,1) ;
    c=reshape(constdata,79*95*69,1);

for p=1:size(patients,2)
    fprintf('Processing patient %d\n', patients(p)) ;

    swFA =  sprintf('/home/mhc15/boxer_metrics/smooth4/
                                          sw%d_FA.img', patients(p));
    swDav = sprintf('/home/mhc15/boxer_metrics/smooth4/
                                         sw%d_Dav.img', patients(p));
    swMODE= sprintf('/home/mhc15/boxer_metrics/smooth4/
                                        sw%d_MODE.img', patients(p));

    fidFA = fopen(swFA, 'r', 'ieee-le');
    fidDav = fopen(swDav, 'r', 'ieee-le');
    fidMODE = fopen(swMODE, 'r', 'ieee-le');

    for i=1:69
        FAdata(:,:,i) = fread(fidFA, [79,95], 'float32');
        Davdata(:,:,i) = fread(fidDav, [79,95], 'float32');
        MODEdata(:,:,i) = fread(fidMODE, [79,95], 'float32');
    end
    %Now form the new linear combination image using vectorized
                                                        normalized data
    FAv=reshape(FAdata,79*95*69,1) ;
    Davv=reshape(Davdata,79*95*69,1) ;
    MODEv=reshape(MODEdata,79*95*69,1) ;
    FAv(isnan(FAv))=0 ; %Replaces NaN with 0
    Davv(isnan(Davv))=0 ;
    MODEv(isnan(MODEv))=0 ;


    FA=zscore(FAv);
    Dav=zscore(Davv);
    MODE=zscore(MODEv);
    LC=FAc.*FA + Davc.*Dav + MODEc.*MODE + c ;
    LinComb = reshape(LC,79,95,69);
    fclose(fidFA);
    fclose(fidDav);
    fclose(fidMODE);

     outputpath1=sprintf('/home/mhc15/boxer_metrics/smooth4/sw%.5d_',
                                                        patients(p)) ;
    fileLC = fopen([outputpath1, 'LC.img'], 'wb', 'ieee-le') ;
    fwrite(fileLC, LinComb, 'float32');

end

%Repeat for controls
for p=1:size(controls,2)
    fprintf('Processing control %d\n', controls(p)) ;
    swFA = sprintf('/home/mhc15/boxer_metrics/smooth4/
                                          sw%d_FA.img', controls(p));
    swDav = sprintf('/home/mhc15/boxer_metrics/smooth4/
                                         sw%d_Dav.img', controls(p));
    swMODE = sprintf('/home/mhc15/boxer_metrics/smooth4/
                                        sw%d_MODE.img', controls(p));
```

```
        fidFA = fopen(swFA, 'r', 'ieee-le');
        fidDav = fopen(swDav, 'r', 'ieee-le');
        fidMODE = fopen(swMODE, 'r', 'ieee-le');

        for i=1:69
            FAdata(:,:,i) = fread(fidFA, [79,95], 'float32');
            Davdata(:,:,i) = fread(fidDav, [79,95], 'float32');
            MODEdata(:,:,i) = fread(fidMODE, [79,95], 'float32');
        end
        %Now form the new linear combination image using normalized    data
        FAv=reshape(FAdata,79*95*69,1) ;
        Davv=reshape(Davdata,79*95*69,1) ;
        MODEv=reshape(MODEdata,79*95*69,1) ;
        FAv(isnan(FAv))=0 ; %Replaces NaN with 0
        Davv(isnan(Davv))=0 ;
        MODEv(isnan(MODEv))=0 ;

        FA=zscore(FAv);
        Dav=zscore(Davv);
        MODE=zscore(MODEv);
        LC=FAc.*FA + Davc.*Dav + MODEc.*MODE + c ;
        LinComb = reshape(LC,79,95,69);

        fclose(fidFA);
        fclose(fidDav);
        fclose(fidMODE);

         outputpath2=sprintf('/home/mhc15/boxer_metrics/smooth4/
                                  controldata/sw%.5d_', controls(p)) ;
        fileLC2 = fopen([outputpath2, 'LC.img'], 'wb', 'ieee-le') ;
        fwrite(fileLC2, LinComb, 'float32') ;

    end



fclose(fileLC) ;
fclose(fileLC2) ;

c2=fix(clock) ;
fprintf('\nJob finished at %d:%d ...\n', c2(4), c2(5));
if c2(5)>=c1(5)
    mins=c2(5)-c1(5) ;
    hrs=c2(4)-c1(4) ;
else
    mins=60+c2(5)-c1(5);
    hrs=c2(4)-c1(4)-1 ;
end
fprintf('\nTime taken:  %d hours %d mins\n', hrs, mins);
```

Fisher.m

```
%This function performs Fisher Linear Discriminant analysis and
calculates the success rate of separation using its results.

%

% INPUTS: data must be in structure format for fld.

% 1. data must be  a 'number of different metrics' x 'number of
%    subjects' matrix.

% 2. group is a 1 x 'number of subjects' vector labelling the group
%     that each subject belongs to (usually 1 or 2)

% 3. met is the number of metrics

% 4. sub is the number of subjects

% 5. n1 and n2 are the number of subjects in group 1 and 2
     respectively

%

function [discrim, successrate] = fisher(data,group,met,sub,n1,n2)

boxer.X = data ;

boxer.y = group ;

boxer.name = 'Boxer LDA' ;

boxer.dim = met ;

boxer.num_data = sub ;


discrim=fld(boxer) ;

success=0 ;


% Enumerate the discriminant function

FLD=discrim.W'*boxer.X + discrim.b ;

for n=1:n1

    if FLD(n)>0 success=success+1 ;

    end

end

for n=n1+1:sub
```

```
    if FLD(n)<0 success=success+1 ;
    end
end
successrate=success/sub ;

return ;
```

Hotelling's T^2 Statistic

```
%DERIVES THE HOTELLING T-SQ STATISTIC AT EACH VOXEL for the Cornell
%Boxers data, READY FOR TESTING IN SPM
c=fix(clock) ;
fprintf('\nHOTELLINGS T-SQUARED PROGRAM STARTED AT %d:%d
\n\n',c(4),c(5)) ;

fclose('all');

%INPUT number of metrics being used
m=2 ;

%Now input the id numbers of the controls and the patients
patients = [14288  14360  15520  15552  15575  15582  15604  15780
15782  15919  16173  16212  16272  16284  16300  16351  16478  16686
16696  16712  16719  16728  16753  17169  17264  17282  17283  17284
17579  17604  17709  17713  17714  17731  17754  17779 17783  17796
17815  17827  18175  18180  18201  18491  18581  18619  18767  18768
18807  18821  17648  17649  18261  18263 18831  18921  18922  18938
21344] ;

controls = [13887  13941  13958  13960  14009  14210  14211 18774
18007 17782 17820 18772] ;

if m==3
    fid1 = fopen('/home/mhc15/multi-metrics_Oct06/
      Age_restricted_boxers/Hotelling/3M/3M_Tsq_59.img', 'w', 'ieee-le');
else
    fid1 = fopen('/home/mhc15/multi-metrics_Oct06/
      Age_restricted_boxers/Hotelling/2M/2M_Tsq_59.img', 'w', 'ieee-le');
end

 tempdata=zeros(79,95,69);

%START THE STRUCTURE THAT WILL HOLD THE DATA
if m==3
      data(79,95,69)=struct('Bmetrics', [0;0;0], 'Cmetrics', [0;0;0],
      'Bave', [0;0;0],  'Cave', [0;0;0], 'Tsq', 0, 'F', 0 ) ;
else
    data(79,95,69)=struct( 'Bmetrics', [0;0], 'Cmetrics', [0;0], 'Bave', [0;0],
   'Cave', [0;0], 'Tsq', 0, 'F', 0 ) ;
end

%READ DATA IN FOR EACH patient
    for p=1:size(patients,2)
        fprintf('Processing patient %d\n', patients(p)) ;
        N=readanalyze(['/home/mhc15/boxer_metrics/spm2_analysis/
            age_matched_boxerdata/sw',num2str(patients(p)), '_Dav.img']);
        F=readanalyze(['/home/mhc15/boxer_metrics/spm2_analysis/
             age_matched_boxerdata/sw',num2str(patients(p)),' _FA.img']);
        if m==3
            M=readanalyze(['/home/mhc15/boxer_metrics/spm2_analysis/
           age_matched_boxerdata/sw',num2str(patients(p)), '_MODE.img']);
            Mdata=reshape(M,79,95,69) ;
        end
        Ndata=reshape(N,79,95,69) ;
        Fdata=reshape(F,79,95,69) ;
```

```
    %NOW GO THROUGH EACH VOXEL TO FORM THE ARRAY OF ALL THE METRICS
        for x=1:79
            for y=1:95
                for z=1:69
                    if m==3
                        data(x,y,z).Bmetrics = [data(x,y,z ).Bmetrics
                             [Ndata(x,y,z); Fdata(x,y,z); Mdata(x,y,z)]];
                    else
                        data(x,y,z).Bmetrics = [data(x,y,z ).Bmetrics
                                        [Ndata(x,y,z) ; Fdata(x,y,z) ]] ;
                    end
                end
            end
        end

%NOW DO THE CONTROLS
  %READ DATA IN FOR EACH SUBJECT
        for p=1:size(controls,2)
        fprintf('Processing control %d\n', controls(p)) ;

        N=readanalyze(['/home/mhc15/boxer_metrics/spm2_analysis/
                        controldata/sw',num2str(controls(p)),'_Dav.img']);
        F=readanalyze(['/home/mhc15/boxer_metrics/spm2_analysis/
                         controldata/sw',num2str(controls(p)),'_FA.img']);

        if m==3
            M=readanalyze(['/home/mhc15/boxer_metrics/spm2_analysis/
                       controldata/sw',num2str(controls(p)),'_MODE.img']);
            Mdata=reshape(M,79,95,69) ;
        end
        Ndata=reshape(N,79,95,69) ;
        Fdata=reshape(F,79,95,69) ;

%NOW GO THROUGH EACH VOXEL TO FORM THE ARRAY OF ALL THE METRICS
        for x=1:79
            for y=1:95
                for z=1:69
                    if m==3
                        data(x,y,z).Cmetrics = [data(x,y,z ).Cmetrics
                          [Ndata(x,y,z) ; Fdata(x,y,z) ; Mdata(x,y,z)]] ;
                    else
                        data(x,y,z).Cmetrics = [data(x,y,z ).Cmetrics
                                        [Ndata(x,y,z) ; Fdata(x,y,z) ]] ;
                    end
                end
            end
        end


%Now find the stats at each voxel
c=fix(clock) ;
fprintf('\nCalculating the mean and standard deviation for each
voxel... ') ;
fprintf('\nthis takes a while, starting at %d:%d ... \n', c(4), c(5))
;
   for x=1:79
            for y=1:95
                for z=1:69
```

```
                    data(x,y,z).Bave=mean(data(x,y,z).Bmetrics, 2) ;
                    data(x,y,z).Bdev=zeros(m) ;
                    data(x,y,z).Cdev=zeros(m) ;
                    data(x,y,z).Spool=zeros(m) ;
                    data(x,y,z).Tsq=0 ;
                    data(x,y,z).F=0 ;

                  %NOW DO THE SUMMATION ACROSS patients FOR THE STD DEV
                    for s=1:size(patients,2)
                        Bsd=(data(x,y,z).Bmetrics(:,s)-data(x,y,z).Bave)*
                         (data(x,y,z).Bmetrics(:,s)- data(x,y,z).Bave)' ;
                        data(x,y,z).Bdev=data(x,y,z).Bdev + Bsd ;
                    end

                    data(x,y,z).Bdev=(1/(size(patients,2)-1))*
                                                 data(x,y,z).Bdev ;

                    data(x,y,z).Cave=mean(data(x,y,z).Cmetrics, 2) ;

                     %NOW DO THE SUMMATION ACROSS CONTROLS FOR THE STD DEV
                    for s=1:size(controls,2)
                        Csd=(data(x,y,z).Cmetrics(:,s)- data(x,y,z).Cave)*
                         (data(x,y,z).Cmetrics(:,s)- data(x,y,z).Cave)' ;
                        data(x,y,z).Cdev=data(x,y,z).Cdev + Csd ;
                    end

                    data(x,y,z).Cdev=(1/(size(patients,2)- 1))*
                                                 data(x,y,z).Cdev ;
                    data(x,y,z).Spool=((size(patients,2) - 1)*
              data(x,y,z).Bdev + (size(controls,2)- 1)*data(x,y,z).Cdev)/
                 (size(patients,2)+size(controls,2)-2) ;  %Pooled std dev
   %The singular matrix case:
                    if rcond(data(x,y,z).Spool) < 2e-15
                        data(x,y,z).Tsq = 0 ;
                     else
                        data(x,y,z).Tsq=[data(x,y,z).Bave(:,1)-
                          data(x,y,z).Cave(:,1)]'*(data(x,y,z).Spool*
                          (1/size(patients,2) +  1/size(controls,2)))^-1*
                          (data(x,y,z).Bave-data(x,y,z).Cave) ;
                    end
                        %Hotellings T-squared statistic:
                             data(x,y,z).F=((size(patients,2)+
                             size(controls,2)-m- 1)/(m*(size(patients,2)+
                             size(controls,2)-2)))*data(x,y,z).Tsq ;
                end
            end
        end

        for x=1:79
            for y=1:95
                for z=1:69
                tempdata(x,y,z)=data(x,y,z).F;
                end
            end
        end
fwrite(fid1, tempdata, 'float32');
fclose(fid1);
c=fix(clock) ;
fprintf('\nJOB FINSISHED AT %d:%d \n\n',  c(4), c(5)   ) ;
```

Simulation

```
%This program simulates DTI analysis, comparing the results with
%"ground truth" for various parameter choices.
%
%INPUT: Tensor eigenvalues
%       S0
%       b-factors
%       number of, and actual, gradients, via directional cosines
%       gx, gy, gz
%       SNR
%       Number of simulations to run
%
%The program takes this information, calculates the signal at each
%gradient, adds noise to it, then processes this in the normal way to
%find the tensor elements and derived parameters. These are then
%compared with %the known originals.

clear all ;
tstart = clock;
fprintf('\nJob started at %d:%d ...\n',tstart(4), tstart(5)) ;
%INPUT THE NUMBER OF SIMULATIONS TO PERFORM
sim=100000;
parsum=zeros(1,12) ; %The arrays for storing all the derived
parameters
parsumsq=zeros(1,12) ;

%Start the diffusion tensor, D
D=zeros(3) ;

%INPUT the tensor eigenvalues
D(1,1) = 9e-4 ;
D(2,2) = 7e-4 ;
D(3,3) = 5e-4 ;

%INPUT SNR (of B0 signal)
SNR = 12;

%INPUT S0, the no-diffusion signal (the T2 value). Else set it to 1
S0 = 500 ;

%INPUT the number of non-zero gradient directions ( select from 6-100
inclusive, 120, or 150 )
d = 26;

%INPUT B-factor
B=1000;

b = ones(1,d) ;
grad = zeros(d+1,3) ;
Strue = zeros(1,d+1) ;
Snoisy = zeros(1,d+1) ;
g=zeros(3) ;

%FORM THE B-MATRIX
 b=[0 B*b];
```

```
%b = [0 1000 1000 1000 1000 1000 1000];

%INPUT the tensor angles

%Call function GRADIENTS to return non-normalised directional cosines
for each of the directions:
grad=gradients(d) ;
grads = [0 0 0 ; grad./[sum(grad.^2,2) sum(grad.^2,2)
sum(grad.^2,2)]];

for j=1:d+1
    %Calculate the grad, g, and b matrices, and thus the signal, at
    %each gradient direction
    G=grads(j,:)' ;
    g = G*G' ;
    bmat = b(j)*g ;
    Strue(j) = S0*exp(-trace(bmat*D')) ;
end

%Find the "true" parameters++++++++++++++++++++++++++++++

    %Calculate measured signal for each gradient direction
    bD = (log(S0)-log(Strue));
    S=S0*exp(-bD);

    %Now fit the tensor ********************
    gx=grads(:,1) ;
    gy=grads(:,2) ;
    gz=grads(:,3) ;

    A=ones(d+1,7) ; % 6 tensor elements plus ln(S0)
    for i=1:d+1  %for each gradient direction
        A(i,2:7)=-b(i)*[gx(i)^2,gy(i)^2,gz(i)^2,
                            2*gx(i)*gy(i),2*gx(i)*gz(i),2*gy(i)*gz(i)];
    end
    lnS=log(S+1) ;
    %Compute Weighted matrix W
    W=diag(S.^2);

    %parameters currently obtained: S,b0,gx,gy,gz,A,lnS,W
    %Solving A'WA*parameter=A'W*lnS
    parameter=(A'*W*A)\(A'*W*lnS');
    %extract S0 and D from parameter
    S0t=exp(parameter(1));

Dt=[parameter(2),parameter(5),parameter(6);parameter(5),parameter(3),
parameter(7);parameter(6),parameter(7),parameter(4)];

     %Now derive the diffusion parameters
                 Dav = trace(Dt)/3;
                 S0it = S0t;

      %First find the eigenvalues of D and sort them
                 [V,D1] = eig(Dt);
                 [Y,I] = sort(diag(D1));
                 I(:) = 4-I(:);          % Descending order index
                 Vs(:,:) = V(:,I);       % Sort eigenvectors
                 Es = Y(4-(1:3));        % Sort eigenvalues
```

```
      %Finding the components of the principal eigenvector
                  EigX = Vs(1,1);
                  EigY = Vs(2,1);
                  EigZ = Vs(3,1);

      %A neat way to compute FA:
                  L = Dav*eye(3,3);
                  Z = D1 - L;
                  FA = sqrt(3/2)*(sqrt(trace(Z.^2))/ sqrt(trace(D1.^2)));
      %Compute the scaled Relative Anistropy sRA
                  sRA = sqrt(trace(Z.^2))/(sqrt(6)*Dav);
      %Compute the Volume Fraction VF
                  VF = 1 - D1(1,1)*D1(2,2)*D1(3,3)/Dav^3 ;
      %Compute the Geodesic Anisotropy GA
                   lg=log(Es) ; %Find the log of the eigenvalues
                   avelg=mean(lg) ;
                   difflg=(lg-avelg).^2;
                   GA=sum(difflg)^0.5 ;

     %Reading out the eigenvalues:
                  D11 = Es(1);
                  D22 = Es(2);
                  D33 = Es(3);
                  AllD(:,:) = D;

      %Now split the original tensor D into its isotropic part (DIS)
      % and anisotropic part (DIS) where D=DAN + DIS
                  DIS=trace(D)*eye(3,3)/3;
                  DAN=D-DIS;

      %Calculate the norm of the tensor
                  NORM=sqrt(trace(D*D'));

      %Calculate the mode
                  MODE=3*sqrt(6)*det(DAN)/sqrt(trace(DAN*DAN'));

      %Calculate the anisotropy types
                  CL=(D11-D22)/(D11+D22+D33) ;
                  CP=2*(D22-D33)/(D11+D22+D33) ;
                  CS=3*D33/(D11+D22+D33) ;

       %Form the three Aziz-invariants
        I1=D11+D22+D33 ;
        I2=D11*D22 + D11*D33 + D22*D33 ;
        I3=D11*D22*D33 ;


      %Giving positions to the negative eigenvalues:
                  if D33 < 0.0
                      negatives = 1.0;
                  end
       true = [D11 D22 D33 Dav NORM FA sRA VF MODE CL CP CS I1 I2 I3 GA] ;

%Done ++++++++++++++++++++++++++++++++++++++++++++

%Now do many simulations
for q=1:sim
    noise=randn(1,d+1)*S0/SNR ; %Create noise from a normal dist with
                                %mean 0 and std dev S0/SNR
```

```
    Snoisy = Strue + noise ;

    %Calculate measured signal for each gradient direction
    bD = (log(Snoisy(1))-log(Snoisy)) ;
    S=Snoisy(1)*exp(-bD);


    %Now fit the tensor ********************

    lnS=log(S+1) ;
    %Compute Weighted matrix W
    W=diag(S.^2);

    %parameters currently obtained: S,b0,gx,gy,gz,A,lnS,W
    %Solving A'WA*parameter=A'W*lnS
    parameter=(A'*W*A)\(A'*W*lnS') ;
    %extract S0 and D from parameter

D=[parameter(2),parameter(5),parameter(6);parameter(5),parameter(3),
parameter(7);parameter(6),parameter(7),parameter(4)];
     %Now derive the diffusion parameters
                 Dav = trace(D)/3;
                 S0i = exp(parameter(1));

      %First find the eigenvalues of D and sort them
                 [V,D1] = eig(D);
                 [Y,I] = sort(diag(D1));
                 I(:) = 4-I(:);          % Descending order index
                 Vs(:,:) = V(:,I);       % Sort eigenvectors
                 Es = Y(4-(1:3));        % Sort eigenvalues

      %Finding the components of the principal eigenvector
                 EigX = Vs(1,1);
                 EigY = Vs(2,1);
                 EigZ = Vs(3,1);

      %A neat way to compute FA:
                 L = Dav*eye(3,3);
                 Z = D1 - L;
                 FA = sqrt(3/2)*(sqrt(trace(Z.^2)) /sqrt(trace(D1.^2)));
      %Compute the scaled Relative Anistropy sRA
                 sRA = sqrt(trace(Z.^2))/(sqrt(6)*Dav);
      %Compute the Volume Fraction VF
                 VF = 1 - D1(1,1)*D1(2,2)*D1(3,3)/Dav^3 ;
      %Compute the Geodesic Anisotropy GA
                  lg=log(Es) ; %Find the log of the eigenvalues
                  avelg=mean(lg) ;
                  difflg=(lg-avelg).^2;
                  GA=sum(difflg)^0.5 ;


      %Reading out the eigenvalues:
                 D11 = Es(1);
                 D22 = Es(2);
                 D33 = Es(3);
                 AllD(:,:) = D;

      %Now split the original tensor D into its isotropic part (DIS)
      %and anisotropic part (DIS) where D=DAN + DIS
```

```
                DIS=trace(D)*eye(3,3)/3;
                DAN=D-DIS;

      %Calculate the norm of the tensor
                NORM=sqrt(trace(D*D'));

      %Calculate the mode
                MODE=3*sqrt(6)*det(DAN)/sqrt(trace(DAN*DAN'));

      %Calculate the anisotropy types
                CL=(D11-D22)/(D11+D22+D33) ;
                CP=2*(D22-D33)/(D11+D22+D33) ;
                CS=3*D33/(D11+D22+D33) ;

       %Form the three Aziz-invariants
        I1=D11+D22+D33 ;
        I2=D11*D22 + D11*D33 + D22*D33 ;
        I3=D11*D22*D33 ;


      %Giving positions to the negative eigenvalues:
                if D33 < 0.0
                    negatives = 1.0;
                end

    %Find the SNR
    SNRsim = Strue./noise ;

    measure(q,:)=[Dav NORM FA sRA VF MODE CL CP CS I1 I2 I3 GA] ;
end

%Find the bias
bias=measure-repmat(true(4:16), sim, 1) ;
zbias=zscore(bias) ;

edges=[-3:0.1:3] ;
n = histc(zbias,edges,1) ;

figure(1) ;
plot(edges,n(:,1), '-k', edges,n(:,2),'--k', 'LineWidth',2)
xlabel('Bias of Normalized Metric','FontSize',12)
title(['ADC Bias: n=',num2str(sim), ', b=',num2str(B), ',
gradients=',num2str(d), ', SNR=', num2str(SNR)],'FontSize',12);
legend('MD','Norm');

figure(2) ;
plot(edges,n(:,3), '-k', edges,n(:,4), '--k',  edges,n(:,5), '-.k',
edges,n(:,13), '+:k','LineWidth',2 )
xlabel('Bias of Normalized Metric','FontSize',12)
%ylabel('Number of Simulations','FontSize',14)
title(['Anisotropy Bias: n=',num2str(sim), ', b=',num2str(B), ',
gradients=',num2str(d), ', SNR=', num2str(SNR)],'FontSize',12);
legend('FA','sRA', 'VF', 'GA');

figure(3) ;
plot(edges,n(:,6), 'k', edges,n(:,7), '--k',edges,n(:,8), ':k',
edges,n(:,9), '+:k', 'LineWidth',2)
xlabel('Bias of Normalized Metric','FontSize',12)
```

```
title(['Propagation Bias: n=',num2str(sim), ', b=',num2str(B), ',
gradients=',num2str(d), ', SNR=', num2str(SNR)],'FontSize',12);
legend('Mode', 'CL', 'CP', 'CS') ;

tend=clock ;
if tend(5)>=tstart(5)
    etime(1) = tend(4) - tstart(4);
    etime(2)=tend(5) - tstart(5);
else
    etime(1) = tend(4) - tstart(4) -1;
    etime(2)=tend(5) - tstart(5) +60 ;
end

fprintf('\nJob ended. \nFor N=%d simulations, time taken=%d hours %d
mins\n\n', sim, etime(1), etime(2)) ;
```

REFERENCES

Aguirre GK, Zarahn E, D'Esposito M. (1998): The variability of human, BOLD hemodynamic responses. Neuroimage 8(4):360-369.

Alexander GE, Crutcher MD, Delong MR. (1990): Basal Ganglia-Thalamocortical Circuits - Parallel Substrates for Motor, Oculomotor, Prefrontal and Limbic Functions. Progress in Brain Research 85:119-146.

Anderson AW. (2001): Theoretical analysis of the effects of noise on diffusion tensor imaging. Magnetic Resonance in Medicine 46(6):1174-1188.

Ankrom M, Gordon B, Selnes O. (2002): Mild cognitive impairment: Analysis of folstein mini-mental state exam. Gerontologist 42:132-133.

Arfanakis K, Haughton VM, Carew JD, Rogers BP, Dempsey RJ, Meyerand ME. (2002): Diffusion tensor MR imaging in diffuse axonal injury. American Journal of Neuroradiology 23(5):794-802.

Armitage PA, Bastin ME. (2000): Selecting an appropriate anisotropy index for displaying diffusion tensor imaging data with improved contrast and sensitivity. Magnetic Resonance in Medicine 44(1):117-121.

Arsigny V, Fillard P, Pennec X, Ayache N. (2006): Log-euclidean metrics for fast and simple calculus on diffusion tensors. Magnetic Resonance in Medicine 56(2):411-421.

Ashburner J, Friston KJ. (1999): Nonlinear spatial normalization using basis functions. Human Brain Mapping 7(4):254-266.

Athey RJ, Walker RW. (2006): Demonstration of cognitive decline in Parkinson's disease using the Cambridge Cognitive Assessment (Revised) (CAMCOG-R). International Journal of Geriatric Psychiatry 21(10):977-982.

Azuma T, Cruz RF, Bayles KA, Tomoeda CK, Montgomery EB. (2003): A longitudinal study of neuropsychological change in individuals with Parkinson's disease. International Journal of Geriatric Psychiatry 18(12):1115-1120.

Basser PJ, Jones DK. (2002): Diffusion-tensor MRI: theory, experimental design and data analysis - a technical review. Nmr in Biomedicine 15(7-8):456-467.

Basser PJ, Mattiello J, Lebihan D. (1994): Estimation of the Effective Self-Diffusion Tensor from the Nmr Spin-Echo. Journal of Magnetic Resonance Series B 103(3):247-254.

Basser PJ, Pajevic S. (2000): Statistical artifacts in diffusion tensor MRI (DT-MRI) caused by background noise. Magnetic Resonance in Medicine 44(1):41-50.

Bastin ME, Armitage PA, Marshall I. (1998): A theoretical study of the effect of experimental noise on the measurement of anisotropy in diffusion imaging. Magnetic Resonance Imaging 16(7):773-785.

Batchelor PG, Calamante F, Tournier JD, Atkinson D, Hill DLG, Connelly A. (2006): Quantification of the shape of fiber tracts. Magnetic Resonance in Medicine 55(4):894-903.

Batchelor PG, Moakher M, Atkinson D, Calamante F, Connelly A. (2005): A rigorous framework for diffusion tensor calculus. Magnetic Resonance in Medicine 53(1):221-225.

Bechinger B. (1999): The structure, dynamics and orientation of antimicrobial peptides in membranes by multidimensional solid-state NMR spectroscopy. Biochimica Et Biophysica Acta-Biomembranes 1462(1-2):157-183.

Behrens TEJ, Woolrich MW, Jenkinson M, Johansen-Berg H, Nunes RG, Clare S, Matthews PM, Brady JM, Smith SM. (2003): Characterization and propagation of uncertainty in diffusion-weighted MR imaging. Magnetic Resonance in Medicine 50(5):1077-1088.

Benjamini Y, Hochberg Y. (1995): Controlling the False Discovery Rate - a Practical and Powerful Approach to Multiple Testing. Journal of the Royal Statistical Society Series B-Methodological 57(1):289-300.

Bernstein M, King K, Zhou X. 2004. Handbook of MRI Pulse Sequences. Burlington: Elsevier Academic Press.

Bertrand E, Lechowicz W, Lewandowska E, Szpak G, Dymecki J, Kosno-Kruszewska E, Wierzba-Bobrowicz T. (2003): Degenerative axonal changes in the hippocampus and amygdala in Parkinson's disease. Folia Neuropathologica 41(4):197-207.

Bigler ED. (2001): Neuropsychological testing defines the neurobehavioral significance of neuroimaging-identified abnormalities. Archives of Clinical Neuropsychology 16(3):227-236.

Binder JR, Frost JA, Hammeke TA, Bellgowan PSF, Rao SM, Cox RW. (1999): Conceptual processing during the conscious resting state: A functional MRI study. Journal of Cognitive Neuroscience 11(1):80-93.

Bliss TVP, Collingridge GL. (1993): A Synaptic Model of Memory - Long-Term Potentiation in the Hippocampus. Nature 361(6407):31-39.

Boecker H, Kleinschmidt A, Requardt M, Hanicke W, Merboldt KD, Frahm J. (1994): Functional Cooperativity of Human Cortical Motor Areas During Self-Paced Simple Finger Movements - a High-Resolution Mri Study. Brain 117:1231-1239.

Bozzali M, Falini A, Cercignani M, Baglio F, Farina E, Alberoni M, Vezzulli P, Olivotto F, Mantovani F, Shallice T and others. (2005): Brain tissue damage in dementia with Lewy bodies: an in vivo diffusion tensor MRI study. Brain 128:1595-1604.

Braak H, Braak E, Yilmazer D, deVos RAI, Jansen ENH, Bohl J. (1996): Pattern of brain destruction in Parkinson's and Alzheimer's diseases. Journal of Neural Transmission 103(4):455-490.

Brandstack N, Kurki T, Tenovuo O, Isoniemi H. (2006): MR imaging of head trauma: Visibility of contusions and other intraparenchymal injuries in early and late stage. Brain Injury 20(4):409-416.

Braver TS, Cohen JD, Nystrom LE, Jonides J, Smith EE, Noll DC. (1997): A parametric study of prefrontal cortex involvement in human working memory. Neuroimage 5(1):49-62.

Brett M, Anton J-L, Valabregue R, Poline J-B. Region of interest analysis using an SPM toolbox; 2002; Sendai, Japan.

Bruck A, Kurki T, Kaasinen V, Vahlberg T, Rinne JO. (2004): Hippocampal and prefrontal atrophy in patients with early non-demented Parkinson's disease is related to cognitive impairment. Journal of Neurology Neurosurgery and Psychiatry 75(10):1467-1469.

Burton MW, Small SL. (1999): An introduction to functional magnetic resonance imaging. Neurologist 5(3):145-158.

Caparroslefebvre D, Pecheux N, Petit V, Duhamel A, Petit H. (1995): Which Factors Predict Cognitive Decline in Parkinsons-Disease. Journal of Neurology Neurosurgery and Psychiatry 58(1):51-55.

Carr HY, Purcell EM. (1954): Effects of Diffusion on Free Precession in Nuclear Magnetic Resonance Experiments. Physical Review 94(3):630-638.

Castano-Moraga CA, Lenglet C, Deriche R, Ruiz-Alzola J. (2007): A Riemannian approach to anisotropic filtering of tensor fields. Signal Processing 87(2):263-276.

Cavanna AE, Trimble MR. (2006): The precuneus: a review of its functional anatomy and behavioural correlates. Brain 129:564-583.

Celone KA, Calhoun VD, Dickerson BC, Atri A, Chua EF, Miller SL, DePeau K, Rentz DM, Selkoe DJ, Blacker D and others. (2006): Alterations in memory networks in mild cognitive impairment and Alzheimer's disease: An independent component analysis. Journal of Neuroscience 26(40):10222-10231.

Chan JHM, Tsui EYK, Peh WCG, Fong D, Fok KF, Leung KM, Yuen MK, Fung KKL. (2003): Diffuse axonal injury: detection of changes in anisotropy of water diffusion diffusion-weighted imaging. Neuroradiology 45(1):34-38.

Cherubini A, Luccichenti G, Peran P, Hagberg GE, Barba C, Formisano R, Sabatini U. (2007): Multimodal MRI tractography in normal subjects and in clinically recovered traumatic brain injury patients. Neuroimage 34(4):1331-1341.

Chun T, Filippi CG, Zimmerman RD, Ulug AM. (2000): Diffusion changes in the aging human brain. American Journal of Neuroradiology 21(6):1078-1083.

Ciccarelli O, Behrens TE, Altmann DR, Orrell RW, Howard RS, Johansen-Berg H, Miller DH, Matthews PM, Thompson AJ. (2006): Probabilistic diffusion tractography: a potential tool to assess the rate of disease progression in amyotrophic lateral sclerosis. Brain 129:1859-1871.

Cohen JD, Perlstein WM, Braver TS, Nystrom LE, Noll DC, Jonides J, Smith EE. (1997): Temporal dynamics of brain activation during a working memory task. Nature 386(6625):604-608.

Corouge I, Fletcher PT, Joshi S, Gouttard S, Gerig G. (2006): Fiber tract-oriented statistics for quantitative diffusion tensor MRI analysis. Medical Image Analysis 10(5):786-798.

CroninGolomb A, Braun AE. (1997): Visuospatial dysfunction and problem solving in Parkinson's disease. Neuropsychology 11(1):44-52.

Croningolomb A, Corkin S, Growdon JH. (1994): Impaired Problem-Solving in Parkinsons-Disease - Impact of a Set-Shifting Deficit. Neuropsychologia 32(5):579-593.

Dalrymple-Alford J. (2001): Comparative neuropsychology of Lewy body and Alzheimer's dementia. Journal of Neurology Neurosurgery and Psychiatry 70(2):148-148.

Dalrymple-Alford J, Kalders A, Jones R, Watson R. (1994): A central executive deficit in patients with Parkinson’s disease. Journal of Neurology Neurosurgery & Psychiatry 57:360–367.

Dubois B, Pillon B. (1997): Cognitive deficits in Parkinson's disease. Journal of Neurology 244(1):2-8.

Durston S, Casey BJ. (2006): What have we learned about cognitive development from neuroimaging? Neuropsychologia 44(11):2149-2157.

Eichenbaum H. (2006): Remembering: Functional organization of the declarative memory system. Current Biology 16(16):R643-R645.

Einstein A. (1905): On the Motion Required by the Molecular Kinetic Theory of Heat of Small Particles Suspended in a Stationary Liquid. Annalen der Physik 17:549-560.

Emre M. (2003): Dementia associated with Parkinson's disease. Lancet Neurology 2(4):229-237.

Ennis DB, Kindlmann G. (2006): Orthogonal tensor invariants and the analysis of diffusion tensor magnetic resonance images. Magnetic Resonance in Medicine 55(1):136-146.

Fillard P, Arsigny V, Ayache N, Pennec X. 2005. A Riemannian framework for the processing of tensor-valued images. Deep Structure, Singularities, and Computer Vision. p 112-123.

Fischl B, Liu A, Dale AM. (2001): Automated manifold surgery: Constructing geometrically accurate and topologically correct models of the human cerebral cortex. Ieee Transactions on Medical Imaging 20(1):70-80.

Fletcher PT, Joshi S. 2004. Principal geodesic analysis on symmetric spaces: Statistics of diffusion tensors. Computer Vision and Mathematical Methods in Medical and Biomedical Image Analysis. p 87-98.

Fletcher PT, Joshi S. (2007): Riemannian geometry for the statistical analysis of diffusion tensor data. Signal Processing 87(2):250-262.

Fransson P. (2005): Spontaneous low-frequency BOLD signal fluctuations: An fMRI investigation of the resting-state default mode of brain function hypothesis. Human Brain Mapping 26(1):15-29.

Friston KJ, Price CJ, Fletcher P, Moore C, Frackowiak RSJ, Dolan RJ. (1996): The trouble with cognitive subtraction. Neuroimage 4(2):97-104.

Fung WK. (1995): Diagnostics in Linear Discriminant-Analysis. Journal of the American Statistical Association 90(431):952-956.

Galanaud D, Nicoli F, Chinot O, Confort-Gouny S, Figarella-Branger D, Roche P, Fuentes S, Le Fur Y, Ranjeva JP, Cozzone PJ. (2006): Noninvasive diagnostic assessment of brain tumors using combined in vivo MR imaging and spectroscopy. Magnetic Resonance in Medicine 55(6):1236-1245.

Gale SD, Baxter L, Roundy N, Johnson SC. (2005): Traumatic brain injury and grey matter concentration: a preliminary voxel based morphometry study. Journal of Neurology Neurosurgery and Psychiatry 76(7):984-988.

Galvin JE, Pollack J, Morris JC. (2006): Clinical phenotype of Parkinson disease dementia. Neurology 67(9):1605-1611.

Gati JS, Menon RS, Ugurbil K, Rutt BK. (1997): Experimental determination of the BOLD field strength dependence in vessels and tissue. Magnetic Resonance in Medicine 38(2):296-302.

Gelb DJ, Oliver E, Gilman S. (1999): Diagnostic criteria for Parkinson disease. Archives of Neurology 56(1):33-39.

Genovese CR, Lazar NA, Nichols T. (2002): Thresholding of statistical maps in functional neuroimaging using the false discovery rate. Neuroimage 15(4):870-878.

Gevins A, Cutillo B. (1993): Spatiotemporal Dynamics of Component Processes in Human Working-Memory. Electroencephalography and Clinical Neurophysiology 87(3):128-143.

Goetz P, Blamire A, Rajagopalan B, Cadoux-Hudson T, Young D, Styles P. (2004): Increase in apparent diffusion coefficient in normal appearing white matter following human traumatic brain injury correlates with injury severity. Journal of Neurotrauma 21(6):645-654.

Goodman JC. (1994): Pathological-Changes in Mild Head-Injury. Seminars in Neurology 14(1):19-24.

Greicius MD, Krasnow B, Reiss AL, Menon V. (2003): Functional connectivity in the resting brain: A network analysis of the default mode hypothesis. Proceedings of the National Academy of Sciences of the United States of America 100(1):253-258.

Gusnard DA, Raichle ME. (2001): Searching for a baseline: Functional imaging and the resting human brain. Nature Reviews Neuroscience 2(10):685-694.

Guye M, Parker GJM, Symms M, Boulby P, Wheeler-Kingshott CAM, Salek-Haddadi A, Barker GJ, Duncan JS. (2003): Combined functional MRI and tractography to demonstrate the connectivity of the human primary motor cortex in vivo. Neuroimage 19(4):1349-1360.

Haacke EM, Brown RW, Thompson MR, Venkatesan R. 1999. Magnetic resonance imaging : physical principles and sequence design New York Wiley.

Hamilton J, Salmon D, Galasko D, Delis D, Hansen L. (2004): A comparison of episodic memory deficits in neuropathologically-confirmed dementia with Lewy bodies and Alzheimer's disease. JINS 10:689-697.

Hamstra DA, Chenevert TL, Moffat BA, Johnson TD, Meyer CR, Mukherji SK, Quint DJ, Gebarski SS, Fan XY, Tsien CI and others. (2005): Evaluation of the functional diffusion map as an early biomarker of time-to-progression and overall survival in high-grade glioma. Proceedings of the National Academy of Sciences of the United States of America 102(46):16759-16764.

Hegde ML, Gupta VB, Anitha M, Hankrishna T, Shankar SK, Muthane U, Rao KS, Rao KSJ. (2006): Studies on genomic DNA topology and stability in brain regions of Parkinson's disease. Archives of Biochemistry and Biophysics 449(1-2):143-156.

Heitger MH, Anderson TJ, Jones RD, Dalrymple-Alford JC, Frampton CM, Ardagh MW. (2004): Eye movement and visuomotor arm movement deficits following mild closed head injury. Brain 127:575-590.

Heitger MH, Jones RD, Dalrymple-Alford JC, Frampton CM, Ardagh MW, Anderson TJ. (2006): Motor deficits and recovery during the first year following mild closed head injury. Brain Injury 20(8):807-824.

Holmes AP, Blair RC, Watson JDG, Ford I. (1996): Nonparametric analysis of statistic images from functional mapping experiments. Journal of Cerebral Blood Flow and Metabolism 16(1):7-22.

Hristova DR, Grozdev IS. (2007): Level of movement, cognitive and emotional disturbances and their correlation in patients with Parkinson's disease. Movement Disorders 22:S220-S221.

Huang CR, Mattis P, Tang CK, Perrine K, Carbon M, Eidelberg D. (2007): Metabolic brain networks associated with cognitive function in Parkinson's disease. Neuroimage 34(2):714-723.

Huisman T, Schwamm LH, Schaefer PW, Koroshetz WJ, Shetty-Alva N, Ozsunar Y, Wu O, Sorensen AG. (2004): Diffusion tensor imaging as potential biomarker of white matter injury in diffuse axonal injury. American Journal of Neuroradiology 25(3):370-376.

Huisman T, Sorensen AG, Hergan K, Gonzalez RG, Schaefer PW. (2003): Diffusion-weighted Imaging for the evaluation of diffuse axonal injury in closed head injury. Journal of Computer Assisted Tomography 27(1):5-11.

Idiaquez J, Benarroch EE, Rosales H, Milla P, Rios L. (2007): Autonomic and cognitive dysfunction in Parkinson's disease. Clinical Autonomic Research 17(2):93-98.

Inglese M, Makani S, Johnson G, Cohen BA, Silver JA, Gonen O, Grossman RI. (2005): Diffuse axonal injury in mild traumatic brain injury: a diffusion tensor imaging study. Journal of Neurosurgery 103(2):298-303.

Jantzen KJ, Anderson B, Steinberg FL, Kelso JAS. (2004): A prospective functional MR imaging study of mild traumatic brain injury in college football players. American Journal of Neuroradiology 25(5):738-745.

Janvin C, Aarsland D, Larsen JP, Hugdahl K. (2003): Neuropsychological profile of patients with Parkinson's disease without dementia. Dementia and Geriatric Cognitive Disorders 15(3):126-131.

Janvin CC, Aarsland D, Larsen JP. (2005): Cognitive predictors of dementia in Parkinson's disease: A community-based, 4-year longitudinal study. Journal of Geriatric Psychiatry and Neurology 18(3):149-154.

Jaroniec CP, MacPhee CE, Bajaj VS, McMahon MT, Dobson CM, Griffin RG. (2004): High-resolution molecular structure of a peptide in an amyloid fibril determined by magic angle spinning NMR spectroscopy. Proceedings of the National Academy of Sciences of the United States of America 101(3):711-716.

Jiang HY, van Zijl PCM, Kim J, Pearlson GD, Mori S. (2006): DtiStudio: Resource program for diffusion tensor computation and fiber bundle tracking. Computer Methods and Programs in Biomedicine 81(2):106-116.

Junque C, Ramirez-Ruiz B, Tolosa E, Summerfield C, Marti MJ, Pastor P, Gomez-Anson B, Mercader JM. (2005): Amygdalar and hippocampal MRI volumetric reductions in Parkinson's disease with dementia. Movement Disorders 20(5):540-544.

Kane NM, Moss TH, Curry SH, Butler SR. (1998): Quantitative electroencephalographic evaluation of non-fatal and fatal traumatic coma. Electroencephalography and Clinical Neurophysiology 106(3):244-250.

Kingsley P. (2006a): Introduction to diffusion tensor imaging mathematics: Part II. Anisotropy, diffusion-weighting factors, and gradient encoding schemes. Concepts in Magnetic Resonance Part A 28A(2):123-154.

Kingsley P. (2006b): Introduction to diffusion tensor imaging mathematics: Part III. Tensor calculation, noise, simulations, and optimization. Concepts in Magnetic Resonance Part A 28A(2):155-179.

Lauterbur P. (1973): Image Formation by Induced Local Interactions - Examples Employing Nuclear Magnetic-Resonance. Nature 242(5394):190-191.

Le Bihan D. 1995. Magnetic Resonance Imaging of Diffusion and Perfusion: Applications to Functional Imaging. New York: Lippincott-Raven Press.

Lee KC, Sud S, Meyer CR, Moffat BA, Chenevert TL, Rehemtulla A, Pienta KJ, Ross BD. (2007): An Imaging biomarker of early treatment response in prostate cancer that has metastasized to the bone. Cancer Research 67(8):3524-3528.

Levin BE, Llabre MM, Reisman S, Weiner WJ, Sanchezramos J, Singer C, Brown MC. (1991): Visuospatial Impairment in Parkinsons-Disease. Neurology 41(3):365-369.

Levy G, Jacobs DM, Tang MX, Cote LJ, Louis ED, Alfaro B, Mejia H, Stern Y, Marder K. (2002): Memory and executive function impairment predict dementia in Parkinson's disease. Movement Disorders 17(6):1221-1226.

Lewis SJG, Cools R, Robbins TW, Dove A, Barker RA, Owen AM. (2003a): Using executive heterogeneity to explore the nature of working memory deficits in Parkinson's disease. Neuropsychologia 41(6):645-654.

Lewis SJG, Dove A, Robbins TW, Barker RA, Owen AM. (2003b): Cognitive impairments in early Parkinson's disease are accompanied by reductions in activity in frontostriatal neural circuitry. Journal of Neuroscience 23(15):6351-6356.

Lin FC, Yu CS, Jiang TZ, Li KC, Zhu CZ, Zhu WL, Qin W, Duan YY, Xuan Y, Sun H and others. (2006): Discriminative analysis of relapsing neuromyelitis optica and relapsing-remitting multiple sclerosis based on two-dimensional histogram from diffusion tensor imaging. Neuroimage 31(2):543-549.

Litvan I, Mohr E, Williams J, Gomez C, Chase TN. (1991): Differential Memory and Executive Functions in Demented Patients with Parkinsons and Alzheimers-Disease. Journal of Neurology Neurosurgery and Psychiatry 54(1):25-29.

Liu AY, Maldjian JA, Bagley LJ, Sinson GP, Grossman RI. (1999): Traumatic brain injury: Diffusion-weighted MR imaging findings. American Journal of Neuroradiology 20(9):1636-1641.

Loucks RB. 1997. Use of a correlation coefficient for conditional averaging. Adelphi, USA: Army Research Laboratory.

Mahieux F, Fenelon G, Flahault A, Manifacier MJ, Michelet D, Boller F. (1998): Neuropsychological prediction of dementia in Parkinson's disease. Journal of Neurology Neurosurgery and Psychiatry 64(2):178-183.

Mansfield P. (1977): Multi-planar image formation using NMR spin echoes. Journal of Physics C: Solid State Physics. 10:L55-58.

Mansfield P, Maudsley AA, Baines T. (1976): Fast Scan Proton Density Imaging by Nmr. Journal of Physics E-Scientific Instruments 9(4):271-278.

Marinus J, Visser M, Verwey NA, Verhey FRJ, Middelkoop HAM, Stiggelbout AM, van Hilten JJ. (2003): Assessment of cognition in Parkinson's disease. Neurology 61(9):1222-1228.

Marks W, Brockhuis B, Lass P, Wieczorek D, Zapasnik A, Lasek J, Witkowski Z. (2006): Brain perfusion imaging (SPECT-Tc-99m HM-PAO) in diagnosis of diffuse axonal injury. Neurosurgery Quarterly 16(2):89-91.

Mathias JL, Beall JA, Bigler ED. (2004): Neuropsychological and information processing deficits following mild traumatic brain injury. Journal of the International Neuropsychological Society 10(2):286-297.

Mattiello J, Basser PJ, LeBihan D. (1997): The b matrix in diffusion tensor echo-planar imaging. Magnetic Resonance in Medicine 37(2):292-300.

Mazoyer B, Zago L, Mellet E, Bricogne S, Etard O, Houde O, Crivello F, Joliot M, Petit L, Tzourio-Mazoyer N. (2001): Cortical networks for working memory and executive functions sustain the conscious resting state in man. Brain Research Bulletin 54(3):287-298.

McAllister TW, Saykin AJ, Flashman LA, Sparling MB, Johnson SC, Guerin SJ, Mamourian AC, Weaver JB, Yanofsky N. (1999): Brain activation during working memory 1 month after mild traumatic brain injury - A functional MRI study. Neurology 53(6):1300-1308.

McCormick DA, Bal T. (1997): Sleep and arousal: Thalamocortical mechanisms. Annual Review of Neuroscience 20:185-215.

McKeith I. (2004): Dementia in Parkinson's disease: common and treatable. Lancet Neurology 3(8):456-456.

McKiernan KA, Kaufman JN, Kucera-Thompson J, Binder JR. (2003): A parametric manipulation of factors affecting task-induced deactivation in functional neuroimaging. Journal of Cognitive Neuroscience 15(3):394-408.

McKinlay A, Dalrymple-Alford J, Anderson T, Fink J, Hudson I. Towards a concept of Parkinson's disease-mild cognitive impairment. ; 2004; Basel.

McRobbie D, Moore E, Graves M, Prince M. 2003. MRI From Picture to Proton. Cambridge: University Press.

Meythaler JM, Peduzzi JD, Eleftheriou E, Novack TA. (2001): Current concepts: Diffuse axonal injury-associated traumatic brain injury. Archives of Physical Medicine and Rehabilitation 82(10):1461-1471.

Middleton FA, Strick PL. (1994): Anatomical Evidence for Cerebellar and Basal Ganglia Involvement in Higher Cognitive Function. Science 266(5184):458-461.

Moffat BA, Chenevert TL, Meyer CR, McKeever PE, Hall DE, Hoff BA, Johnson TD, Rehemtulla A, Ross BD. (2006): The functional diffusion map: An imaging biomarker for the early prediction of cancer treatment outcome. Neoplasia 8(4):259-267.

Moore DS, McCabe GP. 2006. Introduction to the practice of statistics. New York: W.H. Freeman and Co.

Mori S, Crain BJ, Chacko VP, van Zijl PCM. (1999): Three-dimensional tracking of axonal projections in the brain by magnetic resonance imaging. Annals of Neurology 45(2):265-269.

Moseley IF. (2000): The neuroimaging evidence for chronic brain damage due to boxing. Neuroradiology 42(1):1-8.

Mtumbuka MC, Edwards DJ. Increasing Channel Capacity using a Dual-spaced Tri-Polarised (DSTP) MIMO System. In: Fapojuwo AO, editor; 2004. ACTA Press.

Nadel L, Moscovitch M. (2001): The hippocampal complex and long-term memory revisited. Trends in Cognitive Sciences 5(6):228-230.

Nedd K, Sfakianakis G, Ganz W, Uricchio B, Vernberg D, Villanueva P, Jabir AM, Bartlett J, Keena J. (1993): Tc-99m-Hmpao Spect of the Brain in Mild-to-Moderate Traumatic Brain Injury Patients - Compared with Ct - a Prospective-Study. Brain Injury 7(6):469-479.

Nelson A, Fogel BS, Faust D. (1986): Bedside Cognitive Screening Instruments - a Critical-Assessment. Journal of Nervous and Mental Disease 174(2):73-83.

Newsome MR, Scheibel RS, Steinberg JL, Troyanskaya M, Sharma RG, Rauch RA, Li XQ, Levin HS. (2007): Working memory brain activation following severe traumatic brain injury. Cortex 43(1):95-111.

Nichols T, Hayasaka S. (2003): Controlling the familywise error rate in functional neuroimaging: a comparative review. Statistical Methods in Medical Research 12(5):419-446.

Nichols TE, Holmes AP. (2002): Nonparametric permutation tests for functional neuroimaging: A primer with examples. Human Brain Mapping 15(1):1-25.

Nystrom LE, Braver TS, Sabb FW, Delgado MR, Noll DC, Cohen JD. (2000): Working memory for letters, shapes, and locations: fMRI evidence against stimulus-based regional organization in human prefrontal cortex. Neuroimage 11(5):424-446.

Olton DS, Becker JT, Handelmann GE. (1979): Hippocampus, Space, and Memory. Behavioral and Brain Sciences 2(3):313-322.

Owen AM, James M, Leigh PN, Summers BA, Marsden CD, Quinn NP, Lange KW, Robbins TW. (1992): Fronto-Striatal Cognitive Deficits at Different Stages of Parkinsons-Disease. Brain 115:1727-1751.

Owen AM, McMillan KM, Laird AR, Bullmore E. (2005): N-back working memory paradigm: A meta-analysis of normative functional neuroimaging. Human Brain Mapping 25(1):46-59.

Park MY, Kang HU, Jung GY. (2007): Diffusion tensor MR imaging for evaluation of fronto-subcortical neural pathway changes in Parkinson's disease with dementia. Movement Disorders 22:S142-S142.

Paschal CB, Morris HD. (2004): k-space in the clinic. Journal of Magnetic Resonance Imaging 19(2):145-159.

Perry RJ, Hodges JR. (1999): Attention and executive deficits in Alzheimer's disease - A critical review. Brain 122:383-404.

Persson J, Lustig C, Nelson JK, Reuter-Lorenz PA. (2007): Age differences in deactivation: A link to cognitive control? Journal of Cognitive Neuroscience 19(6):1021-1032.

Piatt AL, Fields JA, Paolo AM, Koller WC, Troster AI. (1999): Lexical, semantic, and action verbal fluency in Parkinson's disease with and without dementia. Journal of Clinical and Experimental Neuropsychology 21(4):435-443.

Pointinger H, Sarahrudi K, Poeschl G, Munk P. (2002): Electroencephalography in primary diagnosis of mild head trauma. Brain Injury 16(9):799-805.

Poline JB, Worsley KJ, Evans AC, Friston KJ. (1997): Combining spatial extent and peak intensity to test for activations in functional imaging. Neuroimage 5(2):83-96.

Price CJ, Friston KJ. (1997): Cognitive conjunction: A new approach to brain activation experiments. Neuroimage 5(4):261-270.

Raafat RM, Dresner MA, Counsel SJ, Srinivasan L, Hajnal JV, Edwards AD. (2007): Assessment of the visual system in preterm infants using diffusion tractography and fMRI. Early Human Development 83(2):127-128.

Rabadi MH, Jordan BD. (2001): The cumulative effect of repetitive concussion in sports. Clinical Journal of Sport Medicine 11(3):194-198.

Raichle ME, MacLeod AM, Snyder AZ, Powers WJ, Gusnard DA, Shulman GL. (2001): A default mode of brain function. Proceedings of the National Academy of Sciences of the United States of America 98(2):676-682.

Rombouts S, Barkhof F, Goekoop R, Stam CJ, Scheltens P. (2005): Altered resting state networks in mild cognitive impairment and mild Alzheimer's disease: An fMRI study. Human Brain Mapping 26(4):231-239.

Salmond CH, Menon DK, Chatfield DA, Williams GB, Pena A, Sahakian BJ, Pickard JD. (2006): Diffusion tensor imaging in chronic head injury survivors: Correlations with learning and memory indices. Neuroimage 29(1):117-124.

Scherfler C, Schocke MF, Seppi K, Esterhammer R, Brenneis C, Jaschke W, Wenning GK, Poewe W. (2006): Voxel-wise analysis of diffusion weighted imaging reveals disruption of the olfactory tract in Parkinson's disease. Brain 129:538-542.

Schmahmann JD. (2003): Vascular syndromes of the thalamus. Stroke 34(9):2264-2278.

Schonberg T, Pianka P, Hendler T, Pasternak O, Assaf Y. (2006): Characterization of displaced white matter by brain tumors using combined DTI and fMRI. Neuroimage 30(4):1100-1111.

Shaw NA. (2002): Neurophysiology of concussion. Progress in Neurobiology 67(4):281-344.

Shiga T, Ikoma K, Katoh C, Isoyama H, Matsuyama T, Kuge Y, Kageyama H, Kohno T, Terae S, Tamaki N. (2006): Loss of neuronal integrity: a cause of hypometabolism in patients with traumatic brain injury without MRI abnormality in the chronic stage. European Journal of Nuclear Medicine and Molecular Imaging 33(7):817-822.

Shinoura N, Yamada R, Kodama T, Suzuki Y, Takahashi M, Yagi K. (2005): Preoperative fMRI, tractography and continuous task during awake surgery for maintenance of motor function following surgical resection of metastatic tumor spread to the primary motor area. Minimally Invasive Neurosurgery 48(2):85-90.

Shulman GL, Corbetta M, Buckner RL, Fiez JA, Miezin FM, Raichle ME, Petersen SE. (1997): Common blood flow changes across visual tasks .1. Increases in subcortical structures and cerebellum but not in nonvisual cortex. Journal of Cognitive Neuroscience 9(5):624-647.

Simard M. (1998): The Mini-Mental State Examination: Strengths and Weaknesses of a Clinical Instrument. The Canadian Alzheimer Disease Review:10-12.

Simard M, van Reekum R. (1999): Memory assessment in studies of cognition-enhancing drugs for Alzheimer's disease. Drugs & Aging 14(3):197-230.

Siotani M. (1956): On the distribution of Hotelling's T^2-test. Ann. Inst. Statist. Math. 8:1-14.

Slemmer JE, Matser EJT, De Zeeuw CI, Weber JT. (2002): Repeated mild injury causes cumulative damage to hippocampal cells. Brain 125:2699-2709.

Soto-Ares G, Vinchon M, Delmaire C, Abecidan E, Dhellemes P, Pruvo JP. (2001): Cerebellar atrophy after severe traumatic head injury in children. Childs Nervous System 17(4-5):263-269.

Srivastava S, Govil G. (2001): Application of NMR to the study of cells and body fluids. Current Organic Chemistry 5(10):1039-1057.

Stuss D, Knight R. 2002. Principles of Frontal Lobe Function. New York: Oxford University Press.

Takahashi E, Ohki K, Kim DS. (2007): Diffusion tensor studies dissociated two fronto-temporal pathways in the human memory system. Neuroimage 34(2):827-838.

Takayama H, Kobayashi M, Sugishita M, Mihara B. (2000): Diffusion-weighted imaging demonstrates transient cytotoxic edema involving the corpus callosum in a patient with diffuse brain injury. Clinical Neurology and Neurosurgery 102(3):135-139.

Tam CWC, Burton EJ, McKeith IG, Burn DJ, O'Brien JT. (2005): Temporal lobe atrophy on MRI in Parkinson disease with dementia - A comparison with Alzheimer disease and dementia with Lewy bodies. Neurology 64(5):861-865.

Theilmann RJ, Borders R, Trouard TP, Xia GW, Outwater E, Ranger-Moore J, Gillies RJ, Stopeck A. (2004): Changes in water mobility measured by diffusion MRI predict response of metastatic breast cancer to chemotherapy. Neoplasia 6(6):831-837.

Toosy AT, Ciccarelli O, Parker GJM, Wheeler-Kingshott CAM, Miller DH, Thompson AJ. (2004): Characterizing function-structure relationships in the human visual system with functional MRI and diffusion tensor imaging. Neuroimage 21(4):1452-1463.

Trivedi MA, Murphy CM, Pagonabarrago JM, Goldman JG, DeToledo-Morrell L, Stebbins GT. (2007): A comparison of white matter changes in patients with Parkinson's disease and Alzheimer's disease relative to cognitively-healthy elderly controls using diffusion tensor imaging. Movement Disorders 22:S149-S150.

Troyer A, Moscovitch M, Winocur G, Leach L, Freedman M. (1998): Clustering and switching on verbal fluency tests in Alzheimer's and Parkinson's disease. JINS 4:137-143.

Vingerhoets G, Verleden S, Santens P, Miatton M, De Reuck J. (2003): Predictors of cognitive impairment in advanced Parkinson's disease. Journal of Neurology Neurosurgery and Psychiatry 74(6):793-796.

Vojtech F, Vaclav H. 2004. Statistical Pattern Recognition Toolbox for Matlab. Center for Machine Perception, K13133 FEE Czech Technical University, Prague, Czech Republic. Report nr CTU--CMP--2004--08. 105 p.

Walter H, Vasic N, Hose A, Spitzer M, Wolf RC. (2007): Working memory dysfunction in schizophrenia compared to healthy controls and patients with depression: Evidence from event-related fMRI. Neuroimage 35(4):1551-1561.

Watts R, Liston C, Niogi S, Ulug AM. (2003): Fiber tracking using magnetic resonance diffusion tensor imaging and its applications to human brain development. Mental Retardation and Developmental Disabilities Research Reviews 9(3):168-177.

Werheid K, Hoppe C, Thone A, Muller U, Mungersdorf M, von Cramon DY. (2002): The Adaptive Digit Ordering Test Clinical application, reliability, and validity of a verbal working memory test. Archives of Clinical Neuropsychology 17(6):547-565.

Westin CF, Maier SE, Mamata H, Nabavi A, Jolesz FA, Kikinis R. (2002): Processing and visualization for diffusion tensor MRI. Medical Image Analysis 6(2):93-108.

Williams-Gray CH, Foltynie T, Lewis SJG, Barker RA. (2006): Cognitive deficits and psychosis in Parkinson's disease - A review of pathophysiology and therapeutic options. Cns Drugs 20(6):477-505.

Witzel T, Halgren E, Fischl BR, Liu AK, Ahlfors SP, Dale AM. (2001): Spatiotemporal imaging of brain activation using FreeSurfer. Neuroimage 13(6):S286-S286.

Woods SP, Troster AI. (2003): Prodromal frontal/executive dysfunction predicts incident dementia in Parkinson's disease. Journal of the International Neuropsychological Society 9(1):17-24.

Worsley KJ, Evans AC, Marrett S, Neelin P. (1992): A 3-Dimensional Statistical-Analysis for Cbf Activation Studies in Human Brain. Journal of Cerebral Blood Flow and Metabolism 12(6):900-918.

Worsley KJ, Marrett S, Neelin P, Vandal AC, Friston KJ, Evans AC. (1996): A unified statistical approach for determining significant signals in images of cerebral activation. Human Brain Mapping 4(1):58-73.

Wu HM, Huang SC, Hattori N, Glenn TC, Vespa PM, Hovda DA, Bergsneider M. (2004): Subcortical white matter metabolic chances remote from focal hemorrhagic lesions suggest diffuse injury after human traumatic brain injury. Neurosurgery 55(6):1306-1317.

Yoshikawa K, Nakata Y, Yamada K, Nakagawa M. (2004): Early pathological changes in the parkinsonian brain demonstrated by diffusion tensor MRI. Journal of Neurology Neurosurgery and Psychiatry 75(3):481-484.

Zarahn E, Aguirre GK, Desposito M. (1997): Empirical analyses of BOLD fMRI statistics .1. Spatially unsmoothed data collected under null-hypothesis conditions. Neuroimage 5(3):179-197.

Zhang LJ, Ravdin LD, Relkin N, Zimmerman RD, Jordan B, Lathan WE, Ulug AM. (2003): Increased diffusion in the brain of professional boxers: A preclinical

sign of traumatic brain injury? American Journal of Neuroradiology 24(1):52-57.